Chemodynamical simulations of disc galaxies

Awat Rahimi

Mullard Space Science Laboratory
Department of Space and Climate Physics
University College London

A thesis submitted to University College London
for the degree of Doctor of Philosophy

I, Awat Rahimi, confirm that the work presented in this thesis is my own. Where information has been derived from other sources, I confirm that this has been indicated in the thesis.

Chapter 3 was previously published as A. Rahimi, D. Kawata, C. B. Brook & B. K. Gibson, 2010, "Chemodynamical analysis of bulge stars for simulated disc galaxies", *MNRAS* **401** 1826.

Chapter 4 was previously published as A. Rahimi, D. Kawata, C. Allende Prieto, C. B. Brook, B. K. Gibson & A. Kiessling, 2011, "Metallicity gradients of disc stars for a cosmologically simulated galaxy", *MNRAS* **415** 1469.

Chapter 5 was previously published as A. Rahimi, D. Kawata, 2012, "Towards a self-consistent numerical model of late-type galaxies: Calibrating the effects of subgrid physics on galactic models", *MNRAS* **422** 2609.

Minor alterations have been made to these studies in order to maintain consistency of style.

Abstract

We use numerical simulations to probe the evolutionary history of spiral galaxies such as our own Milky Way. We use the chemodynamical simulation code GCD+ to simulate several galaxies both in a cosmological and isolated environment. The simulations include gravity, hydrodynamics, radiative gas cooling, star formation, stellar evolution, metal production and feedback into the interstellar medium. We describe in detail how these physical processes are implemented in two different versions of the code adopted in this thesis. The simulations are compared with observations in order to disentangle the details of spiral galaxy formation. Several unresolved issues regarding the evolution of spiral galaxies are specifically addressed. We first analyse the properties of stars found in the bulge component of our simulated spiral galaxies, finding that stars formed during mergers at different epochs show different elemental abundance ratio [α/Fe]. Stars formed during one of the merger events retain a systematically prograde rotation at the present time demonstrating that ancient orbital information may still be preserved in the present day kinematics of bulge stars. Next, we analysed the radial abundance gradients along the disc, comparing with recent observations from the Milky Way. We found that the disc contains a greater fraction of young stars in the outer regions, with older stars in the inner regions. This could explain the positive [α/Fe] and negative [N/O] gradients with radius. These radial trends are a natural outcome of an inside-out formation of the disc and could thus explain the recently observed positive [α/Fe] gradients seen in Milky Way disc open clusters. Finally, several isolated galaxy evolution simulations were carried out using the new and improved version of our

N-body/smoothed particle hydrodynamics code. We show that our models with higher energy feedback from supernovae and stellar winds more closely resemble the observations of spiral galaxies.

Acknowledgements

First and foremost, I would like to thank my supervisor Daisuke Kawata, for his constant support over the course of my PhD, and for always prioritising me over his many other responsibilities. It was a pleasure to be your student Daisuke. I would also like to thank the many other members of the MSSL Astrophysics group who guided me over the years (too numerous to list) but I would like to mention my co-supervisor Mark Cropper and especially Curtis Saxton, who gave up much of his time to support me throughout my studies. I also would like to thank Kinwah Wu and Ignacio Ferreras for providing me with great intellectual stimulation through their fascinating talks and seminars.

I would like to thank all of my friends at MSSL and elsewhere for their encouragement and friendship. Again, this page is too small to contain all of their names, but you know who you are.

I would like to thank my Mum and Dad for their encouragement throughout all of my student career. I couldn't be where I am today if it weren't for their upbringing. I would like to thank Parviz for being a great brother to me. Thanks also to all of my large extended family for their support.

I would like to thank my examiners Frazer Pearce and Graziella Branduardi-Raymont for their useful comments and suggestions, which helped to improve this thesis. Finally, I would like to acknowledge the funding I received for the three and a half years of my PhD from the Science and Technology Facilities Council (STFC).

Contents

List of Figures

List of Tables

Chapter 1

Introduction

1.1 Background

Galaxies are the fundamental components of our Universe. Their individual stars are the primary source of their luminous material. It is now known that stars routinely host planets[1]. The space in between the stars: the interstellar medium (ISM), is made up of gas and dust. Stars in a galaxy may be found grouped together in associations ranging from small open clusters with up to a few thousand stars to large globular clusters with hundreds of thousands of stars or more. In addition, the major component of galaxies is a material termed dark matter since it does not emit, absorb or reflect electromagnetic radiation, and so cannot be observed directly. Its presence is indirectly inferred due to its gravitational effect on luminous matter. Galaxies range in size from dwarfs with a few million stars to giant ellipticals with many trillions of stars. Galaxies are often found together in small groups or in larger associations known as clusters. Groups of clusters are known as superclusters. On the largest scales, these superclusters are arranged along filaments separated by huge voids. Galaxies are, therefore, the main structural components of our Universe. By

[1] As of the time of publication of this thesis, there have been hundreds of confirmed detections of extra-solar planets with thousands of other candidates (Batalha et al., 2012). Some estimate that there could be many billions of planets in our home galaxy, the Milky Way, making them as ubiquitous as the stars (e.g. Cassan et al., 2012).

understanding the process of galaxy formation and evolution in detail, we go a long way towards understanding how the wider Universe works. However, galaxy formation and evolution remains one of the most outstanding problems in modern astrophysics.

In 1990, the National Aeronautics and Space Administration (NASA) sent the 2.4 m diameter Hubble Space Telescope (HST) into low Earth orbit. Initially it was found that the main mirror had been ground incorrectly, leading to blurred images. However, a servicing mission in 1993 restored it to its intended quality. Due to its location beyond the Earth's atmosphere, it is able to 'see' with remarkable clarity revolutionising Astronomy with its vivid images. For example, the HST has revealed in spectacular detail the vast array of shapes and sizes in which galaxies are found (Fig. 1.1). The HST has also taken the deepest image ever of our Universe (Fig. 1.2), showing galaxies in the early stages of their evolution. In recent times, rapid advances in technology have meant that ground-based telescopes have become bigger and more powerful, with the larger collecting area of the new mirrors capturing more photons from astronomical sources. The larger mirrors also mean that the newer telescopes can look at fainter and more distant objects. Since light travels at a finite speed, when looking at more distant galaxies, we are also looking further back in time. We thus build up a picture of galaxies at different stages of their evolution. This array of observational snapshots of galaxies of different age provides us with some clues as to their evolution. However it is not clear how galaxies evolve from one stage (snapshot) to another. Since galactic history has occurred only once,[2] and since we cannot perform any 'real' experiments, to address this fundamental issue, computer simulations modelling galaxy formation and evolution have been developed.

Simulations can capture important features of a physical process and suggest avenues for further research. With increasing computing power, the models and

[2]This is equivalent to saying we cannot travel back in time, or the arrow of time only flows forwards.

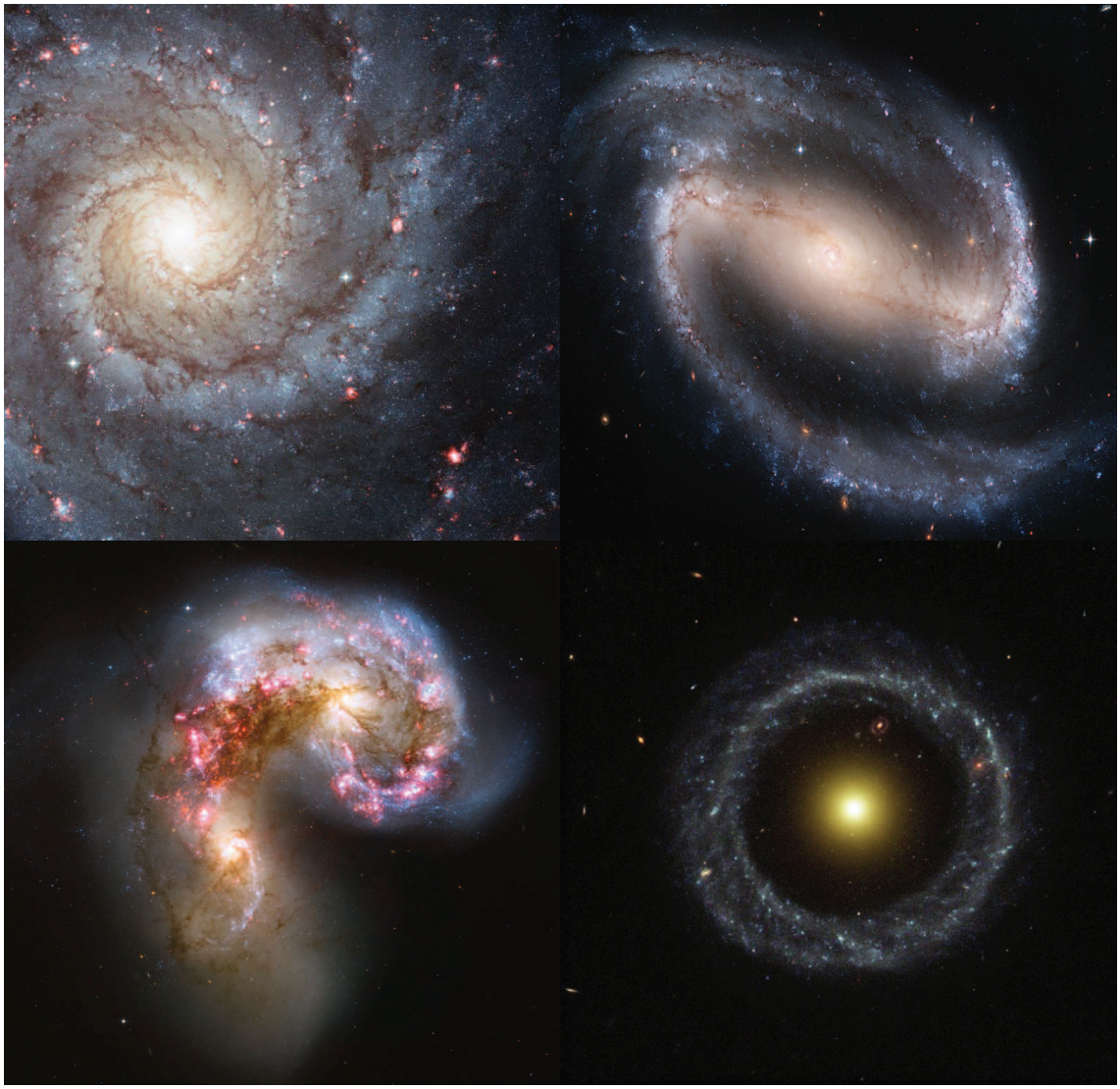

Figure 1.1: Mosaic of four Hubble Space Telescope images of galaxies. From top-left going clockwise: Spiral galaxy M74 (NGC 628), prototypal barred spiral galaxy NGC 1300, Hoag's object ring galaxy (PRC D-51) and the Antennae galaxies (NGC 4038/NGC 4039), an example of two colliding galaxies. Credit: NASA, ESA, and the Hubble Heritage Team (STScI/AURA)-ESA/Hubble Collaboration.

simulations have become increasingly sophisticated, incorporating more and more of the important physical processes involved in galaxy formation and evolution. One of the reasons behind the improvement of these models is the availability of new and more detailed observational data, especially for our own galaxy, the Milky Way. In the very near future, space telescopes such as *Gaia* (expected launch date: August 2013) together with ground-based surveys such as RAVE, SEGUE, LAMOST, Gaia-ESO, APOGEE and HERMES will provide unprecedented levels of observational data, both kinematical and chemical, on stars in our Galaxy.

In this thesis, a state-of-the-art galaxy simulation code, galactic chemodynamics plus (`GCD+`), is used to simulate disc galaxies such as our Milky Way and M33. A new and improved version of the code is developed. The simulations are then compared against observational data in various studies to shed new light on the formation and evolution of disc galaxies.

As the building blocks of our Universe, galaxies represent the link between the large-scale cosmological structures and the local small-scale structures around us: the planets, Sun and stars. All theories of galaxy formation and evolution must therefore account for the cosmological context in which galaxies form. In the next section an overview is given for such a cosmological context of structure formation. Then in Section 1.3 a brief description is given on the current state of knowledge about our own Galaxy, the Milky Way. A very brief historical review of theories for spiral galaxy formation is given in Section 1.4. In Section 1.5 different galaxy formation modelling techniques are presented with an emphasis on N-body chemodynamical codes. The final section of this chapter is used to summarise the studies investigated in this thesis. In Chapter 2, the chemodynamical galaxy evolution code `GCD+` and its updated version are described in detail. The results presented in Chapters 3, 4 and 5 were each published in the Monthly Notices of the Royal Astronomical Society, and each represents a separate study of galaxy formation and evolution. In Chapter 6 the conclusions from this thesis are outlined, as well as some future work to be carried out in this field.

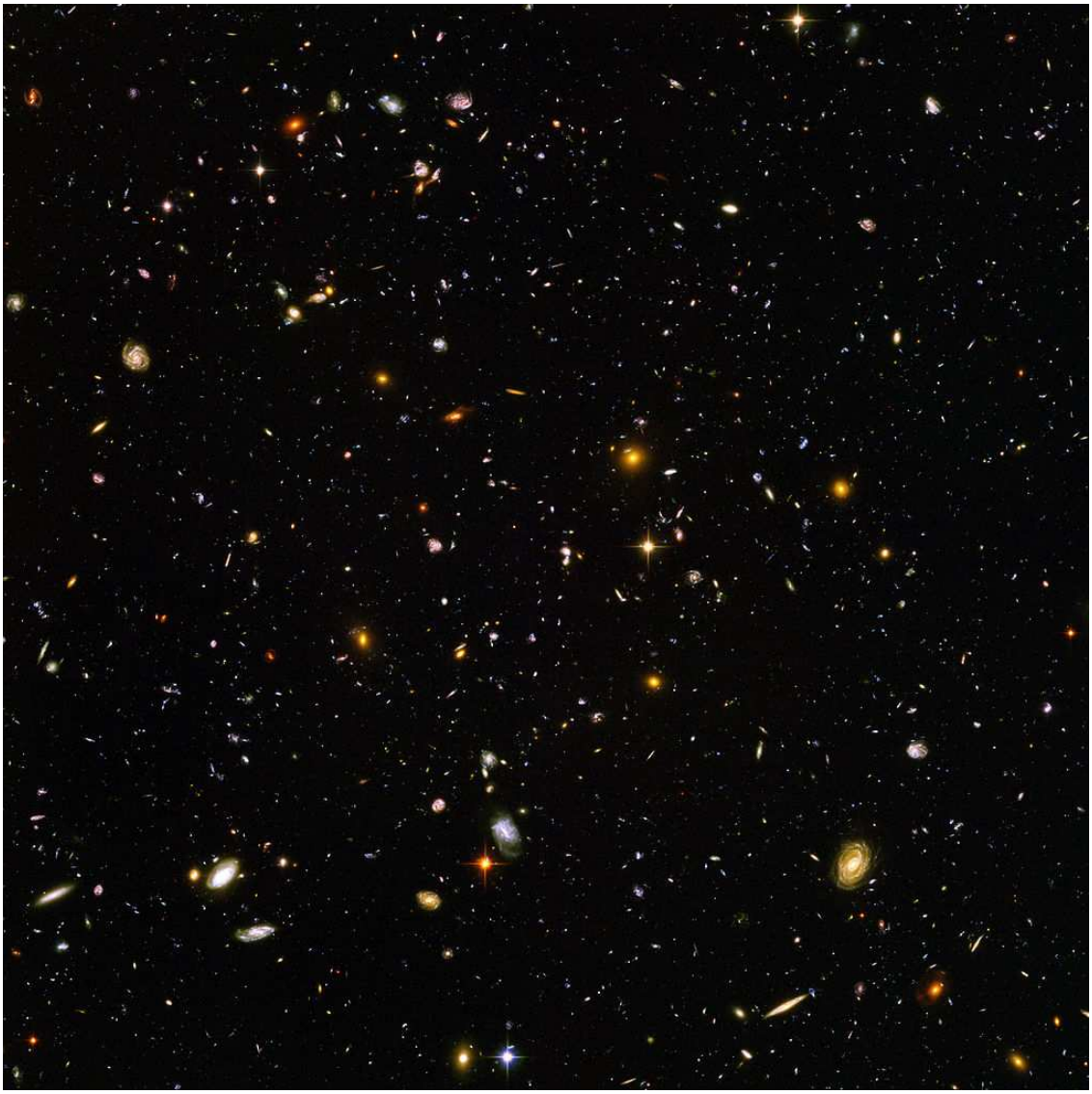

Figure 1.2: Hubble Ultra Deep Field (HUDF), the deepest image of the Universe ever taken in visible light, looking back approximately 13 billion years (around 800 million years after the Big Bang). The image shows some of the oldest galaxies ever seen in the Universe. To take this image, the telescope accumulated data from September 24, 2003, through to January 16, 2004. Credit: NASA, ESA, S. Beckwith (STScI) and the HUDF Team.

1.2 Cosmological Context

In the 1920's, Edwin Hubble, using the 2.5 m Hooker telescope at Mt. Wilson in California, measured the distances to spiral nebulae using Cepheid variable stars as standard candles, showing that they were extragalactic systems lying far from our Milky Way. By 1929 Hubble had measured the velocity of these neighbouring galaxies. He found that the more distant the galaxy, the faster it was moving away from us. This suggested that the space in between the galaxies was getting larger and larger. By extrapolating back in cosmic time, this implied that the Universe had emerged from an extraordinarily dense and hot state, known as the 'Big Bang'[3]. The discovery of the predicted cosmic microwave background (CMB) radiation in 1965 by A. A. Penzias and R. W. Wilson[4] confirmed for the majority of the astronomical community the Big Bang theory[5]. In 1989, NASA launched the Cosmic Background Explorer (COBE) satellite to investigate the CMB radiation. COBE showed that the CMB was a near perfect black-body spectrum but that it contains very small anisotropies. Recently, the Wilkinson Microwave Anisotropy Probe (WMAP, Spergel et al., 2003) has measured in unprecedented detail the temperature fluctuations in the CMB corresponding to the last scattering surface when matter and radiation dissociated. Currently, the European Space Agency's (ESA's) Planck spacecraft is complementing and improving upon observations made by WMAP, measuring the anisotropies at smaller angular scales and higher sensitivities.

During the 1970's, Vera Rubin, Ken Freeman and several other groups of astronomers began measuring the rotation curves of galaxies. It was expected that stars further from the centre of the Galaxy would rotate slower. Different groups found that the orbital speed of the stars and gas remained remarkably constant with increasing radius from the centre of the galaxy. This implied that there must be a significant mass of unseen material in the Galaxy, which via gravity was affecting

[3]The term Big Bang was actually first coined by Sir Fred Hoyle as a derision.

[4]Penzias and Wilson won the Nobel Prize for physics for their discovery of the CMB.

[5]Until that time cosmologists were divided primarily between the Big Bang theory and an alternate theory known as Steady State.

the orbit of the stars and luminous matter. Using numerical simulations containing up to 500 mass points, Ostriker & Peebles (1973) followed the evolution of galaxies with starting characteristics similar to the disc of our own Milky Way and found that they were rapidly and grossly unstable to bar-like modes. In order to maintain stability, an extensive dark matter halo was required to match the observed rotation curves. Since then, dark matter has been invoked to explain a number of wide ranging observational phenomena, from the motion of stars within galaxies (e.g. Freeman, 1970), to the distribution and temperature of hot X-ray gas in clusters (e.g. Mulchaey et al., 1993) to the gravitational lensing of very distant galaxies by foreground clusters (e.g. Tyson et al., 1990). Little is known about the nature of the dark matter. Some cosmologists and particle physicists suggest that it is some kind of weakly interacting massive particle[6].

The accuracy of the current CMB data as well as data from Type Ia supernovae (SNe Ia, Astier et al., 2006) and baryon acoustic oscillations (BAO, Eisenstein et al., 2007) has resulted in a concordance model of cosmology. According to this model, we live in a flat Universe, with total energy density close to the critical density. Nearly 1/3 of the density is accredited to matter with dark matter dominating ($\Omega_{DM} = 0.228 \pm 0.027$, Komatsu et al., 2011) and baryons contributing less than 5% ($\Omega_B = 0.0455 \pm 0.0028$). The remainder of the energy density is attributed to a smoothly distributed vacuum energy ($\Omega_\Lambda = 0.727 \pm 0.030$) with very little known about its nature except that it acts to accelerate the expansion of the Universe. Since so little is known about this mysterious but major component of the Universe, it is termed 'dark energy'. The existence of dark energy was proposed to explain the observed accelerated expansion of the Universe apparent from observations of distant SNe Ia (Perlmutter et al., 1998; Schmidt et al., 1998). The current best measurement for the expansion rate of the Universe, also known as the Hubble constant H_0, is $H_0 = 70.4 \pm 1.4 \mathrm{kms}^{-1}\mathrm{Mpc}^{-1}$ constructed from WMAP seven-year

[6]As of the time of publication of this thesis, there has yet to be a direct detection of a dark matter particle.

data with gaussian priors based on earlier estimates from other studies such as observations of SNe Ia and BAO (e.g. Jarosik et al., 2011; Komatsu et al., 2011).

The current most successful model of cosmology is known as Lambda-Cold Dark Matter (ΛCDM), so called because the dark matter is assumed to be 'cold', or non relativistic, where the Λ denotes dark energy. ΛCDM is thus far the most successful model for explaining a number of observations, including the existence and structure of the CMB, the large-scale structure of galaxies and clusters, the distribution and abundance of the light elements and the accelerating expansion of the Universe. In the CDM scenario structures form hierarchically in a bottom up fashion starting with the amplification via gravitational instability of primordial small-scale density fluctuations in the dark matter distribution. Due to the scale-free nature of gravity and the dissipationless nature of CDM, one expects the formation at all scales of collapsed self-similar ellipsoidal objects (Mayer et al., 2008): the dark matter haloes. The largest haloes are expected to form last. Surrounding the most massive haloes are a swarm of smaller dark matter haloes, the so called sub-structures or sub-haloes. These sub-haloes may themselves be surrounded by smaller structures (sub-sub-haloes) and so on. ΛCDM simulations predict that there should be many hundreds of such sub-structures around a galaxy the size of our Milky Way (e.g. Klypin et al., 1999; Moore et al., 1999a; Springel et al., 2005b, 2008). However observations have thus far only found a handful of such satellite galaxies (e.g. Belokurov et al., 2007). Furthermore, the inner density profiles of virialized CDM haloes is too steep with respect to what is inferred from rotation curves of galaxies: the so called 'core-cusp' problem (e.g. Dubinski & Carlberg, 1991; Navarro et al., 1997; Moore et al., 1999b; Klypin et al., 2001; Diemand et al., 2005; de Blok, 2010). Recent work has also suggested that dark matter may be 'warm', and indeed warm dark matter may solve some outstanding issues with CDM such as the missing satellites problem and the observed kinematics of the Milky Way satellites (e.g. Lovell et al., 2012). Despite its mentioned discrepancies, the ΛCDM model is consistent with a wide and admirable range of observations including the cosmological power spectrum. Therefore the

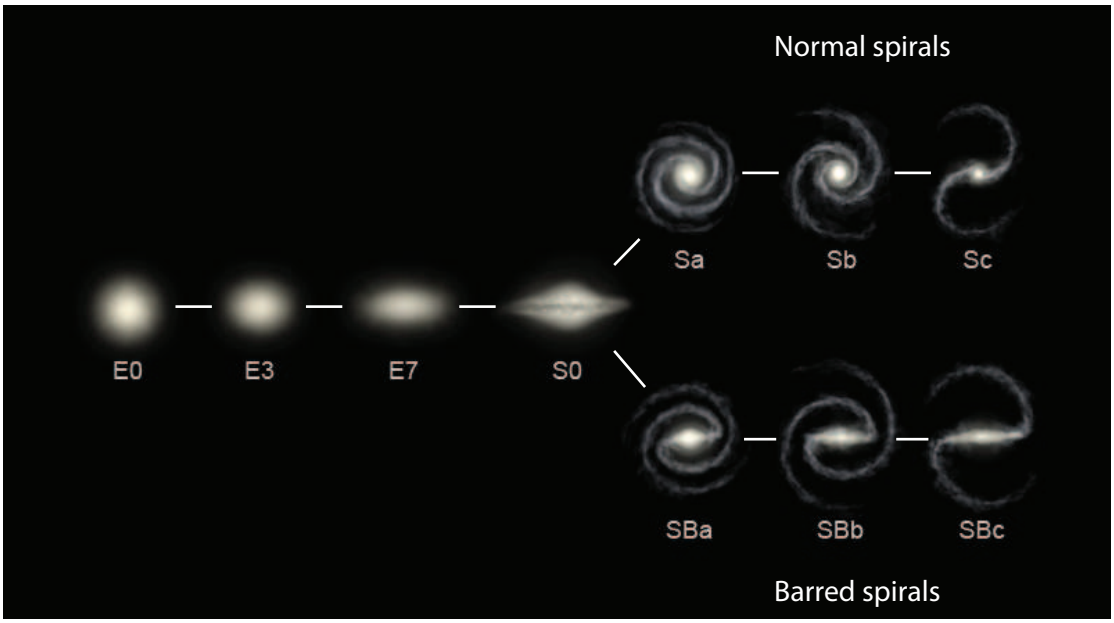

Figure 1.3: Illustration of The Hubble Sequence, also known as the tuning fork diagram. On the left hand side are elliptical galaxies ranging from E0 to E7 based on their ellipticity. Lower E values are more spherical. The two branches on the right hand side represent the spiral galaxies, with lower-case a, b and c representing how tightly-wound the spiral arms are and how prominent the bulge is. Capital B represents a barred spiral galaxy. An SBc galaxy therefore, is one with a bar and a small bulge and prominent spiral arms, where new star formation is occurring. At the node are the S0s, which have intermediate morphology between the spirals and ellipticals. Credit: Ville Koistinen.

simulations presented in this thesis were all carried out using a ΛCDM cosmology.

1.3 The Milky Way

Perhaps the most distinctive feature of a dark night sky is the bright band of light which stretches from one side of the night sky to the other. The ancient Greek philosopher Democritus (460 − 370 BC) first speculated that this bright streak may consist of distant stars. The Persian astronomer Abu Rayhan al-Biruni (973−1048) proposed the Milky Way galaxy to be a vast ensemble of stars. It was only in 1610 when Galileo first pointed his telescope towards the Milky Way that it was proven to consist of a vast amount of stars. Thomas Wright hypothesised in 1750 that the Milky Way consisted of a rotating body of stars held together by gravitational forces

similar to the solar system but on a larger scale. The resulting disc would appear as a band due to our position within it. In the early 1920's, astronomers were debating the size of the Milky Way and whether spiral nebulae were extragalactic 'island universes' or located within the Galaxy. The issue was settled by 1925 when Edwin Hubble found Cepheid variable stars in the Andromeda and Triangulum nebulae, using them as standard candles to set distance scales which showed both spiral nebulae to be a great distance from the Milky Way and therefore a separate galaxy in their own right (Hubble, 1925).

In 1930, Robert Trumpler quantified the effect of the absorption of light by interstellar dust in the Galactic plane, resulting in greatly improved estimates for the size of our Milky Way. By the mid 1930s, astronomers came to realise that the Milky Way was just one of countless other galaxies of varying shapes and sizes. Having observed thousands of such galaxies, Hubble noticed a trend and ordered them into a sequence based on their visual morphology, known as the Hubble Sequence (Fig. 1.3).

Since then there has been a great deal of progress in our understanding of the Galaxy. Walter Baade showed that galaxies consist of two stellar populations, Population I exemplified by the blue giants seen near the solar neighbourhood, and Population II typified by red giants seen in globular clusters. Baade assumed that Population I were young and that Population II were old. In the following years, further progress was made due to spectroscopic observations and the emerging theory of stellar evolution, which led to the current picture of Population I containing young, metal-rich[7] stars that are on nearly circular orbits, and Population II containing old, metal-poor stars that are generally on highly inclined and/or eccentric orbits. By 1958, Baade's original simple division had grown into an idea that connected stellar evolution and the progressive enrichment of the ISM, to the pattern of star formation in the Galaxy and the Galaxy's dynamical evolution. Much of modern astrophysics is interested in exploring this link to deduce the history of galaxies.

In recent times, we have learned much more about the Milky Way's structure and

[7]Astronomers designate all elements heavier than helium in the periodic table as *metals*.

attributes. The Milky Way has a total mass of approximately 1 trillion solar masses (McMillan, 2011) and contains approximately 300 billion stars, with a diameter of 110,000 light years[8]. The Milky Way is classified as Hubble type Sb or Sc (Sbc). The presence of a central bar was first suggested by de Vaucouleurs (1964) from observations of non-circular motions in the gas kinematics. Recent studies (e.g. Blitz & Spergel, 1991; Binney et al., 1991; Babusiaux & Gilmore, 2005) have shown evidence to support this, hence making it a SBbc. Most astronomers now believe that the Milky Way is the second largest galaxy (after Andromeda) in the Local Group of galaxies, which resides on the outskirts of the great Virgo Supercluster. The great Virgo Supercluster is itself just one of many thousands of 'Local' Superclusters, a huge collection of which make up the observable Universe (see Figs 1.5−1.9). It is widely accepted that our Galaxy has several distinct structural components, each with varying ages, kinematic, dynamic and chemical properties. These components are the bulge, thin disc, thick disc and the halo.

1.3.1 The Bulge

The bulge dominates the Galaxy interior to around 3 kpc. Our view of the Galactic bulge is heavily obscured at optical wavelengths. Much of the work on bulge stars has been carried out along lines of sight which have significantly less obscuration. The most common such line of sight is known as Baade's window which intersects the bulge approximately 300 pc below the plane, so the region where the bulge and disc intersect is still poorly examined. Furthermore, contamination of bulge samples with foreground disc stars is a problem. Nevertheless we know that the bulge contains a bar from both photometry (e.g. Blitz & Spergel, 1991; Stanek, 1995; Binney et al., 1997; Babusiaux & Gilmore, 2005; Gonzalez et al., 2011) and kinematics (e.g. Binney et al., 1991; Fux, 1999; Bissantz et al., 2003; Shen et al., 2010). The bulge is chemically complex with a wide range of metallicities[9], ranging

[8] 110,000 lyrs $\simeq$ 33.7 kpc, where 1 pc=3.1×10^{13} km

[9] $[\mathrm{Fe/H}] \equiv \log(\mathrm{Fe/H}) - \log(\mathrm{Fe}_{\odot}/\mathrm{H}_{\odot})$

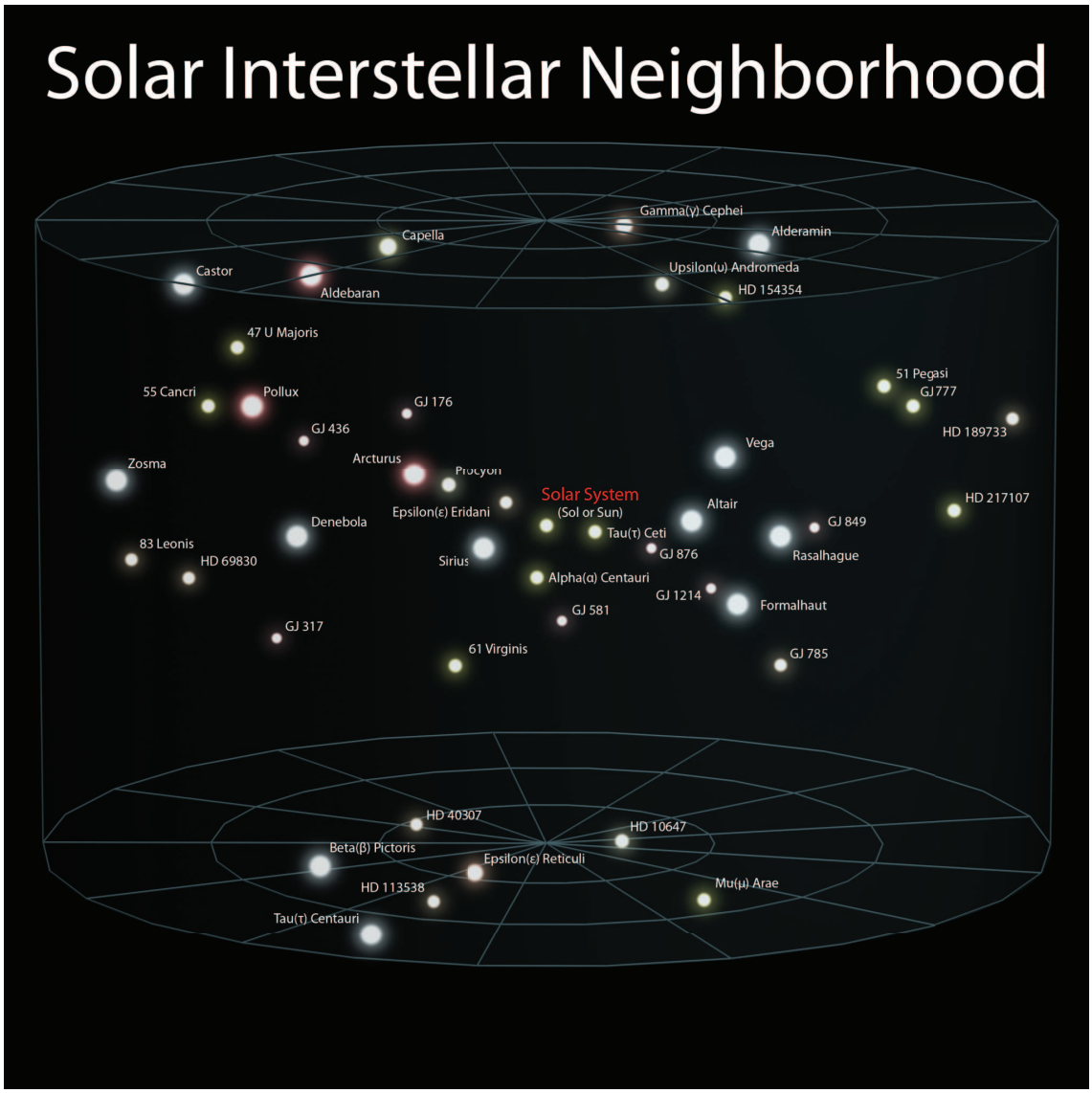

Figure 1.4: Illustration of the solar interstellar neighbourhood. Credit: Andrew Z. Colvin.

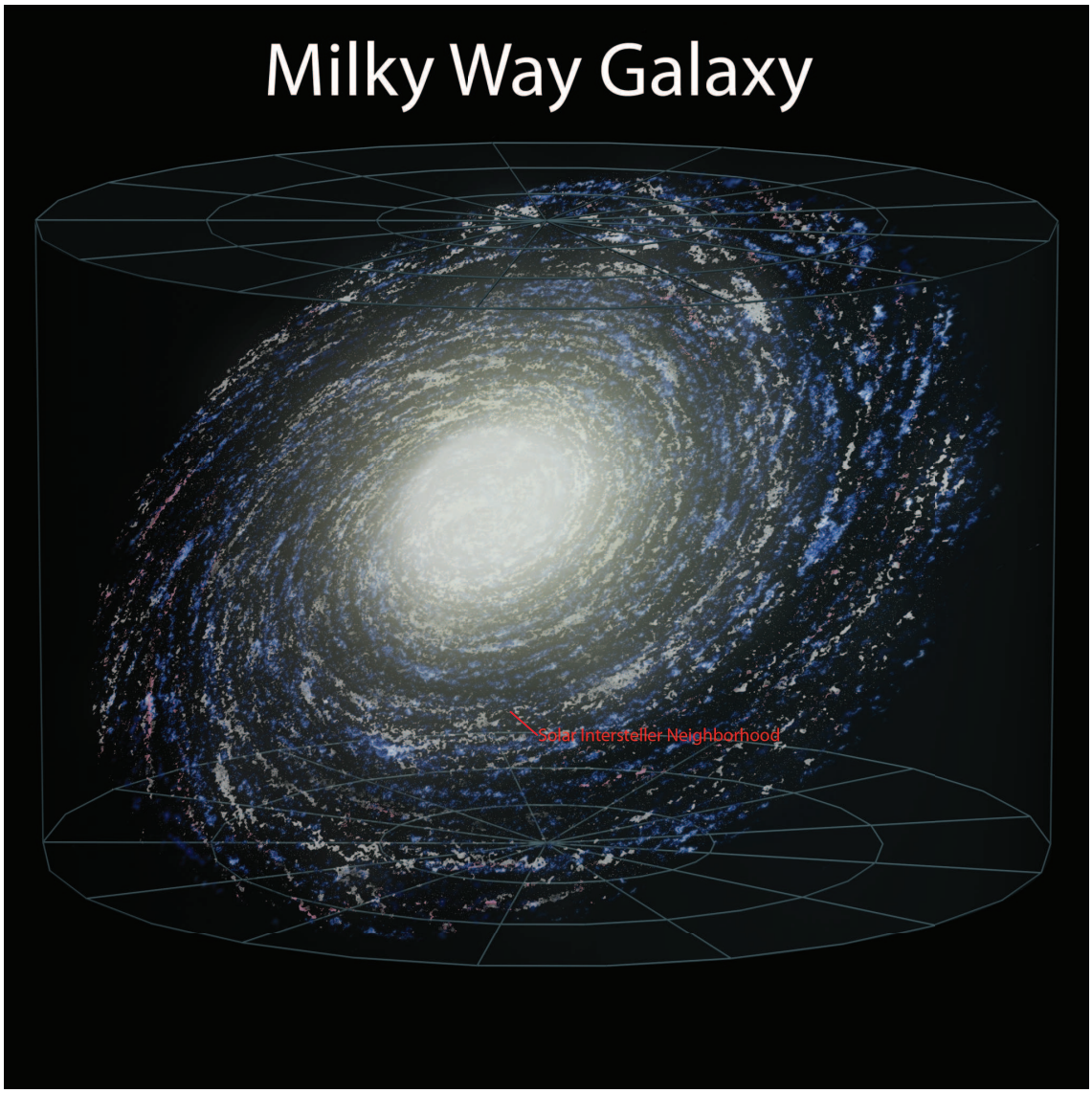

Figure 1.5: The solar interstellar neighbourhood in the Milky Way. Credit: Andrew Z. Colvin.

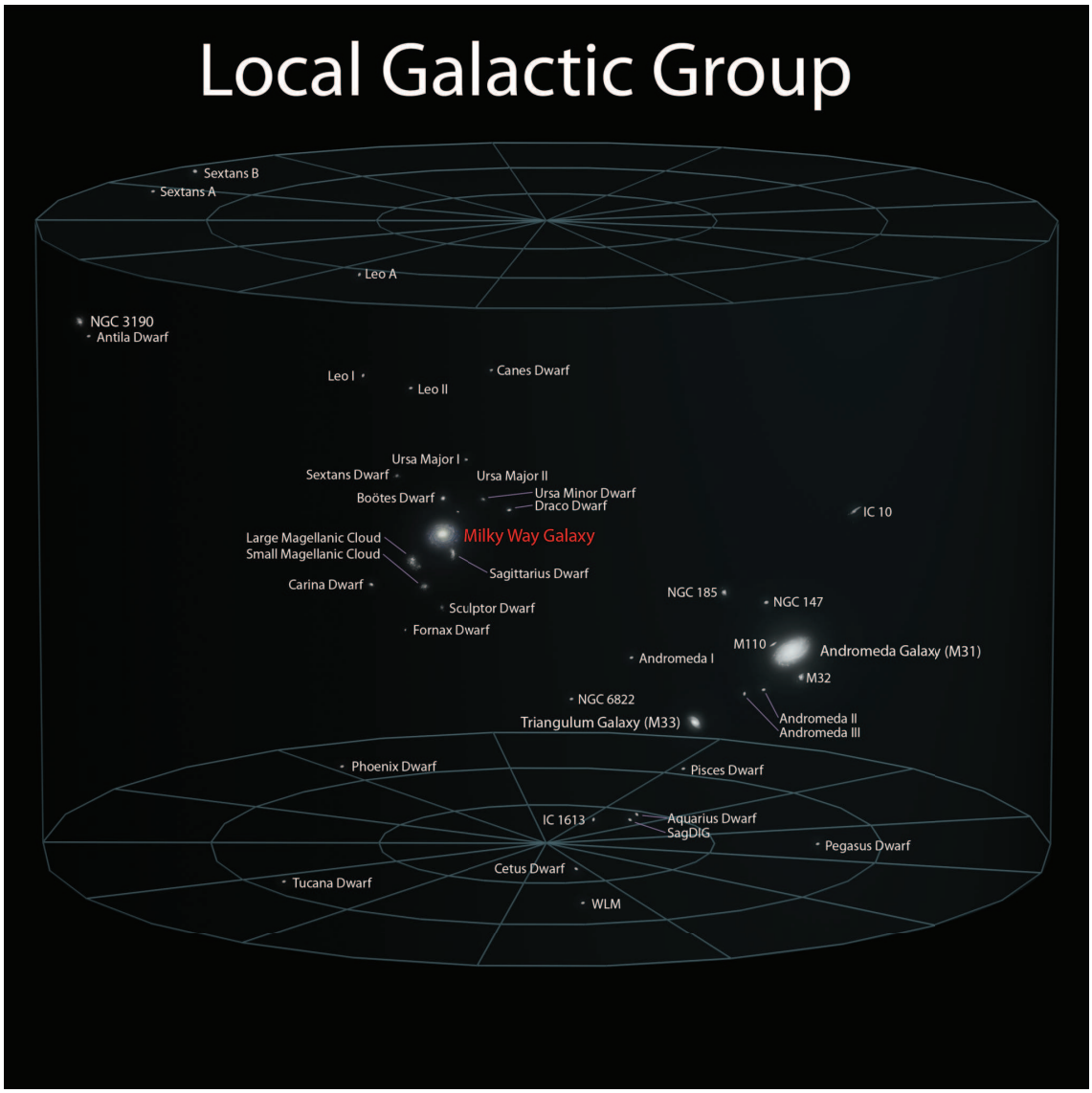

Figure 1.6: The Milky Way in the Local Group of galaxies. Credit: Andrew Z. Colvin.

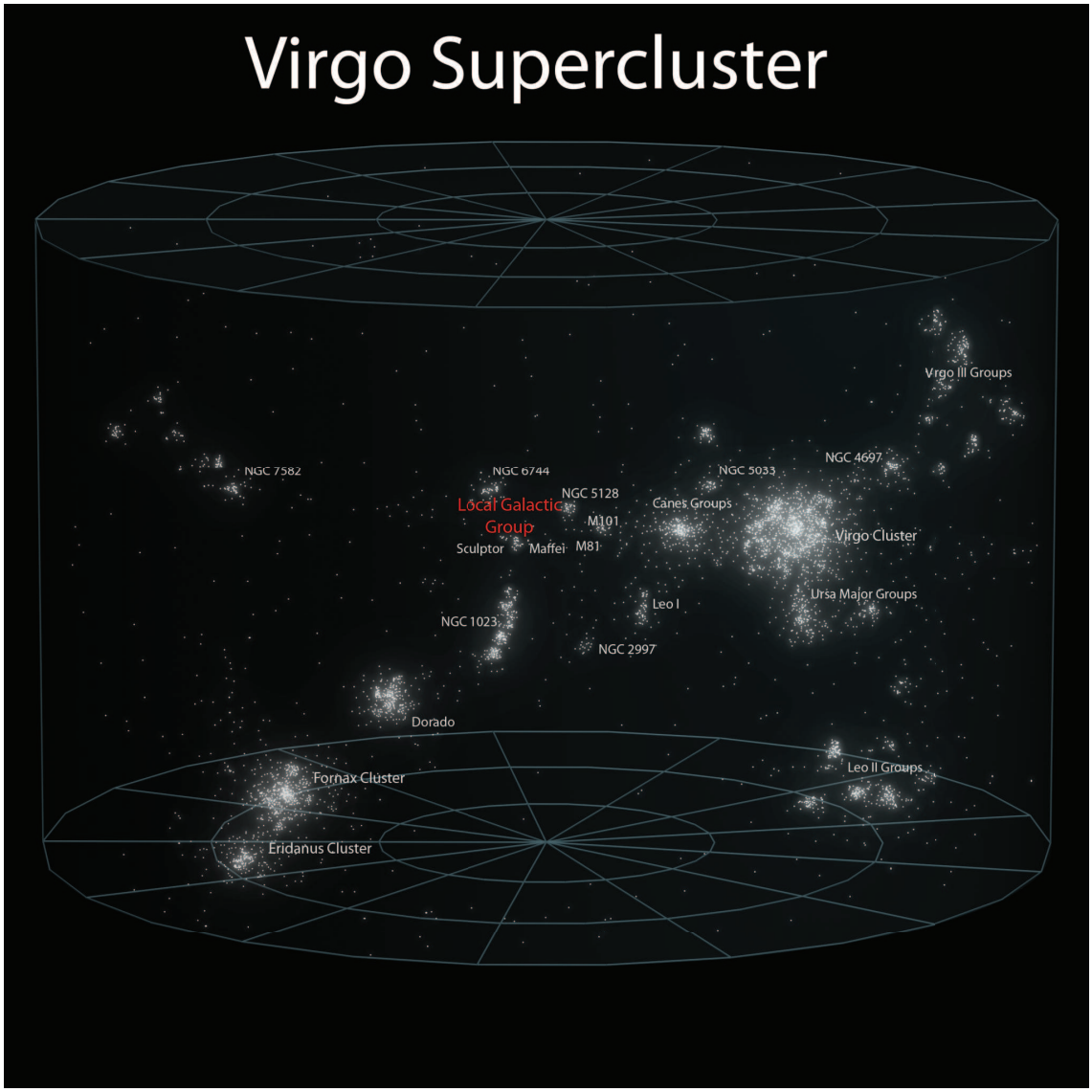

Figure 1.7: The Local Group within the Virgo Supercluster. Credit: Andrew Z. Colvin.

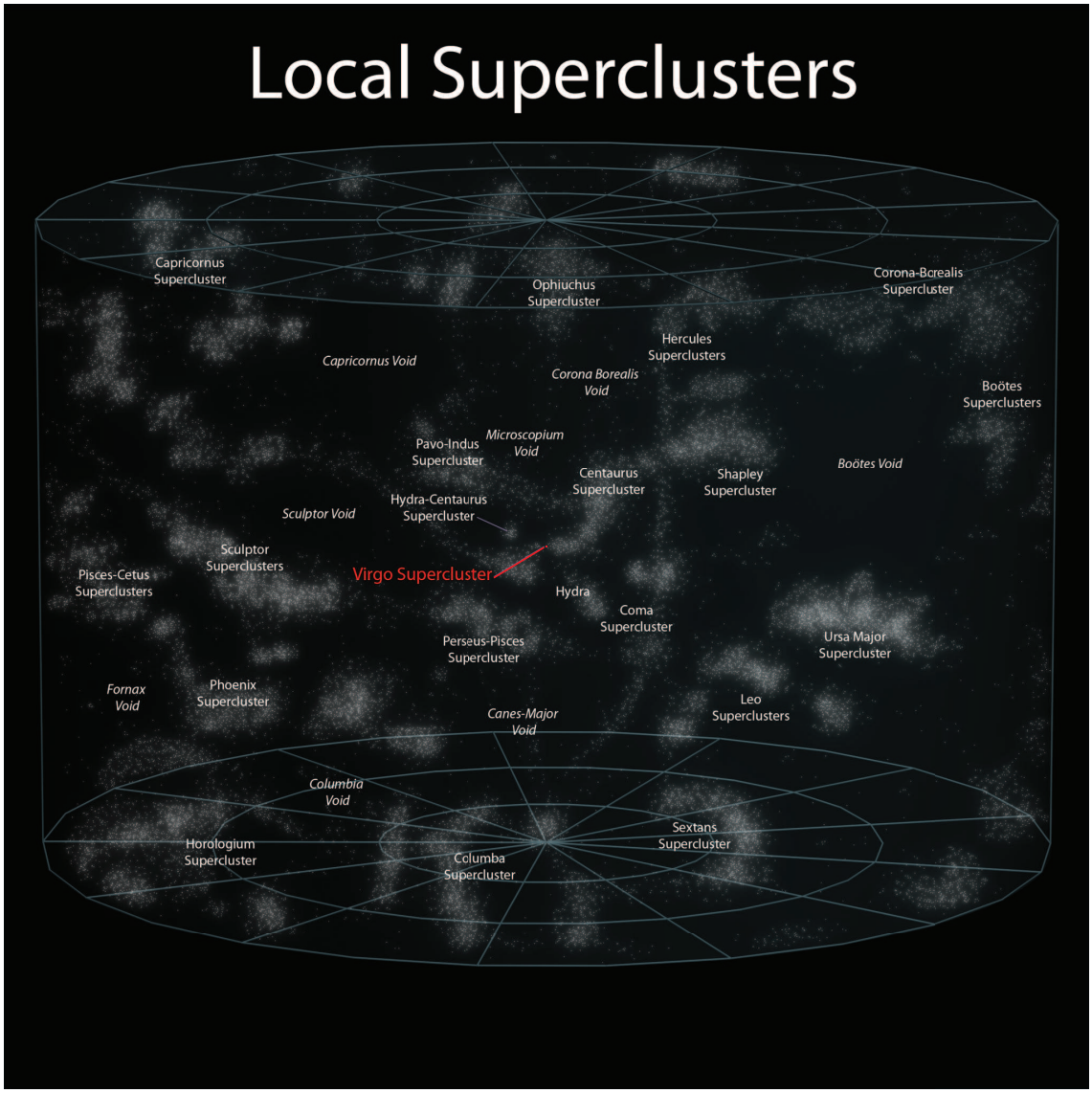

Figure 1.8: The Virgo Supercluster (small red dot) as a small speck within the Local Superclusters. Credit: Andrew Z. Colvin.

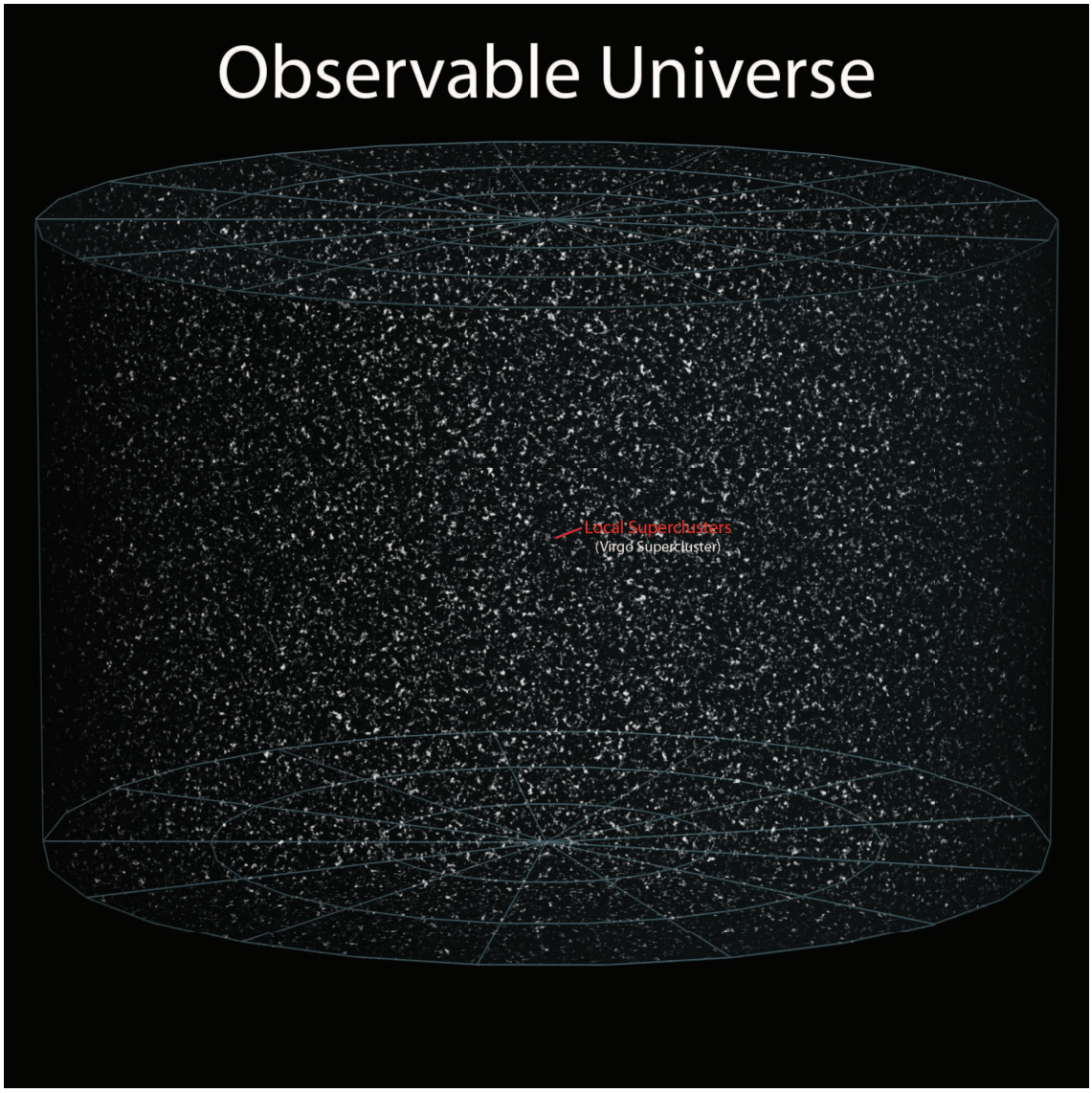

Figure 1.9: The local Superclusters within the Observable Universe. Credit: Andrew Z. Colvin.

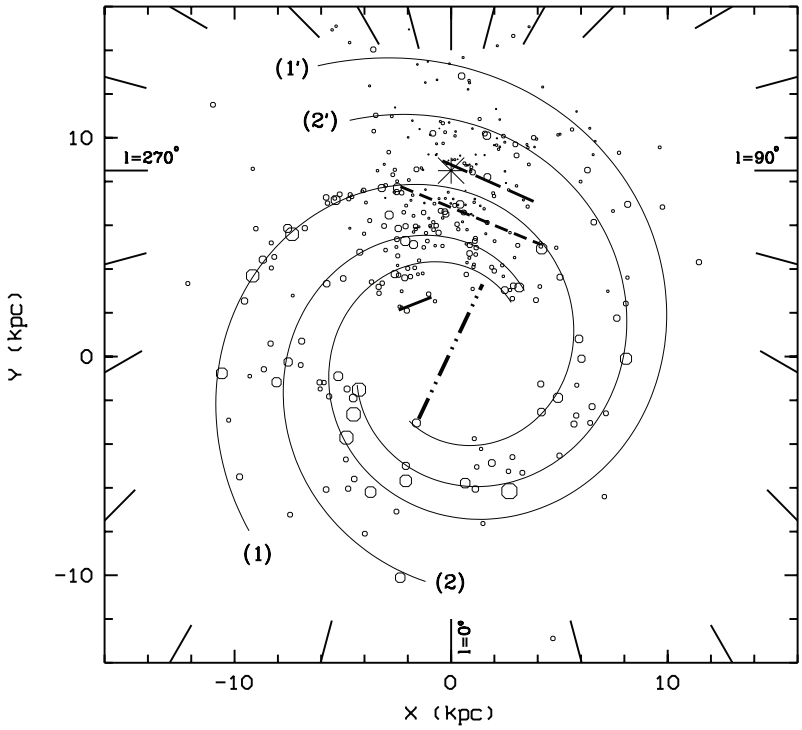

Figure 1.10: The location of young star forming complexes (circles) in our Galaxy in relation to the spiral arms. The large asterix marks the position of the Sun. The four arms are plotted. 1: Sagittarius-Carina arm, 2: Scutum-Crux arm, 1': Norma-Cygnus (or external) arm and 2': Perseus arm. The local arm feature (long dashed line) is shown, as is the bar orientation and length (dashed-dot-dot line) and the expected departure from a logarithmic spiral arm observed for the Sagittarius-Carina arm (short dashed line). The majority of the star forming complexes lie on or near spiral arms. From Russeil (2003).

from metal poor stars with [Fe/H]=−1 to metal rich stars with [Fe/H]=0.5, with a peak at [Fe/H]~ -0.2 (e.g. Fulbright et al., 2006; Zoccali et al., 2008). Stars in the bulge are generally assumed to be old, however the presence of massive stars also indicates continuing star formation.

1.3.2 The Thin Disc

When we look up at the sky on a dark night, the faint band of light stretching across the sky is primarily the Milky Way's thin disc. The thin disc defines the Galactic plane and is host to a significant proportion of the Galaxy's supply of gas as well as the Galaxy's population of open clusters. The Sun lies in the thin disc, ~ 8.3 kpc from the centre (Gillessen et al., 2009; McMillan, 2011) and within ~ 15 pc

of the plane. The thin disc is also the dominant stellar component of the Milky Way, containing the majority of the overall baryonic material in the Galaxy. The thin disc is the main site of ongoing star formation in the Galaxy, especially in the spiral arms (Fig. 1.10). The rotational velocity of stars along the disc remains fairly constant with radius from the centre, with the disc rotating at around 220 kms^{-1}. This rotational velocity is still in debate with some recent authors suggesting a value of around 210 kms^{-1} (e.g. Sofue et al., 2011) and others finding values closer to 250 kms^{-1} (e.g. Reid et al., 2009; McMillan, 2011). The density along the disc is approximated by an exponential with scale length between 3-4 kpc and scale height of 300 pc (e.g. Jurić et al., 2008). Thin disc stars are relatively young but span a wide range of ages with the youngest stars currently in the process of formation and the oldest stars more than 10 Gyr old. This mixture suggests a star formation rate (SFR) that has remained fairly constant or has slightly decreased with time over the age of the Galaxy (e.g. Rocha-Pinto et al., 2000). Disc stars are metal rich, with a narrow distribution peaking around solar metallicity (middle panel of Fig. 1.11).

1.3.3 The Thick Disc

Gilmore & Reid (1983) showed that near the Sun, the stellar vertical density profile is tightly matched by the sum of two exponentials in $|z|$ with scaleheights of 300 and 900 pc (Jurić et al., 2008). This observation led to the notion of a disc which was made up of two distinct (but overlapping) components, the thin and thick discs. The vertical scaleheight of the thick disc (900 pc) is significantly larger than the thin disc, but its precise value is uncertain, making it difficult to determine the fraction of local stars which belong to each component. Current estimates put the value around 10:1 in favour of the thin disc (Jurić et al., 2008).

The authenticity of the distinction between the thin and thick discs is still debated (e.g. Bovy et al., 2012), and an important aspect of recent research has been to find a method of separating the two components in a physically well motivated

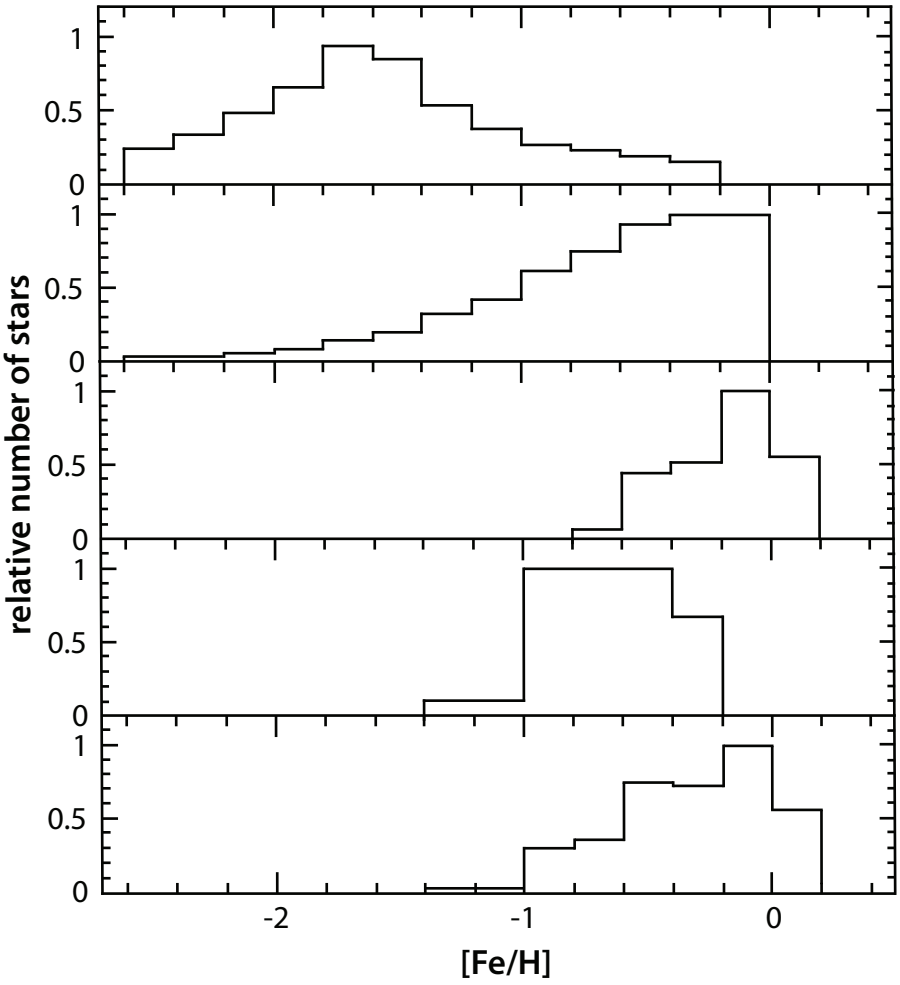

Figure 1.11: The metallicity distributions from the different Milky Way components. The panels represent, from top to bottom; the local stellar halo (Carney et al., 1994); the outer Galactic bulge (Ibata & Gilmore, 1995), truncated at solar metallicity due to calibration limitations; the volume-complete local thin disc F/G stars (from the Gliese catalogue); the volume complete local thick disc stars; and lastly the 'solar cylinder', i.e. F/G stars integrated vertically from the disc plane to infinity. From Wyse (1999).

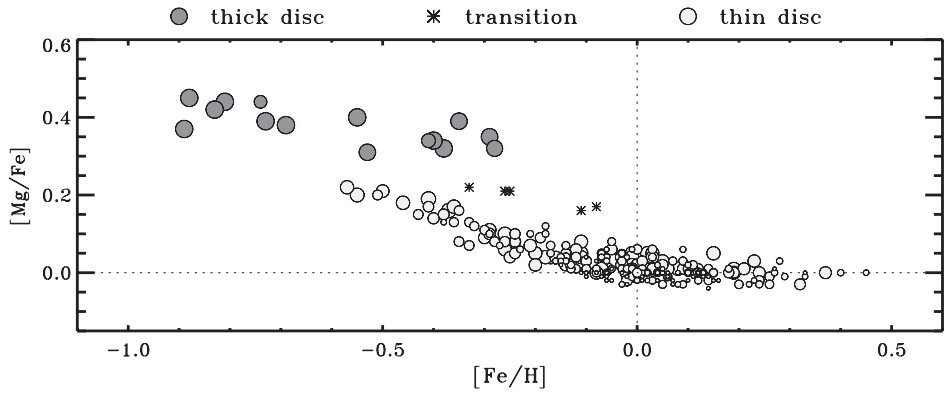

Figure 1.12: The local, volume-complete abundances of iron and the α-element magnesium for 271 F-, G- and K-type stars within 25 pc. Circle diameters are in proportion to the stellar age estimates, i.e. small diameters correspond to young stars. Light and dark circles represent members of the thin and thick discs, respectively. This figure suggests a gap in star formation in between the youngest thick disc and oldest thin disc stars. From Fuhrmann (2008).

way. A kinematical separation like that used by Bensby et al. (2005) has had some success as it is argued that thick disc stars can be identified by their lower rotational velocity, since near the Sun, the thick disc lags solar rotation. Perhaps a clearer distinguishing criterion is chemistry. Thick disc stars generally have, at any given metallicity [Fe/H], a higher abundance of alpha−elements to iron ratio [α/Fe] (Fig. 1.12). An α-particle is identical to a helium nucleus, consisting of two protons and two neutrons. Elements heavier than ^{12}C synthesised by the capture of α-particles are known as $\alpha-$elements. These include O, Ne, Mg, Si, S, Ar, Ca and Ti. The $\alpha-$elements are produced primarily in Type II supernovae (SNe II) whose progenitors are massive stars with shorter lifetimes. Iron on the other hand, primarily comes from SNe Ia which derives from a binary system of less massive, much longer lived stars (e.g. Kobayashi et al., 2000). This high [α/Fe] value implies that the thick disc formed rapidly within the first $\sim$ 2 Gyr of the Galaxy's life. All thick disc stars are thought to be older than $\sim$ 9 Gyr. There are several theories for the origin of the thick disc including disc heating (Kroupa, 2002), satellite accretion (Abadi et al., 2003b; Yoachim & Dalcanton, 2005), gas rich mergers (Brook et al., 2004b) and radial migration (Roŝkar et al., 2008; Schönrich & Binney, 2009a). In all formation scenarios, the thick disc is older than the thin disc. Thick discs have been

observed in many other disc galaxies (e.g. Dalcanton & Bernstein, 2002; Yoachim & Dalcanton, 2006) suggesting that they may be ubiquitous.

1.3.4 The Halo

The halo contains ∼1% of the Galaxy's stars. It is made up of a diffuse population of old stars with low metallicities and high velocity dispersion. It has zero net rotation near the Sun, whereas further out, it may rotate slightly in the opposite sense to the disc[10] (Carollo et al., 2007). The radial density distribution of the halo is close to a power law $\rho \propto r^{-2.8}$ (Jurić et al., 2008). Most halo stars are on plunging orbits, with their apocentres located at very large galactocentric radii. The metallicity distribution of halo stars is broad but peaks at low metallicities of [Fe/H] = −1.6 (top panel of Fig. 1.11). In the outer parts of the halo, this peak lies around [Fe/H] = −2.2 (Carollo et al., 2007). The most metal-poor star ever discovered lies in the halo and has metallicity [Fe/H] = −5.6 (Frebel et al., 2005). The halo is rich with substructure (Figure. 1.13: 'Field of Streams') much of which is the tidal debris of accreted satellite galaxies, such as the tidal stream of the Sagittarius dwarf spheroidal galaxy. The Galaxy's population of globular clusters reside in the halo, some of which are also known to have significant tidal tails (e.g. Belokurov et al., 2006). Dating of some of these stars has shown that the age of the halo may be close to the age of the Universe.

In addition to the stellar component, the Galaxy is thought to hold a spherical dark halo component which contains around 80% of its total mass. Its presence is inferred from the flat rotation curves of stars and gas in the Milky Way's disc. Without the presence of a large mass in an extended dark halo, the rotation velocity of stars and gas would be expected to fall with increasing galactocentric radius in the disc. The nature of the dark matter, as previously discussed, is unknown but it plays an important role in current cosmological theories of structure formation.

[10]Schönrich et al. (2011) have disputed the authenticity of this duality.

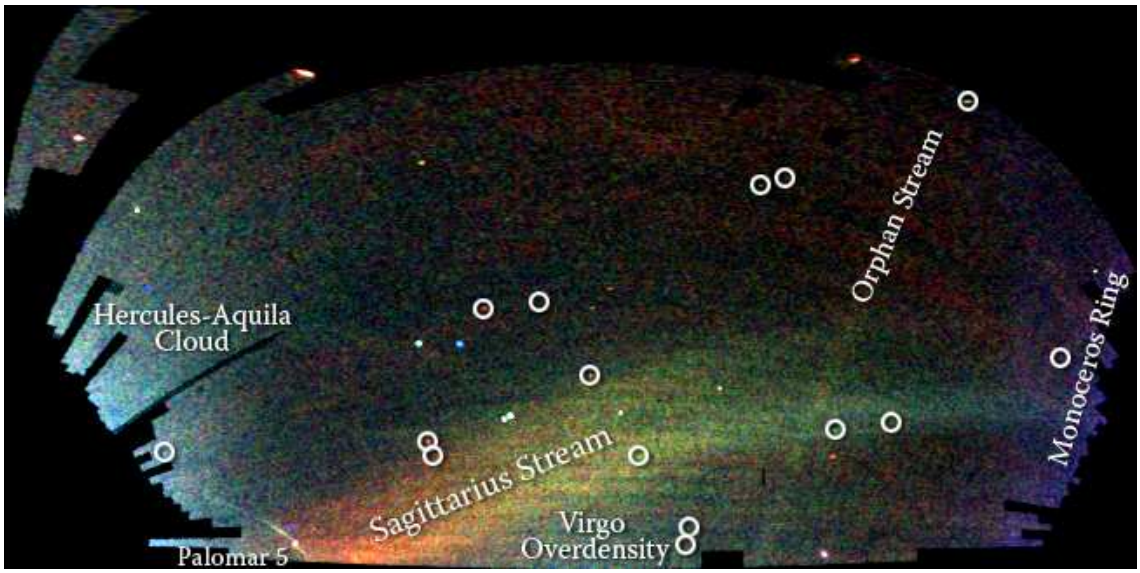

Figure 1.13: A map of stars in the outer regions of the Milky Way Galaxy, derived from the SDSS images of the northern sky, shown in a Mercator-like projection. The colour indicates the distance of the stars, with blue being closer and red further away, while the intensity indicates the density of stars on the sky. Structures visible in this map include streams of stars torn from the Sagittarius dwarf galaxy, a smaller 'orphan' stream crossing the Sagittarius streams, the 'Monoceros Ring' that encircles the Milky Way disc, trails of stars being stripped from the globular cluster Palomar 5, and excesses of stars found towards the constellations Virgo and Hercules. Circles enclose new Milky Way companions discovered by the Sloan Digital Sky Survey (SDSS); two of these are faint globular star clusters, while the others are faint dwarf galaxies. Credit: V. Belokurov and the SDSS.

1.4 The Foundations of Spiral Galaxy Formation

The luminous components of galaxies form through a combination of gravitational clustering and dissipative collapse. In hierarchical structure formation, dark matter 'building blocks' form first. The gas then falls in towards the centre of these building blocks. If these dark matter haloes then merge, angular momentum is transferred from the gas to the dark matter component resulting in a deficiency of specific angular momentum for simulated spiral galaxies[11] in comparison to observations (e.g. Navarro et al., 1995). In order to reconcile hierarchical clustering with a collapsing gaseous sphere, White & Rees (1978) suggested that it was necessary to include energetic feedback from star formation to help prevent gas from collapsing into building blocks. Therefore, in order to accurately model spiral galaxies, it is essential to include baryonic processes such as star formation, feedback from supernovae, stellar winds and metal enrichment.

1.5 Simulating Galaxy Formation

1.5.1 Early Numerical Models

Numerical models of galaxy formation and evolution have the advantage of providing a self-consistent treatment of the kinematics and therefore, the structural evolution of galaxies. Toomre & Toomre (1972) showed, in their pioneering study, that many peculiar features of observed galaxies could be explained due to the gravitational effects of nearby galaxies alone. Larson (1969) was the first to model gas dissipative processes in numerical simulations. His axisymmetric models, which included self-consistent chemical evolution, were successful in reproducing several properties of elliptical (Larson, 1974, 1975) and disc (Larson, 1976) galaxies. These models were improved when gas and star formation processes were treated in a phenomenological way (e.g. Carlberg, 1984).

[11] This has been termed the 'angular momentum catastrophe'.

1.5.2 Semi-Analytic Models

Semi-analytic models (SAMs) aim to connect galactic chemical evolution to structure formation. SAMs can deal with both large-scale structure and evolution in a galaxy halo sized region. The merger history of a halo is constructed either by Monte Carlo realisations of the Press-Schechter formalism, or more recently, directly from numerical dark matter simulations, where the spatial halo distribution with mass accretion and merger histories for each halo is explicitly obtained. Hydrodynamical processes involved in galaxy formation are followed using a set of physical laws or, if the physics is not well understood, phenomenological formalisms. SAMs allow large regions of parameter space to be investigated. Most successful new SAMs include as a minimum, recipes for cosmology, dark haloes, gas cooling, star formation, feedback and chemical enrichment. White & Frenk (1991) developed a basis for modern SAMs to recover observed properties of galaxies. Since that pioneering study SAMs have become more elaborate and can now reproduce fairly well the observed luminosity function, colour-bimodality of galaxies, mass-metallicity relation and Tully-Fisher relation.

The following picture has been established over the past two decades. Gas is collisionally heated when initial density perturbations 'turn around' and collapse to form gravitationally bound structures. Gas in haloes cools via atomic line transitions (depends on density, temperature, metallicity and UV background radiation). Cooled gas collapses to form a rotationally supported disc. Cold gas forms stars, with efficiency a function of gas density (e.g. Schmidt-Kennicutt Law). Massive stars and supernovae reheat cold gas and may expel it together with some metals. Galaxy mergers trigger bursts of star formation with 'major' mergers transforming discs into spheroids (e.g. Kauffmann et al., 1993; Cole et al., 1994; Somerville & Primack, 1999; Cole et al., 2000; Somerville et al., 2001; Croton et al., 2006; Cattaneo et al., 2007; Somerville et al., 2008; De Lucia et al., 2010; Bower et al., 2012).

1.5.3 Semi-cosmological Models

Semi-cosmological simulations start with the collapse of an isolated 'top-hat' sphere of dark and baryonic matter which initially follows the Hubble flow. As their name suggests, these simulations are not fully cosmological since they do not self-consistently treat the large-scale tidal fields. These fields are instead imitated by providing the sphere with a initial degree of solid body rotation, characterised by a dimensionless spin parameter, λ (Peebles, 1971). Small scale density perturbations are then superimposed on the sphere, consistent with the CMB and present day structure of the Universe. Over the years, semi-cosmological simulations have become more detailed and sophisticated, now tracing the baryonic physics processes which are important in galaxy formation and evolution. The properties of the simulated galaxies can be compared to observed galaxies (e.g. Katz & Gunn, 1991; Katz, 1992; Steinmetz & Muller, 1995; Brook et al., 2004b). Although this approach was useful due to its lower computational costs, recent advances in computer performance have made fully cosmological models affordable, hence leading to the declining use of semi-cosmological modelling.

1.5.4 Fully Cosmological Simulations

Fully cosmological simulations are the newest and potentially most powerful tool at the disposal of the computational astrophysicist studying galaxy formation. There are several types. N-body only simulations follow the evolution of the dark matter component (e.g. the Millennium Simulation, Springel et al., 2005b) and are primarily interested in the large-scale structure of the Universe. Here however, only hydrodynamical simulations shall be discussed. These simulations include the important baryonic processes involved in individual galaxy formation such as star formation, feedback and metal enrichment (e.g. Abadi et al., 2003a; Brooks et al., 2007; Okamoto et al., 2008; Guedes et al., 2011; Scannapieco et al., 2012). In fully

cosmological chemodynamical simulations, the strategy is as follows. First, a large-scale dark matter-only, low-resolution simulation is carried out from high redshift to the present epoch. At redshift $z = 0$, a galaxy sized dark matter halo region of interest is selected. The particles that fall into the selected region are traced back to the initial conditions at high redshift, and the volume containing those particles is identified. Within this arbitrarily shaped volume, the low-resolution particles are replaced with particles several times less massive. The initial density and velocities for the less massive particles are then self-consistently calculated by using a special software package (for example: Grafic-2, Bertschinger, 2001), taking into account the density fields of a lower-resolution region. Finally, a simulation of the entire original volume is re-run, including gas dynamics, radiative cooling and star formation. The gas component is only included within the high-resolution region. The surrounding low-resolution region influences the high-resolution region only through gravity. The main downside of fully cosmological simulations is the fact that they are computationally more expensive than all the previous methods. However, advances in computational power have meant that in the last decade, this technique has become more and more feasible. As a result, the majority of studies in this thesis were carried out using fully cosmological simulations.

1.6 Studies in this Thesis

The first two studies in this thesis (Chapters 3 and 4) are based upon detailed analyses of our cosmological chemodynamical simulations, exploring how the star formation history of the bulge and disc affects the observational properties at $z = 0$. This represented our first attempt towards a model prediction in Galactic Archaeology. However, along the way, we also found limitations and problems in the old code. Therefore, in the third study of this thesis (Chapter 5), we test and calibrate a new improved code simulating the evolution of a late-type spiral galaxy in an isolated fixed dark matter halo, for comparison to observational data. The overall

aim of the work in this thesis is to provide a better understanding of the process of galaxy formation and evolution.

1.6.1 Chemodynamical Analysis of Bulge Stars for Simulated Disc Galaxies

In Chapter 3, we analyse the kinematics and chemistry of the bulge stars of two simulated disc galaxies using our chemodynamical galaxy evolution code GCD+. First we compare stars that are born inside the galaxy with those that are born outside the galaxy and are accreted into the centre of the galaxy. Stars that originate outside of the bulge are accreted into it early in its formation within 3 Gyr so that these stars have high [α/Fe] as well as having a high total energy reflecting their accretion to the centre of the galaxy. Therefore, higher total energy is a good indicator for finding accreted stars. The bulges of the simulated galaxies formed through multiple mergers separated by about a Gyr. Since [α/Fe] is sensitive to the first few Gyr of star formation history, stars that formed during mergers at different epochs show different [α/Fe]. We also find that the [Mg/Fe] against star formation time relation can be very useful to identify a multiple merger bulge formation scenario, provided there is sufficiently good age information available. Our simulations also show that stars formed during one of the merger events retain a systematically prograde rotation at the final time. This implies that the orbit of the ancient merger that helped to form the bulge could still remain apparent in the kinematics of bulge stars.

1.6.2 Metallicity Gradients of Disc Stars for a Cosmologically Simulated Galaxy

In Chapter 4, we analyse for the first time the radial abundance gradients of the disc stars of a disc galaxy simulated with our three dimensional, fully cosmological chemodynamical galaxy evolution code GCD+. We study how [Fe/H], [N/O], [O/Fe],

[Mg/Fe] and [Si/Fe] ratios vary with galactocentric radius. For the young stars of the disc, we found a negative slope for [Fe/H] and [N/O] but a positive [O/Fe], [Mg/Fe] and [Si/Fe] slope with radius. By analysing the star formation rate at different radii, we found that the simulated disc contains a greater fraction of young stars in the outer regions, whereas the old stars tend to be concentrated in the inner parts of the disc. This can explain the positive [α/Fe] gradient as well as the negative [N/O] gradient with radius. These radial trends are natural outcomes of an inside-out formation of the disc (regardless of its size) and can thus explain the recently observed positive [α/Fe] gradients in the Milky Way disc open clusters.

1.6.3 Towards a Self-consistent Numerical Model of Late-type Galaxies: Calibrating the Effects of Sub-grid Physics on Galactic Models

In Chapter 5, we carry out several isolated galaxy evolution simulations in a fixed dark matter halo gravitational potential using the new version of our N-body/smoothed particle hydrodynamics (SPH) code `GCD+`. The new code enables us to more accurately model and follow the evolution of the gas and stellar components of the system, including powerful supernovae feedback and its effects on the ISM. Here we present the results of six simulations of an M33-sized late-type disc galaxy each with varying values for our model parameters which include: the star formation efficiency (C_*), the energy released per supernova explosion ($E_{\rm SN}$), and the energy released per unit time from stellar winds ($E_{\rm SW}$). We carry out both a pixel-by-pixel and a radial ring analysis method for each of our galaxies comparing our results to the observed Schmidt-Kennicutt Law and vertical gas velocity dispersion versus radius relation, amongst other tests. We find that our models with higher feedback more closely resemble the observations and that feedback plays a pivotal role in obtaining *both* the observed Schmidt-Kennicutt and gas velocity dispersion relations.

Chapter 2

A Description of the Model and Code: GCD+

2.1 Introduction

In this chapter we describe the method constructed to study the formation and evolution of galaxies in this thesis. The original galactic chemodynamics code GCD+ was developed by Kawata (1999). Kawata & Gibson (2003a) released a major improvement to the code including new Type II supernovae (SNe II) and Type Ia supernovae (SNe Ia) modelling. This version of the code was used in the bulk of the studies in this thesis. Its structure is outlined in detail below. During the course of these studies, a number of enhancements have been made to the Kawata & Gibson (2003a) version of GCD+. As the final study of this thesis employs the new version of the code (Kawata et al., 2009) these enhancements are outlined as well in Section 2.8. Development of GCD+ has been done by D. Kawata (Kawata & Gibson, 2003a; Kawata et al., 2009). However, the code is extensively used for the studies of this thesis, and therefore in this Chapter we describe the GCD+ code.

In GCD+, the dynamics of dark matter and stars are calculated by an N-body

scheme. The dynamics of the gas is calculated using smoothed particle hydrodynamics (SPH). GCD+ is based on earlier codes which combined N-body techniques with the SPH method (e.g. Hernquist & Katz, 1989; Katz et al., 1996). GCD+ can run on most platforms from PCs to clusters to large supercomputers due to it being vectorised and parallelised. Parallelisation is carried out by use of the MPI library. Further details concerning GCD+ can be found in Kawata (1999); Kawata & Gibson (2003a) and Kawata et al. (2009).

2.2 The N-Body Scheme

Bodies are represented by mass particles (or mass points) that are under the influence of forces. The initial conditions are specified, meaning that we know the initial positions and velocities of all bodies in the system. Interactions (forces) between all bodies in the system must be evaluated in order for each body to receive a new position and velocity. This process is carried out regularly so that we obtain information about the time evolution of the system.

The N-body problem is formulated from the set of ordinary differential equations coming from Newton's laws of motion, which can be expressed as

$$\frac{\mathrm{d}\mathbf{x}_i}{\mathrm{d}t} = \mathbf{v}_i, \tag{2.1}$$

$$m_i \cdot \frac{\mathrm{d}\mathbf{v}_i}{\mathrm{d}t} = \mathbf{F}_i, \tag{2.2}$$

where $\mathbf{x}_i$, $\mathbf{v}_i$ and m_i are the position, velocity and mass of the i-th particle, respectively, and $i = 1, 2, ..., N$. The force on particle i is denoted by $\mathbf{F}_i$.

Galaxies are kept together by the force of gravity acting between a large number, N, of bodies. To take this into account, the gravitational interaction between all pairs of bodies will require a sum to be introduced to the right hand side of Equation

(2.2),

$$m_i \cdot \frac{\mathrm{d}\mathbf{v}_i}{\mathrm{d}t} = \sum_{j=1}^{N} \mathbf{F}_{ij}. \tag{2.3}$$

According to Newton's universal law of gravity, the gravitational force is given by

$$\mathbf{F}_{ij} = G \cdot \frac{m_i.m_j}{r_{ij}^3} \cdot \mathbf{x}_{ij}, \tag{2.4}$$

where G is the gravitational constant, $j = 1, 2, ..., N$, $\mathbf{x}_{ij} = \mathbf{x}_i - \mathbf{x}_j$ and $r_{ij} = |\mathbf{x}_i - \mathbf{x}_j|$. Therefore Equation (2.3) simplifies to

$$\frac{\mathrm{d}^2\mathbf{x}_i}{\mathrm{d}t^2} = G \cdot \sum_{j=1}^{N} \frac{m_j}{r_{ij}^3} \cdot \mathbf{x}_{ij}, \tag{2.5}$$

which can be written

$$\frac{\mathrm{d}\mathbf{v}_i}{\mathrm{d}t} = G \cdot \sum_{j=1}^{N} \frac{m_j}{r_{ij}^3} \cdot \mathbf{x}_{ij}. \tag{2.6}$$

From the above, we see that the acceleration of selected body i is independent of its mass. A galaxy is a collisionless system, meaning stars do not noticeably affect each other by close encounters. If a star particle j approaches a star particle i, r_{ij} tends towards zero, and the acceleration will become unnaturally large. This leads to an anomalously high velocity and can result in a star particle leaving the gravitationally bound system. This is also known as two-body heating and can introduce unacceptable numerical errors. In order to enforce collisionless conditions, no two bodies can get too close to each other. Therefore, a gravitational softening length, ϵ, is introduced into the denominator of Equations (2.5 and 2.6) to avoid unrealistic acceleration caused by close encounters (Aarseth, 1963). The softening length is small compared to the galaxy's dimensions. It essentially represents a distance below which the gravitational interaction is suppressed. When the inter-particle distances are large, the softening length has little effect; making the model slightly more collisionless. Stars interact through the 'softened' gravitational force.

Equation (2.5) can be re-written as

$$\frac{\mathrm{d}^2\mathbf{x}_i}{\mathrm{d}t^2} = G \cdot \sum_{j=1}^{N} \frac{m_j}{(r_{ij}^2 + \epsilon_{ij}^2)^{\frac{3}{2}}} \cdot \mathbf{x}_{ij}, \tag{2.7}$$

where $\epsilon_{ij} = (\epsilon_i + \epsilon_j)/2$ and ϵ_i and ϵ_j are the softening lengths of particles i and j. The velocity and position of each star and dark matter particle can be updated by integrating Equation (2.7).

2.2.1 Numerical Techniques

It is not possible to analytically solve the dynamical evolution of a system of N bodies acting under the influence of gravity if $N > 2$. Therefore, numerical methods are required. Perhaps the simplest technique is Euler's method, a first-order numerical procedure for solving ordinary differential equations with a given initial value, assuming that the derivative remains constant between small, finite time intervals Δt. Euler's method is cheap to compute, but inaccurate when compared to other methods. These other methods use more points and higher derivatives to obtain a better estimate of the integral in the point of interest. GCD+ uses a second-order method known as 'leapfrog' which is described below.

Leapfrog Method

The leapfrog method is far more accurate whilst its computational requirements are only slightly greater than Euler's method, making it a far more desirable time integrator. Unlike the Euler integrator, it is second- rather than first-order accurate. The leapfrog method uses derivatives computed at the midpoint of each step. By design, it is very well suited for second order differential systems like problems involving N-bodies. In leapfrog integration, the equations for updating position and velocity are

$$\mathbf{x}^n = \mathbf{x}^{n-1} + \mathbf{v}^{n-\frac{1}{2}} \cdot \Delta t, \tag{2.8}$$

$$\mathbf{v}^{n+\frac{1}{2}} = \mathbf{v}^{n-\frac{1}{2}} + \mathbf{a}^n \cdot \Delta t, \tag{2.9}$$

where $\mathbf{x}^n$ is position at step n, $\mathbf{v}^{n+\frac{1}{2}}$ is the velocity at step $n + 1/2$, $\mathbf{a}^n$ is the acceleration at step n, given in Equation (2.6) and Δt is the size of each timestep. These equations can be expressed in a form which gives velocity at integer steps as

$$\mathbf{x}^{n+1} = \mathbf{x}^n + \mathbf{v}^n \Delta t + \frac{1}{2}\mathbf{a}^n \Delta t^2, \tag{2.10}$$

$$\mathbf{v}^{n+1} = \mathbf{v}^n + \frac{1}{2}(\mathbf{a}^n + \mathbf{a}^{n+1})\Delta t. \tag{2.11}$$

In this method, velocities are integrated one-half of a timestep out of synchrony with their corresponding positions.

2.2.2 Methods for Evaluating the Gravitational Force

Ideally, the dynamical evolution of a galaxy would be modelled with a direct N-body simulation, whereby each body in the system interacts with every other body. This would mean that each body would have $(N-1)$ interactions with other bodies. These interactions must be carried out for each of the N bodies. Therefore, to evaluate the gravitational interactions of a system composed of N bodies, $N(N-1)$ computations are needed, i.e. approximately N^2 computations. Hence, for a galaxy composed of 10^{11} stars, approximately 10^{22} computations are needed. We require many thousands of timesteps to study the formation and evolution of a galaxy. By using Newtons third law, the number of required computations is reduced to $\frac{N}{2}(N-1)$. However, computational complexity is still of the order $O(N^2)$. This direct 'brute-force' computation provides high accuracy at the price of huge computational cost. Therefore, the number of bodies that can be simulated using this method is dramatically limited. Using the special purpose GRAPE hardware, the largest direct N-body simulations now have $N > 10^6$ (Harfst et al., 2007).

The large dynamic range and the expensive evaluation of the force have led to the development of several numerical techniques aimed at obtaining a reliable

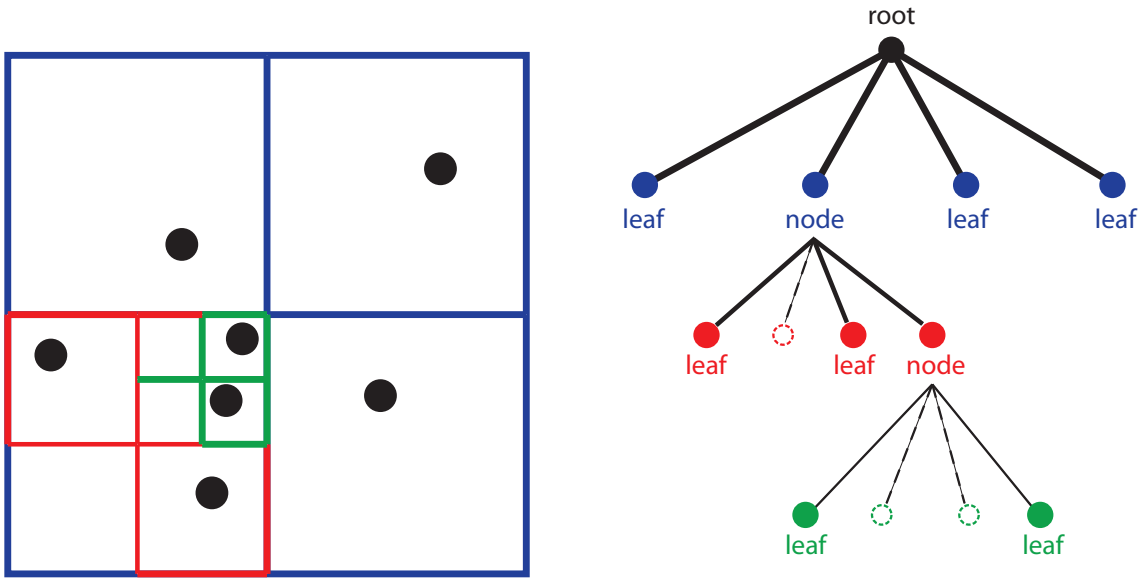

Figure 2.1: An illustration of the Barnes and Hut tree algorithm shown in 2D for simplicity. The Simulation volume with stars is divided into four areas (left). A related quad-tree (right) is constructed (in a clockwise pass in this example) starting at the bottom-right blue square of the simulation volume. Empty squares of the simulated volume are ignored in the tree and are illustrated as transparent circles connected with dotted branches to the parent node. A typical tree structure for an isolated non-interacting galaxy (like the simulations in Chapter 5) is expected to be longer with more branches at the centre and shorter at the edges.

approximate numerical solution to the N-body problem with the minimum amount of computational resources, depending on the astrophysical problem of interest. Below we outline the most successful method for simulations of galaxy formation and evolution and the one which we use in this thesis, the 'Tree' method, which is gridless and based on a particle system.

The Tree Algorithm

Barnes & Hut (1986) introduced a novel algorithm for the fast computation of the gravitational force for collisionless systems such as galaxies, where the force contributions from very distant particles does not need to be computed at very high accuracy. This is achieved by grouping together distant bodies so that the whole group acts as a single particle.

Tree construction begins with a single cell (square in two dimensions and cube in

three dimensions) big enough to contain all the particles. This represents the overall simulated volume and is called the root of the tree. The root cell is then subdivided into 2^d daughter cells having half the side length of the original cell (where d is the number of dimensions). Thus, for a three dimensional cube, the daughter cell will have exactly half the length, width and height of the parent cell, resulting in 8 daughter cells. The tree structure is thus called 'oct-tree'. Cells that do not contain any particles are discarded and are not included in the tree. Cells containing exactly one particle are accepted and the subdivision process is stopped. Cells containing more than one particle are recursively subdivided until only one particle remains in each cell. The tree is usually constructed at every timestep. This recursive subdivision of space into cells can naturally be represented by a hierarchical tree containing leaves, nodes and the root (top-most node). The leaves represent the mass points (particles) and are in the lowest position of the hierarchy. Fig. 2.1 illustrates the method.

The tree method is adaptive for non-homogenous particle distributions, since it automatically adjusts according to the particle distribution. Therefore, it is suitable for astronomical systems such as galaxies, where more bodies are found in the centre and fewer towards the edges.

Every node of the tree contains information about the subcells it contains; including the masses, the position of the centre of mass and higher-order moments. The force on any particle in the system is approximated by passing through the tree starting from its root node. If the centre of mass of a given node containing particles is sufficiently distant from the selected body, the interaction is computed as the force acting between the selected individual body and the centre of mass of the particles in the node. This is the core reason for the speed-up of force computations. If L is the length of the cell currently being processed and D the distance from the cell's centre of mass to the body we are concerned with, and if

$$\frac{L}{D} + \delta < \theta, \tag{2.12}$$

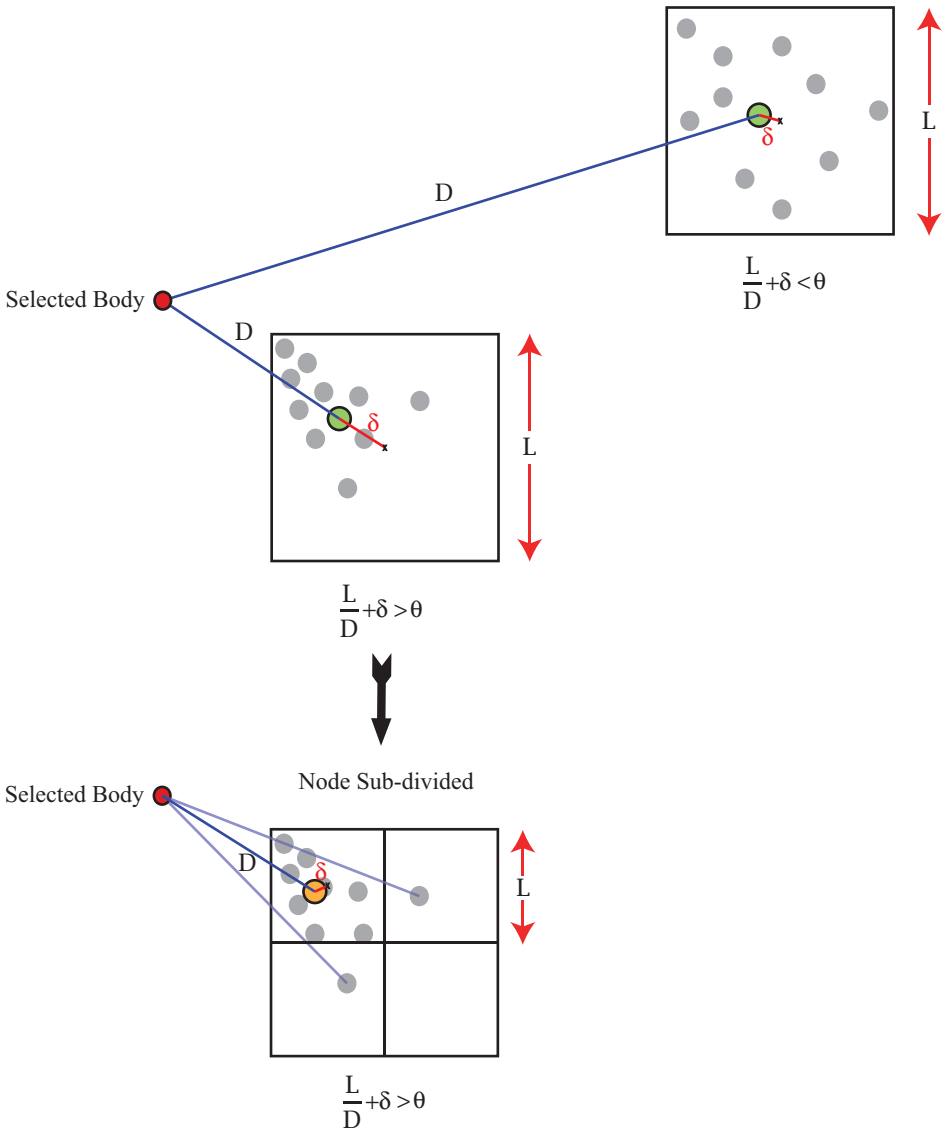

Figure 2.2: If the distance criterion of Equation (2.12) is satisfied, then the force is approximated using the centre of mass of the cell, represented by the green circle. If Equation (2.12) is not satisfied, then the node is subdivided. The orange circle represents the new centre of mass of the top left sub-cell. The distance criterion is then recursively applied to each sub-cell. In the example above, the top left sub-cell may need to be sub-divided further and the force to each particle individually calculated.

where θ is a tolerance parameter which determines the accuracy and thus speed-up and δ is the distance between the geometric centre and the centre of mass of the cell (Dubinski, 1996), then the interaction is approximated as acting in the centre of mass of the whole cell. GCD+ employs $\theta = 0.8$ and uses up to the quadrupole order of mass moments of each node.

If the distance between the selected body and the node (its centre of mass) is close enough, then the node is divided into its daughter cells and a distance check is performed between all of its leaves or sub-nodes and the selected body (see Fig. 2.2). This procedure is executed repeatedly. In the worst time-case scenario, the algorithm will tunnel all the way down from the root to individual leaves (individual particles) and the computational complexity will be the same as in the case of a direct N-body simulation.

The Barnes and Hut tree algorithm greatly reduces the number of required interactions and leads to $O(N \log N)$ number of calculations. This implies that for a (dwarf) galaxy composed of 10^5 stars, only $\sim 5 \times 10^5$ computations are required in contrast to $\sim 10^{10}$ for the direct summation method.

We additionally divide the simulated volume with a space-filling curve. This is beneficial for parallelisation of the code. We use Peano-Hilbert's space-filling curve (Springel, 2005), which completely fills up the simulated volume by passing through every point, using a similar recursive method to tree construction.

2.3 Smoothed Particle Hydrodynamics

In GCD+, gas dynamics are treated using the SPH method originally developed by Lucy (1977) and Gingold & Monaghan (1977). In SPH, gas is represented by discretised particles, which feel additional local forces due to pressure gradients as well as gravitational forces. Each particle has a spatial distance h, known as the 'smoothing length', over which its properties are 'smoothed' by a kernel function (Fig. 2.3). Hence, physical quantities belonging to any particle can be obtained by summing

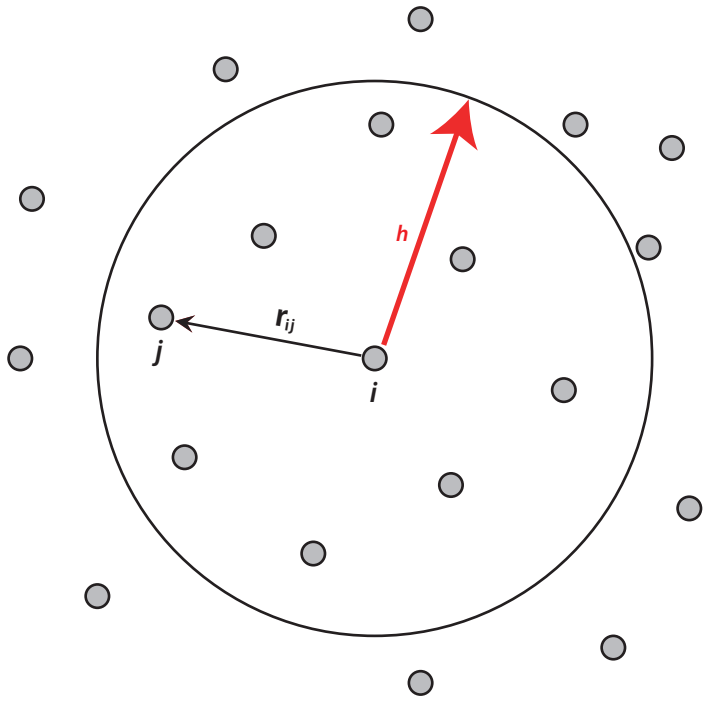

Figure 2.3: The definition of smoothing length h and neighbour particles. The smoothing length is dynamic so that the number of neighbour particles contained within the smoothing length remains roughly constant.

the relevant properties of all the particles which lie within range of the kernel. The kernel concept is important as it minimises local statistical fluctuations in particle numbers. The contributions of each particle to a property are weighted according to their distance, r, from the particle of interest and their density. GCD+ employs a spherically symmetric spline kernel of the form

$$W(r,h) = \frac{8}{\pi h^3} \begin{cases} 1 - 6(r/h)^2 + 6(r/h)^3 & \text{if } 0 \leq r/h \leq 1/2, \\ 2[1-(r/h)]^3 & \text{if } 1/2 \leq r/h \leq 1, \\ 0 & \text{otherwise.} \end{cases} \tag{2.13}$$

We use an update algorithm for the smoothing length based on that employed by Thacker & Couchman (2000). This variable smoothing length means that the resolution of the simulation can be made to automatically adapt itself depending on the local conditions. For example, near the centre of the galaxy where the density

is high, the smoothing length can be made relatively short, producing high spatial resolution. Conversely, far from the centre, where the density is low, the smoothing length can be increased. Thus, the computation is optimised for the different regions of interest. First, neighbouring particles are counted for the i-th particle using the smoothing kernel

$$W_{nn}(r/h_i) = \begin{cases} 1 & \text{if } 0 \leq r/h_i \leq 3/4, \\ \frac{\pi h_i^3}{8} W(4(r/h_i - 3/4)) & \text{if } 3/4 \leq r/h_i \leq 1, \end{cases} \tag{2.14}$$

where r is the distance from the neighbour particle to the i-th particle and $W(x)$ is the same spline kernel as in Equation (2.13). The number of neighbours, $N_{nb,i}$, is a real number rather than an integer, helping alleviate discontinuities in this quantity. Then the smoothing length at timestep $n+1$, h_i^{n+1} is determined by the smoothing length, h_i^n and the number of neighbours, $N_{nb,i}^n$ at the previous timestep n:

$$h_i^{n+1} = h_i^n[1 - a + as], \tag{2.15}$$

where

$$s = \left(\frac{N_s}{N_{nb,i}^n} \right)^{\frac{1}{3}}, \tag{2.16}$$

and N_s is the number of neighbour particles. Motivated by one-dimensional shock-tube tests, we employ $N_s = 40$. The variable, a, changes as a function of the parameter s as

$$a = \begin{cases} 0.2(1 + s^2) & \text{if } s < 1, \\ 0.2(1 + 1/s^3) & \text{if } s \geq 1. \end{cases} \tag{2.17}$$

Physical parameters belonging to each particle, such as the density, ρ, are calculated by

$$\rho_i = \sum_j m_j W(r_{ij}, h_{ij}). \tag{2.18}$$

The acceleration of the i-th particle is given by Euler's equation

$$\frac{d\mathbf{v}_i}{dt} = -\frac{1}{\rho_i}\nabla_i(P + P_{visc}) - \nabla_i\Phi_i, \tag{2.19}$$

where P, P_{visc} and Φ is the pressure, the artificial viscous pressure and the gravitational potential respectively. In GCD+, the gravitational force term of the i-th particle is the sum of the contributions from dark matter, star and gas particles and is given by

$$\nabla_i\Phi_i = -G\sum_j \frac{m_j\mathbf{x}_{ij}}{(r_{ij}^2 + \epsilon_{ij}^2)^{\frac{3}{2}}}. \tag{2.20}$$

GCD+ uses the following smoothed approximation for the pressure-gradient term

$$\frac{1}{\rho_i}\nabla_i(P + P_{visc}) = \sum_j m_j\left(\frac{P_i}{\rho_i^2} + \frac{P_j}{\rho_j^2} + Q_{ij}\right)\nabla_i W(\mathbf{x}_{ij}, h_{ij}), \tag{2.21}$$

where Q_{ij} is the artificial viscosity. The artificial viscosity was developed to allow shocks to be simulated and takes the form

$$Q_{ij} = \begin{cases} \frac{-\alpha v_{s,ij}\mu_{ij} + \beta\mu_{ij}^2}{\rho_{ij}} & \text{if } \mathbf{x}_{ij}.\mathbf{v}_{ij} < 0, \\ 0 & \text{otherwise,} \end{cases} \tag{2.22}$$

with

$$\mu_{ij} = \frac{0.5h_{ij}\mathbf{v}_{ij}.\mathbf{x}_{ij}}{r_{ij} + \eta^2}, \tag{2.23}$$

where $\mathbf{v}_{ij} \equiv \mathbf{v}_i - \mathbf{v}_j$, $\mathbf{v}_{s,ij} = 0.5(\mathbf{v}_{s,i} + \mathbf{v}_{s,j})$ and $\mathbf{v}_{s,i}$ is the sound velocity of the i-th particle. The parameters α and β are chosen to reproduce features of the one-dimensional shock-tube, and govern the amplitude of post-shock oscillations. We employ $\alpha = 0.5$ and $\beta = 1.0$. The parameter η is introduced to prevent numerical divergence. We employ $\eta = 0.05h_{ij}$. A correction is then made in order to reduce the shear component of the artificial viscosity, following the form given in Navarro & Steinmetz (1997)

$$\tilde{Q}_{ij} = Q_{ij}\frac{f_i + f_j}{2}, \tag{2.24}$$

$$f_i = \frac{|\langle \nabla \cdot \mathbf{v} \rangle|}{|\langle \nabla \cdot \mathbf{v} \rangle_i| + |\langle \nabla \times \mathbf{v} \rangle_i| + 0.0002 v_{s,i}/h_i}. \tag{2.25}$$

The velocity divergence and rotation are calculated by

$$\langle \nabla \cdot \mathbf{v} \rangle_i = -\frac{1}{\rho_i} \sum_j m_j \mathbf{v}_{ij} \cdot \nabla_i W(\mathbf{x}_{ij}, h_{ij}), \tag{2.26}$$

$$\langle \nabla \times \mathbf{v} \rangle_{i,x} = -\frac{1}{\rho_i} \sum_j m_j [\mathbf{v}_{ij,z} \nabla_{i,y} W(\mathbf{x}_{ij}, h_{ij}) - \mathbf{v}_{ij,y} \nabla_{i,z} W(\mathbf{x}_{ij}, h_{ij})], \tag{2.27}$$

where $\mathbf{v}_{ij,x} \equiv \mathbf{v}_{i,x} - \mathbf{v}_{j,x}$. If the flow is shear-free and compressive, the corrected viscosity term is identical to the uncorrected term. The velocity and position of each particle is updated by integrating Equation (2.19) using a leapfrog algorithm with individual timesteps (Hernquist & Katz, 1989; Makino, 1991). The timestep of the i-th particle is chosen to be

$$\Delta t_i = \min(0.3\Delta t_{\mathrm{CFL},i}, 0.1\Delta t_{\mathrm{f},i}), \tag{2.28}$$

where Δt_{CFL} is determined by the Courants-Friedrichs-Lewy condition

$$\Delta t_{\mathrm{CFL},i} = \frac{0.5 h_i}{v_{\mathrm{s},i} + 0.6(\alpha v_{\mathrm{s},i} + \beta \mathrm{max}_j |\mu_{ij}|)}, \tag{2.29}$$

and Δt_{f} is determined by the requirement that the force should not change considerably from one timestep to the next. This is achieved by

$$\Delta t_{\mathrm{f},i} = \sqrt{\frac{h_i}{2} \left| \frac{d\mathbf{v}_i}{dt} \right|^{-1}}. \tag{2.30}$$

In a dense region, the smoothing length may become smaller than the softening length, thus requiring a very small timestep. In order to avoid this, we set the lower limit of the smoothing length to be $h_{\mathrm{min}} = \epsilon/2$. For collisionless dark matter and

star particles, the timestep is determined by

$$\Delta t = \min[0.16(\epsilon/v), 0.4(\epsilon/\left|dv/dt\right|)^{1/2}]. \tag{2.31}$$

The leapfrog method is then used to integrate the position and velocity, as follows

$$\mathbf{v}^{n+1/2} = \mathbf{v}^{n} + 0.5\left(\frac{d\mathbf{v}}{dt}(\mathbf{x}^{n}, \tilde{\mathbf{v}}^{n}, ...)\right)^{n} \Delta t^{n\rightarrow n+1}, \tag{2.32}$$

$$\mathbf{x}^{n+1} = \mathbf{x}^{n} + \mathbf{v}^{n+1/2}\Delta t^{n\rightarrow n+1}, \tag{2.33}$$

$$\tilde{\mathbf{v}}^{n+1} = \mathbf{v}^{n+1/2} + 0.5\left(\frac{d\mathbf{v}}{dt}(\mathbf{x}^{n}, \tilde{\mathbf{v}}^{n}, ...)\right)^{n} \Delta t^{n\rightarrow n+1}, \tag{2.34}$$

$$\mathbf{v}^{n+1} = \mathbf{v}^{n+1/2} + 0.5\left(\frac{d\mathbf{v}}{dt}(\mathbf{x}^{n+1}, \tilde{\mathbf{v}}^{n+1}, ...)\right)^{n+1} \Delta t^{n\rightarrow n+1}, \tag{2.35}$$

where $\Delta t^{n\rightarrow n+1}$ represents the time interval between steps n and $n+1$.

The smoothed form of the thermal energy equation used in GCD+ to determine the evolution of the internal energy, u_i, is

$$\frac{du_i}{dt} = \frac{P_i}{\rho_i}\sum_j m_j \mathbf{v}_{ij}\cdot\nabla_i W(\mathbf{x}_{ij}, h_{ij}) + \frac{1}{2}\sum_j m_j Q_{ij}\mathbf{v}_{ij}\cdot\nabla_i W(\mathbf{x}_{ij}, h_{ij}) - \frac{\Lambda_i}{\rho_i} + H_i, \tag{2.36}$$

where Λ/ρ and H are the cooling rate and heating rate per unit mass, respectively. Cooling due to metallicity dependent radiative gas processes is considered using standard cooling curves (Sutherland & Dopita, 1993). Heating due to supernovae feedback is also taken into account.

The minimum timestep between the particles is employed when calculating the time evolution of the internal energy of each particle. Then, the energy equation is integrated semi-implicitly using the trapezoidal rule (Hernquist & Katz, 1989)

$$u^{n+1} = u^{n} + 0.5\left[\left(\frac{du}{dt}\right)^{n} + \left(\frac{du}{dt}\right)^{n+1}\right]\Delta t^{n\rightarrow n+1}. \tag{2.37}$$

Since $(du/dt)^{n+1}$ depends on u^{n+1}, this equation must be solved iteratively. First, a

prediction for the thermal energy $\tilde{u}^{n+1}$ is obtained by assuming that $(du/dt)^{n+1} = (du/dt)^n$. The predicted value $\tilde{u}^{n+1}$ is combined with the predicted velocity $\tilde{\mathbf{v}}^{n+1}$ from Equation (2.34), to estimate the adiabatic term, including the artificial viscosity and the heating in Equation (2.36). Only the cooling term, Λ^{n+1}, is estimated iteratively using the corrected internal energy, once the adiabatic term is obtained. A convergent solution is found using the bisection technique. In order to ensure numerical stability, the radiative cooling is damped as follows (Katz & Gunn, 1991):

$$\left(\frac{du}{dt}\right)_{\rm rad}^{\rm damped} = \frac{a(du/dt)_{\rm rad}}{\sqrt{a^2 + [(du/dt)_{\rm rad}]^2}}, \tag{2.38}$$

$$a = 0.5\frac{u}{\Delta t} + \left(\frac{du}{dt}\right)_{\rm ad}, \tag{2.39}$$

where $(du/dt)_{\rm ad}$ is the change in thermal energy due to adiabatic compression or expansion of the gas, and $(du/dt)_{\rm rad}$ represents the undamped radiative cooling given by Λ/ρ in Equation (2.36).

Finally, the pressure, P, of each gas particle can be obtained by using the equation of state for an ideal gas

$$P = (\gamma - 1)\rho u, \tag{2.40}$$

where u is the specific internal energy and $\gamma = 5/3$ for a monatomic gas.

2.4 Radiative Gas Cooling

To model gas cooling, we use the cooling curves computed by MAPPINGSIII (Sutherland & Dopita, 1993). Using MAPPINGSIII, we have computed the cooling function of the ionization equilibrium gas with various metallicities. Due to the strong role played by metals in radiatively cooling the gas (Källander & Hultman, 1998; Kay et al., 2000), it is important to use metallicity dependent models when calculating the cooling rate. Fig. 2.4 shows the cooling curves utilised in GCD+. With linear interpolation of these cooling curves, the code calculates the cooling rate $\Lambda(T, [{\rm Fe/H}])$,

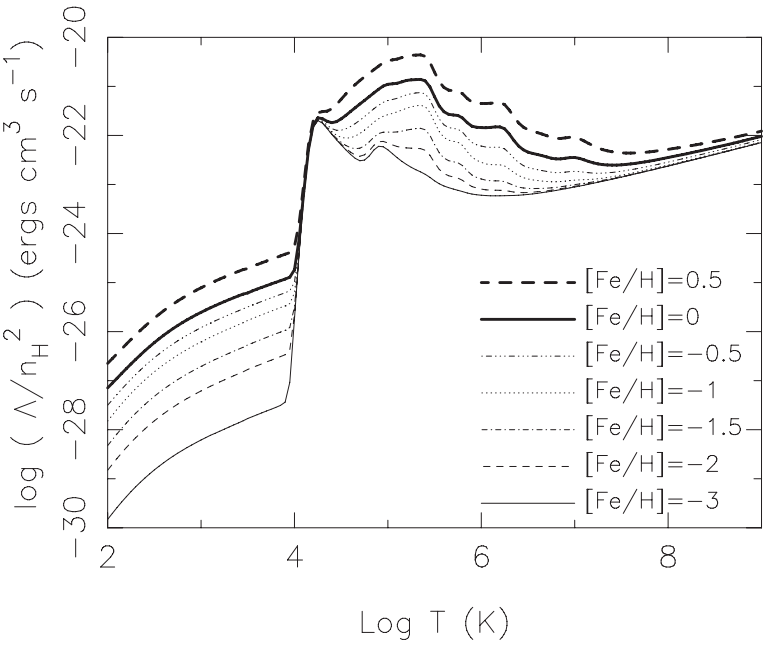

Figure 2.4: Cooling rates, plotted as a function of temperature, for the metallicities indicated (Kawata & Gibson, 2003a). Linear interpolation of these curves is used to calculate cooling rates as a function of temperature and metallicity.

in the metallicity range $-3 <$ [Fe/H] < 0.5, as a function of the temperature and metallicity for each gas particle. To avoid extrapolation, it is assumed that gas with metallicity below [Fe/H] $= -3$ cools at the same rate as gas with [Fe/H] $= -3$, and that gas with metallicity [Fe/H] > 0.5 cools at the same rate as gas with [Fe/H] $= 0.5$.

The temperature for each gas particle is derived by

$$T_i = P_i \mu m_p / (k_{\rm B} \rho_i), \tag{2.41}$$

where P_i and ρ_i are the pressure and density of the i-th particle, and μ, $k_{\rm B}$, and m_p are the mean molecular weight, Boltzmann's constant, and the proton mass, respectively. For simplicity, we fix the mean molecular weight at $\mu = 0.6$, regardless of the metallicity. We set the lower limit of the temperature to be $T_{\rm lim} = 100$ K.

2.5 Star Formation

Star formation is modelled using a method similar to that suggested by Katz (1992) and Katz et al. (1996). In order for a gas particle to be converted into a star particle, the following three criteria must be satisfied:

1. The gas density must be greater than a critical density:
   $\rho_{\rm crit} = 2 \times 10^{-25}$ g cm^{-3}, i.e. $n_{\rm H} \sim 0.1{\rm cm}^{-3}$.

2. The gas velocity field must converge:
   $\nabla \cdot \boldsymbol{v}_i < 0$.

3. The gas must be Jeans unstable:
   i.e. $h/v_s > t_{\rm g}$ where h is the smoothing length, v_s is the speed of sound and $t_{\rm g} = \sqrt{3\pi/16G\rho_{\rm g}}$ is the dynamical time of the gas.

When a gas particle satisfies these conditions and is eligible to form stars, its star-formation rate (SFR) is given by

$$\frac{d\rho_*}{dt} = -\frac{d\rho_{\rm g}}{dt} = \frac{C_*\rho_{\rm g}}{t_{\rm g}}, \tag{2.42}$$

where $d\rho_*/dt$ is the SFR, C_* is a dimensionless SFR parameter and $t_{\rm g}$ is the dynamical time, which is longer than the cooling timescale in the region eligible to form stars. This formula corresponds to the Schmidt law which states that the SFR is proportional to $\rho_{\rm g}^{1.5}$. The star formation efficiency is parametrised by the dimensionless parameter $C_* = 0.5$.

Equation (2.42) implies that the probability, p_*, with which one gas particle transforms entirely into one star particle during a discrete timestep, Δt, is

$$p_* = 1 - \exp(-C_*\Delta t/t_g). \tag{2.43}$$

Transforming all of the gas particle into a star particle, using such a probabilistic approach, avoids creating an intolerably large number of new star particles with different masses. The newly created star particle behaves dynamically as a collisionless particle as described in Section 2.2.

2.6 Initial Mass Function

In GCD+, 'stars' are represented as particles with typical masses around $10^4 - 10^6$ $M_\odot$. Each star particle therefore represents many stars of varying masses, with the relative number distribution of stellar masses within a star particle at its birth being governed by the assumed initial mass function (IMF). In the studies presented in this thesis, the IMF is considered to be universal, with the canonical Salpeter (1955) form adopted. The Salpeter IMF by number, $\Phi(m)$, in each mass interval, dm, is defined as

$$\Phi(m)dm = Am^{-(1+x)}dm, \tag{2.44}$$

where $x = 1.35$ is the Salpeter index corresponding to an IMF by mass proportional to m^{-x}. The coefficient A is determined by the normalization in the specified mass range. The lower and upper mass limits are set to $M_l = 0.1$ $M_\odot$ and $M_u = 60$ $M_\odot$ respectively.

2.7 Feedback

GCD+ takes into account energy feedback and metal enrichment by supernovae, as well as metal enrichment from intermediate mass stars. Both SNe II and SNe Ia are considered. The code calculates the event rates of SNe II and SNe Ia, and the yields of SNe II, SNe Ia, and intermediate mass stars for each star particle at every timestep, by taking into consideration the IMF and stellar lifetimes. The stellar lifetimes are the same as those described by Kodama (1997) and Kodama & Arimoto (1997). GCD+ follows the evolution of the abundances of several chemical

elements: ^{1}H, ^{4}He,^{12}C, ^{14}N, ^{16}O, ^{20}Ne, ^{24}Mg, ^{28}Si, ^{56}Fe, and Z, where Z is the total metallicity. The solar abundances of Woosley & Weaver (1995, hereafter, WW95) are used.

2.7.1 Supernovae

The mass, energy, and heavy elements released by supernovae are smoothed over the neighbouring gas particles using the SPH kernel (Katz, 1992). For example, when the i-th star particle ejects mass $M_{ej,i}$, the incremental change of mass of the j-th neighbour gas particle is

$$\Delta M_{ej,j} = \frac{m_j}{\rho_{\mathrm{g},i}} M_{ej,i} W(r_{ij}, h_{ij}), \tag{2.45}$$

where

$$\rho_{\mathrm{g},i} = \langle \rho_{\mathrm{g}}(\boldsymbol{x}_i) \rangle = \sum_{j \neq i} m_j W(r_{ij}, h_{ij}), \tag{2.46}$$

and $W(x)$ is an SPH kernel (Equation 2.13).

Type II supernovae

The code assumes that each massive star ($\geq$ 8 $\mathrm{M}_{\odot}$) explodes as a SNe II. WW95 provide SNe II yields for stellar masses between 11 and 40 $\mathrm{M}_{\odot}$, and metallicities between 0 and 1 $\mathrm{Z}_{\odot}$. With linear interpolation of these grids, we obtain yields as a function of the stellar mass and metallicity. WW95 considered three different models for $m \geq 30$ $\mathrm{M}_{\odot}$, which differ in the amount of energy imparted by the piston in their models at explosion initiation. Following Timmes et al. (1995), we use the 'B' model in this mass regime. For $m \geq 40$ $\mathrm{M}_{\odot}$, we assume the same abundance ratios for the yields and the same mass fraction for the remnants as those of a 40 $\mathrm{M}_{\odot}$ star. For $\mathrm{Z} \geq \mathrm{Z}_{\odot}$, a simple scaling formula is used, e.g. the yield of carbon from

a star with mass m, and metallicity, Z, is given by

$$m_{\rm ej,C}({\rm Z}, m) = m_{\rm ej,C}({\rm Z}_\odot, m) + m_{\rm ej}({\rm Z}_\odot, m){\rm Z}_{\rm C,\odot}\left(\frac{\rm Z}{{\rm Z}_\odot} - 1\right), \tag{2.47}$$

where $m_{\rm ej,C}$ is the total mass of ejected carbon, including newly synthesised and initial carbon, $m_{\rm ej} = m_{\rm ej,H} + m_{\rm ej,He} + m_{\rm ej,Z}$ indicates the total ejected mass and ${\rm Z}_{\rm C,\odot}$ is the solar abundance of carbon. The yields from stars with initial masses between 8 and 11 $M_\odot$ are still unclear (e.g. Hashimoto et al., 1993). Hence, we simply interpolate linearly between the yields for the lowest mass, i.e. $\sim$ 11 $M_\odot$ star in WW95 and those for the highest mass, i.e. 8 $M_\odot$ star in van den Hoek & Groenewegen (1997), as mentioned in the next section.

Type Ia supernovae

We adopt the SNe Ia model proposed by Kobayashi et al. (2000), hereafter KTN00. This model is different from the conventional one proposed by Greggio & Renzini (1983). Details of this model are described in KTN00. Here, we briefly explain this model and implementation in our code. Following KTN00, SNe Ia are assumed to occur in binary systems which consist of primary and companion stars with appropriate masses and metallicities ([Fe/H] ≥ -1.1). The primary stars have main-sequence mass in the range of $m_{p,l} = 3$ $M_\odot$ and $m_{p,u} = 8$ $M_\odot$, and evolve into the C+O white dwarf (WD). The mass range of companion stars is restricted to between $m_{d,RG,l} = 0.9$ $M_\odot$ and $m_{d,RG,u} = 1.5$ $M_\odot$ and between $m_{d,MS,l} = 1.8$ $M_\odot$ and $m_{d,MS,u} = 2.6$ $M_\odot$. KTN00 designate the binary system whose companion has the mass within the former (latter) mass range 'RG+WD (MS+WD) system'. Finally, the total number of SNe Ia, as a function of age, t, of a star particle with a mass of m_s $M_\odot$, is given by

$$N_{\rm SNeIa}(t) \;=\; m_s \int_{m_{p,l}}^{m_{p,u}} m^{-(1+x)} dm \left\{ \int_{M_l}^{M_u} m^{-x} dm \right\}^{-1}$$

$$\times \left[b_{\rm MS} \frac{\int_{\max(m_{d,MS,l}, m_t)}^{m_{d,MS,u}} \Phi_d(m) dm}{\int_{m_{d,MS,l}}^{m_{d,MS,u}} \Phi_d(m) dm} + b_{\rm RG} \frac{\int_{\max(m_{d,RG,l}, m_t)}^{m_{d,RG,u}} \Phi_d(m) dm}{\int_{m_{d,RG,l}}^{m_{d,RG,u}} \Phi_d(m) dm} \right], \quad (2.48)$$

where m_t is the mass of the star whose lifetime is equal to t, and the mass function of the companion stars is assumed to be $\Phi_d(m) \propto m^{-1.35}$ by number, following KTN00. The term before the square bracket indicates the number of C+O WDs, i.e. primary stars. The first term within the square bracket determines what fraction of C+O WDs evolve into SNe Ia from the MS+WD systems, and the second term determines what fraction of C+O WDs evolve into SNe Ia from the RG+WD systems. Following KTN00, we set $b_{\rm MS} = 0.05$ and $b_{\rm RG} = 0.02$. The nucleosynthesis prescriptions for SNe Ia are taken from the W7 model of Iwamoto et al. (1999).

Initially, metals are only ejected by SNe II. This continues for the time taken by a 8 $M_\odot$ star to die (~ 0.04 Gyr in the case of $\log Z/Z_\odot = 0$, where $Z_\odot = 0.019$). Oxygen is produced mainly by SNe II. After SNe II cease, the continuous ejection of oxygen is mainly due to the contribution from intermediate mass stars. On the other hand, a significant fraction of iron is produced by SNe Ia. Stars with $\log Z/Z_\odot = 0$ lead to SNe Ia, depending on the lifetime of their companion stars. SNe Ia occur in MS+WD (RG+WD) systems in the age range of $0.7 - 1.5$ (> 2.8) Gyr. However, a star particle with $\log Z/Z_\odot = -2$ does not lead to SNe Ia, because the above SNe Ia model restricts the metallicity range for progenitors of SNe Ia to [Fe/H] ≥ -1.1. For simplicity, we assume that the metallicity range for SNe Ia is $\log Z/Z_\odot \geq -1.1$, instead of [Fe/H] ≥ -1.1. In the implementation, the code possesses a look-up table of the yields of all the chemical elements, remnant masses, number of supernovae as a function of the age and metallicity, and calculates those values for each star particle at every timestep.

Intermediate mass stars

The yields and remnant masses for intermediate mass stars (≤ 8 $M_\odot$) are taken from van den Hoek & Groenewegen (1997) who present the yields of ^{1}H, ^{4}He, ^{12}C, ^{13}C, ^{14}N, and ^{16}O for stars with initial masses between 0.8 and 8 $M_\odot$ and initial metallicities of $Z = 0.001 - 0.04$. We do not use ^{13}C yields. They also provide the newly formed and ejected metals unlike WW95, who present the total ejected metals. Therefore, we calculate the total ejected metals using Table 1 of van den Hoek & Groenewegen (1997) for H, He, C, N, and O and the initial abundances for the other elements, i.e. Ne, Mg, Si, and Fe, which are simply scaled to the solar abundance set. As for stars with $Z > 0.04$, we use the same scaling as Equation (2.47) based on $Z = 0.04$ yields. For $Z < 0.001$, we simply assume the same yields as $Z = 0.001$. Whilst this simple assumption may overestimate the ejected metals, since the metals are ejected from intermediate mass stars at a later time than those from SNe II, which eject much larger amounts of metals, this simplification should not affect the final metallicity. Nevertheless, knowledge of the yields for low and zero metallicity stars is important in studies of the chemical composition of extremely metal poor objects observed at both low and high redshifts, although it is not yet well-established.

2.7.2 Energy Feedback

One of the most difficult and most critical processes to model in galaxy formation simulations is the way by which the energy feedback from supernovae affects the surrounding gas. GCD+ adopts a simple model proposed by Navarro & White (1993), which assumes that the energy produced by supernovae affects only the temperature and velocity field of the surrounding gas, and its effect is implemented by increasing the thermal ($E_{\rm th}$) and kinetic ($E_{\rm kin}$) energy of the gas neighbours of each star particle that has a supernova (SN) event, by an amount corresponding to the energy released by the SN (Kawata & Gibson, 2003a). A parameter, $f_v = E_{\rm kin}/(E_{\rm kin} + E_{\rm th})$, defines the fraction of the available energy to perturb the gas velocity field; the rest of the

energy of the supernovae contributes to the increase in the thermal energy of the gas (Kawata, 2001). It is known that kinetic feedback affects the history of star formation more strongly than thermal feedback, which quickly dissipates due to efficient radiative cooling where the gas density is high enough to form stars. We assume that each SN yields an energy of $\epsilon_{\rm SN} \times 10^{51}$ erg, and that

$$E_{\rm kin} = f_v \epsilon_{\rm SN} 10^{51} {\rm erg}, \tag{2.49}$$

where $\epsilon_{\rm SN}$ controls the amount of supernovae energy released and f_v controls the effect of the released supernovae energy (Kawata, 2001; Navarro & White, 1993). Since an initial SN energy is yet to have been established quantitatively, the available SN energy, $\epsilon_{\rm SN}$, as well as f_v, are treated as free parameters. We adopt $\epsilon_{\rm SN} = 0.1$ and $f_v = 0$ in the simulations in Chapters 3 and 4 corresponding to almost negligible feedback effects.

The problems associated with implementing feedback in galaxy formation and evolution simulations are explored in some detail in the final chapter of this thesis. It is important to be aware of these issues and their potential effects on simulation results.

2.8 Updated GCD+

Thus far, the 2003 version of the Galactic chemodynamics software package GCD+ has been outlined. However, work on this code is ongoing, as new techniques are developed to better simulate galaxy evolution. During the course of this thesis, a number of enhancements to the original code have been implemented. Here the new features of the code are described. Further details of the new version of GCD+ can be found in Kawata et al. (2009) and Rahimi & Kawata (2012).

2.8.1 Modern Scheme of SPH

We have implemented a modern scheme of SPH closely following the methodology of Rosswog & Price (2007). As such, we only outline the final formulae adopted, and refer the interested reader to Rosswog & Price (2007) for their formal derivation. The smoothing length is determined by

$$h_i = \eta \left(\frac{m_i}{\rho_i} \right)^{1/3}, \tag{2.50}$$

where $\eta = 3.0$ is adopted and where the density ρ_i is given by

$$\rho_i = \sum_j m_j W(r_{ij}, h_i). \tag{2.51}$$

The solution of Equation (2.50) is calculated iteratively until the relative change between two iterations is smaller than 10^{-3} (see Price & Monaghan, 2007, for more details). Euler's equation is written as

$$\begin{aligned} \frac{d\mathbf{v}_i}{dt} &= -\sum_j m_j \left\{ \frac{P_i}{\Omega_i \rho_i^2} \nabla_i W_{ij}(h_i) + \frac{P_j}{\Omega_j \rho_j^2} \nabla_i W_{ij}(h_j) \right\} \\ &+ Q_{v,i} \\ &- G \sum_j m_j \left\{ \frac{\phi'_{ij}(h_i) + \phi'_{ij}(h_j)}{2} \right\} \mathbf{e}_{ij} \\ &- \frac{G}{2} \sum_j m_j \left\{ \frac{\zeta_i}{\Omega_i} \nabla_i W_{ij}(h_i) + \frac{\zeta_j}{\Omega_j} \nabla_i W_{ij}(h_j) \right\}. \end{aligned} \tag{2.52}$$

The first term of Equation (2.52) corresponds to the pressure gradient, where $W_{ij}(h_i) = W(r_{ij}, h_i)$, $\nabla_i W_{ij}(h_i) = \partial W(r_{ij}, h_i)/\partial \mathbf{x}_i$ and

$$\Omega_i = 1 - \frac{\partial h_i}{\partial \rho_i} \sum_k \frac{\partial W_{ik}(h_i)}{\partial h_i}. \tag{2.53}$$

From Equation (2.50), $\partial h_i/\partial \rho_i = -h_i/(3\rho_i)$. The second term of Equation (2.52) corresponds to the artificial viscosity,

$$Q_{v,i} = \begin{cases} -\left(\sum_j m_j \frac{\alpha_{ij}^{\rm AV}(t) v_{\rm sig} \mathbf{v}_{ij}\cdot\mathbf{e}_{ij}}{\rho_{ij}}\right) \overline{\nabla_i W_{ij}} & \text{if } \mathbf{x}_{ij}.\mathbf{v}_{ij} < 0, \\ 0 & \text{otherwise,} \end{cases} \tag{2.54}$$

where $\mathbf{v}_{ij} = \mathbf{v}_i - \mathbf{v}_j$, $\mathbf{e}_{ij} = (\mathbf{x}_i - \mathbf{x}_j)/|\mathbf{x}_i - \mathbf{x}_j|$, $\rho_{ij} = (\rho_i + \rho_j)/2$ and

$$\overline{\nabla_i W_{ij}} = \frac{1}{2}\left\{\frac{1}{\Omega_i}\nabla_i W_{ij}(h_i) + \frac{1}{\Omega_j}\nabla_i W_{ij}(h_j)\right\}. \tag{2.55}$$

The signal velocity, $v_{\rm sig}$, adopted is

$$v_{\rm sig} = \frac{v_{s,i} + v_{s,j} - \mathbf{v}_{ij}\cdot\mathbf{e}_{ij}}{2}, \tag{2.56}$$

where $v_{s,i}$ is the sound velocity of the i-th particle. The amount of artificial viscosity is controlled by a time-dependent parameter,

$$\alpha_{ij}^{\rm AV} = \frac{1}{4}(\alpha_i^{\rm AV}(t) + \alpha_j^{\rm AV}(t))(f_i + f_j), \tag{2.57}$$

where f_i is given in Equation (2.25) in order to suppress artificial viscosity in pure shear flows. The viscous parameter $\alpha_i^{\rm AV}(t)$ varies with time. Rosswog & Price (2007) suggested the following function to evolve this viscous parameter (see also Morris, 1997):

$$\frac{\alpha_i^{\rm AV}}{dt} = -\frac{\alpha_i^{\rm AV} - \alpha_0}{\tau_i} + S_i, \tag{2.58}$$

where $\alpha_0 = 0.5$ and

$$\tau_i = \frac{h_i}{0.2 v_{s,i}}. \tag{2.59}$$

The source term is given by

$$S_i = \max(-\nabla_i \cdot v_i, 0)(2 - \alpha_i^{\rm AV}), \tag{2.60}$$

The maximum of the viscous parameter is set to be $\alpha_{\rm max}^{\rm AV} = 2$. This parameter is important as it determines how well strong shocks are captured. Following Springel & Hernquist (2002), instead of the energy equation, we follow the entropy equation, which is written as

$$\frac{{\rm d}A_i}{{\rm d}t} = \frac{\gamma - 1}{\rho^{\gamma-1}} Q_{u,i}, \tag{2.61}$$

where $A_i = P_i/\rho_i^{\gamma} = ((\gamma-1)/\rho_i^{\gamma-1})u_i$ is entropy and u_i is the thermal energy of the i-th particle. $Q_{u,ij}$ is zero if $\mathbf{x}_{ij} \cdot \mathbf{v}_{ij} > 0$. Otherwise, it is described by

$$Q_{u,i} = -\sum_j \frac{m_j v_{\rm sig}}{\rho_{ij}} \left\{ \frac{\alpha_{ij}^{\rm AV}}{2} (\mathbf{v}_{ij} \cdot \mathbf{e}_{ij})^2 - \alpha_{ij}^{\rm C} (u_i - u_j) \right\} \times \mathbf{e}_{ij} \cdot \overline{\nabla_i W_{ij}}, \tag{2.62}$$

where $\alpha_{ij}^{\rm C} = (\alpha_i^{\rm C} + \alpha_j^{\rm C})/2$. The second term within the parentheses of Equation (2.62) corresponds to the artificial thermal conductivity (Rosswog & Price, 2007; Price, 2008). The artificial conductivity parameter, $\alpha^{\rm C}$, evolves following

$$\frac{d\alpha_i^{\rm C}}{dt} = -\frac{\alpha_i^{\rm C}}{\tau_i} + S_i^{\rm C}, \tag{2.63}$$

where the source term is

$$S_i^{\rm C} = 0.05 h_i |\nabla^2 u_i| / \sqrt{u_i}, \tag{2.64}$$

and

$$\nabla^2 u_i = 2 \sum_j m_j \frac{u_i - u_j}{\rho_j} \frac{\mathbf{e}_{ij} \cdot \overline{\nabla_i W_{ij}}}{r_{ij}}. \tag{2.65}$$

After implementing the above scheme, the new code is able to resolve Kelvin-Helmholtz instabilities (KHI). Whilst adaptive mesh refinement (AMR) codes have been able to resolve KHI, traditional SPH codes have not, leading Agertz et al. (2007) to argue that this is a fundamental problem for SPH. However, Kawata et al. (2009) demonstrate that the new version of the code can capture KHI, thus confirming that the new SPH scheme of Rosswog & Price (2007) appears to rectify this apparent fundamental problem of SPH.

2.8.2 Adaptive Softening

The updated code now also includes adaptive softening for both the stars and gas although in this thesis study (Chapter 5) we only implement it for the gas particles. The third term of Equation (2.52) corresponds to the gravitational force, and employs the adaptive gravitational force softening suggested in Price & Monaghan (2007), where the softening length is matched to that of the smoothing length. The fourth term of Equation (2.52) is the correction term for adaptive softening, where

$$\zeta_i = \frac{\partial h_i}{\partial \rho_i} \sum_j m_j \frac{\partial \phi_{ij}(h_i)}{\partial h_i}. \tag{2.66}$$

We apply the cubic spline softening kernel of Equation (2.13). The corresponding force kernel is given by

$$\phi' = \frac{4\pi}{r^2} \int_0^r W r'^2 dr'. \tag{2.67}$$

The softened form of the gravitational force $\phi^{'}$ is found by integrating the softening kernel according to Equation (2.67), giving:

$$\phi'(r,h) = \begin{cases} 4/h^2 \left(\frac{8}{3}q - \frac{48}{5}q^3 + 8q^4\right), & 0 \le q < 1/2; \\ 4/h^2 \left(\frac{16}{3}q - 12q^2 + \frac{48}{5}q^3 - \frac{8}{3}q^4 - \frac{1}{60q^2}\right), & 1/2 \le q < 1; \\ 1/r^2, & q \ge 1, \end{cases} \tag{2.68}$$

where $q = r/h$. Integrating a second time gives the gravitational potential kernel. The derivative of the potential with respect to h is given by

$$\frac{\partial \phi}{\partial h} = \begin{cases} 2/h^2 \left(-8q^2 + 24q^4 - \frac{96}{5}q^5 + \frac{7}{5}\right), & 0 \le q < 1/2; \\ 2/h^2 \left(-16q^2 + 32q^3 - 24q^4 + \frac{32}{5}q^5 + \frac{8}{5}\right), & 1/2 \le q < 1; \\ 0. & q \ge 1. \end{cases} \tag{2.69}$$

For collisionless N-body particles, only the gravitational force term of Equation (2.52) is taken into account, as follows:

$$\begin{aligned}\frac{d\mathbf{v}_i}{dt} &= -G\sum_j m_j \left\{\frac{\phi'_{ij}(h_i)+\phi'_{ij}(h_j)}{2}\right\}\mathbf{e}_{ij} \\ &- \frac{G}{2}\sum_j m_j \left\{\frac{\zeta_i}{\Omega_i}\nabla_i W_{ij}(h_i)+\frac{\zeta_j}{\Omega_j}\nabla_i W_{ij}(h_j)\right\}. \end{aligned} \tag{2.70}$$

2.8.3 Individual Timestep Limiter

For SPH particles, we apply an individual timestep scheme to integrate Equations (2.52) and (2.61), and for collisionless particles we use Equation (2.70). The timestep for SPH particles is based upon $dt_i = \min(dt_{\mathrm{CFL},ij}, dt_{\mathrm{DYN},i})$, where the Courant-Friedrich-Levy condition is calculated by

$$dt_{\mathrm{CFL},ij} = C_{\mathrm{CFL}}\frac{0.5h_i}{v_{dt,ij}}, \tag{2.71}$$

where $v_{dt,ij} = v_{\mathrm{sig},ij}$ if $\mathbf{x}_{ij}\cdot\mathbf{v}_{ij} < 0$, otherwise $v_{dt,ij} = 0.5(v_{s,i}+v_{s,j}+\mathbf{v}_{ij}\cdot\mathbf{e}_{ij})$. We set $C_{\mathrm{CFL}} = 0.2$ in our study (Chapter 5) based on the requirement for one-dimensional shock-tube tests. The requirement that the force should not change significantly within one timestep is satisfied by

$$dt_{\mathrm{DYN},i} = C_{\mathrm{DYN}}\left(\frac{0.5h_i}{|dv_i/dt|}\right)^{1/2}. \tag{2.72}$$

We set $C_{\mathrm{DYN}} = 0.2$ for SPH particles. The timestep for collisionless particles is derived solely from Equation (2.72), and we adopt $C_{\mathrm{DYN}} = 0.2$.

Allowing particles to have different timesteps leads to a significant reduction in computational time, since there is large variation in the timescales of particles in galaxy simulations. For example, particles in the outer region of a galaxy can have a larger timestep and hence do not need to be integrated as often as particles located in the inner region. Whilst almost all implementations of the individual

timestep method for a particle system violate Newton's third law, as long as physical quantities are integrated with sufficient accuracy, this violation is not a severe problem. However, such accuracy cannot always be maintained, especially when a sudden change occurs, such as a SN explosion. The SN explosion will generate a bubble with a dense shocked-shell which will expand into the cold relatively diffuse surrounding gas. The difference in timesteps between the gas in the shell and the cold gas can become very large (Equation 2.29). In this kind of situation, a naive implementation of the individual timestep scheme assigns a much larger timestep to the surrounding cold gas, such that it can be longer than the arrival time of the expanding shell, because the timestep criteria is measured well before the shell reaches the neighbourhood of the cold gas. This leads to an unacceptably large error in the evolution of these particles, since the surrounding cold gas may not react to the explosion until after the blast wave has already passed. In order to resolve this problem, as suggested by Saitoh & Makino (2009), we have added the individual timestep limiter which is crucial for correctly resolving the expansion bubbles induced by supernovae feedback (see also Merlin et al., 2010; Durier & Dalla Vecchia, 2012). The timestep limiter works by enforcing

$$dt_i \leq 4 \times \min(dt_j) \quad \text{and} \tag{2.73}$$

$$dt_j \leq 4 \times \min(dt_i), \tag{2.74}$$

where dt_i is the timestep of the ith particle and dt_j is the timestep of all neighbouring particles. At every timestep, particle i checks the minimum timestep of all particles within its smoothing length, i.e. $r_{ij} < h_i$ or $r_{ij} < h_j$. If $dt_i > \min(dt_j)$, the i-th particle lowers its timestep to $dt_i = 4 \times \min(dt_j)$. With this simple timestep limiter, the behaviour of an explosion integrated by individual timesteps essentially becomes the same as that integrated by global timesteps (Saitoh & Makino, 2009).

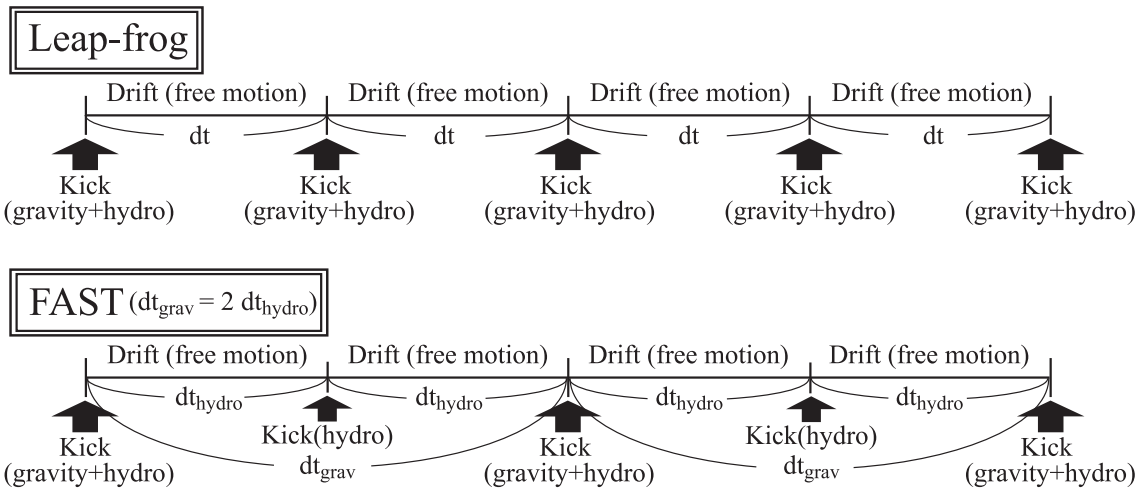

Figure 2.5: The schematic picture of the leapfrog and FAST methods for the integration of a self-gravitating fluid. 'Kick' means the momentum exchanges between particles, while 'Drift' denotes the free (inertial) motions under given velocity vectors. From Saitoh & Makino (2010).

2.8.4 FAST Scheme

The new code implements the Fully Asynchronous Split Time-Integrator (FAST) scheme (Saitoh & Makino, 2010) for the integration of self-gravitating fluid systems using the SPH method. FAST allows the use of different timesteps for integrating hydrodynamics and gravity by splitting the Hamiltonian of the self-gravitating system. Fig. 2.5 shows a schematic of the new scheme and a comparison with the older method. Previously, the gravitational timestep ($\mathrm{dt_{grav}}$) was equal to the hydrodynamical timestep ($\mathrm{dt_{hydro}}$), however with the FAST scheme, the code allows $\mathrm{dt_{grav}} \geq 2^l \times \mathrm{dt_{hydro}}$, where l is a natural number which adaptively changes. Here, $\mathrm{dt_{grav}}$ for SPH particles is measured by

$$dt_{\mathrm{grav},i} = C_{\mathrm{DYN}} \frac{0.5 h_i}{|(dv_i/dt)_{\mathrm{grav}}|}, \tag{2.75}$$

where $(dv_i/dt)_{\mathrm{grav}}$ is the acceleration due to self-gravity only. The schematic shows an example when $l = 1$. In this case, the computational cost of the gravitational force becomes half that of the leapfrog method. FAST results in a significant reduction in the total calculation time of the simulation, with minimal sacrifice to the accuracy

of the time integration.

2.8.5 Radiative Cooling and Heating

Radiative cooling and heating is calculated with CLOUDY (v08.00: Ferland et al., 1998). We tabulate cooling and heating rates and the mean molecular weight as a function of redshift, metallicity, density and temperature adopting the 2005 version of the Haardt & Madau (1996) UV background radiation. We also add a thermal energy floor following Robertson & Kravtsov (2008) to keep the Jeans mass higher than $2N_{\rm nb}m_{\rm p}$, where $N_{\rm nb}$ is the number of neighbour particles and $m_{\rm p}$ is the particle mass, to avoid numerical instability (see also Bate & Burkert, 1997). We no longer apply damping to radiative cooling as described in Equations (2.38) and (2.39).

2.8.6 Star Formation and Gas Restitution

The new version of GCD+ uses a different scheme for star formation and feedback. We now keep the mass of the baryon (gas and star) particles completely the same, unlike Kawata & Gibson (2003b) or the majority of SPH simulations which include star formation. Although the basic strategy is similar to Lia et al. (2002) and Martínez-Serrano et al. (2008), a slightly different implementation is adopted (Fig. 2.6).

First, every star particle formed in the simulation is randomly assigned a mass group ID ranging from 1 to 61 (although 61 is chosen arbitrarily, it is a compromised selection to sample the stellar mass range and be similar to our resolution, i.e. number of neighbour particles).

We can calculate that about 13 per cent of the mass is ejected by SNe II from a star cluster following the assumed IMF and WW95. Therefore we set ID $= 1 - 8$ particles to be 'SNe II particles'. Each SNe II particle receives 1/8 of the energy and metals produced by SNe II depending on the age and initial metallicity. After the age reaches a time when 8/61 of the mass is ejected (about the lifetime of a 8 $M_\odot$ star, depending on metallicity), the whole star particle is changed back to a gas

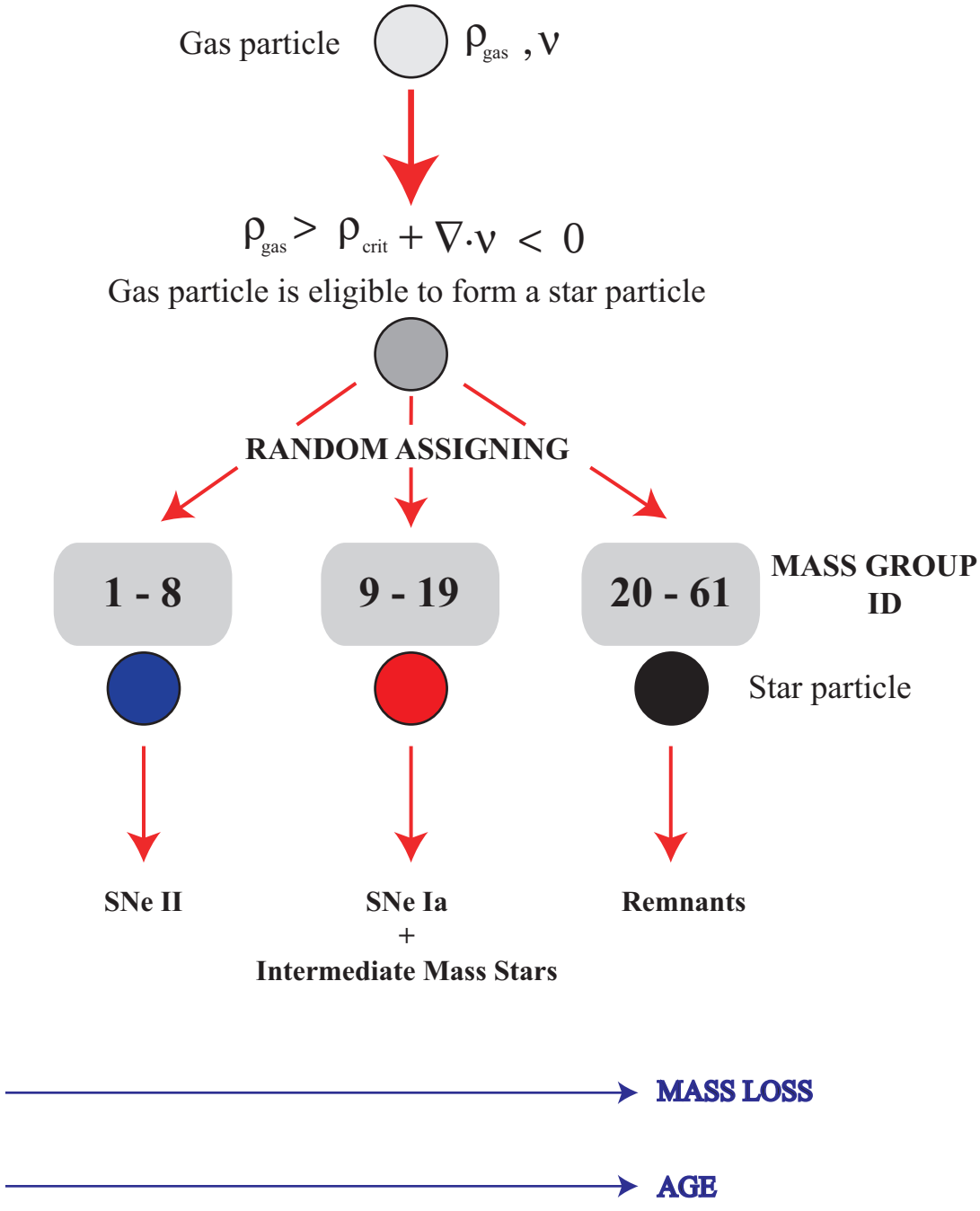

Figure 2.6: When a gas particle forms a star particle, it is randomly assigned a mass group ID ranging from 1-61. The mass group assigned to the newly formed star particle will determine its subsequent evolution. The lower the ID, the more massive the star.

particle.

From the IMF, about 30 per cent of the mass will be ejected after a cosmic time. Therefore, star particles with IDs ranging from 9 to 19 will turn back into a gas particle depending on the age of the star particle, which models the mass-loss from intermediate-mass stars and SNe Ia feedback.

2.8.7 Feedback

We assume each SN produces thermal energy, $E_{\rm SN}$ (erg). We also assume that stellar winds from massive stars (> 30 M$_\odot$) produce thermal energy, $E_{\rm SW}$ (erg s^{-1}) and add this to the supernovae particles. Consequently SNe II particles have higher temperature and become metal rich. We do not take into account radiative cooling until the particle turns back to a gas particle. However, we calculate thermal energy for the SNe II particles following the SPH scheme and add the pressure from the SNe II particles to their neighbour particles, while the dynamics of the SNe II particles are only affected by gravity (see also Pelupessy et al., 2004). The metals produced by SNe II are also distributed from the SNe II particles through the metal diffusion scheme of Greif et al. (2009), i.e. the metal diffusion applied to the SNe II particles is the same as for the other normal gas particles.

For ID 9−19 particles, we turn on radiative cooling during their mass loss and SNe Ia. For example, ID 9 particles with solar metallicity represent mass-loss from $7-5.6$ M$_\odot$ stars (Fig. 2.7). Once they become older than the lifetime of a 7 M$_\odot$ star, they become a 'feedback particle'. The particle inherits the original metal abundance and receives further additional metals produced by stars in this mass range (van den Hoek & Groenewegen, 1997), which are then spread via the metal diffusion scheme applied. Their thermal energy is calculated with the SPH scheme, and the additional pressure from these feedback particles is applied to their neighbouring particles (important especially for the higher ID particles with SNe Ia feedback). Once the particle becomes older than the lifetime of a 5.6 M$_\odot$ star, the particle

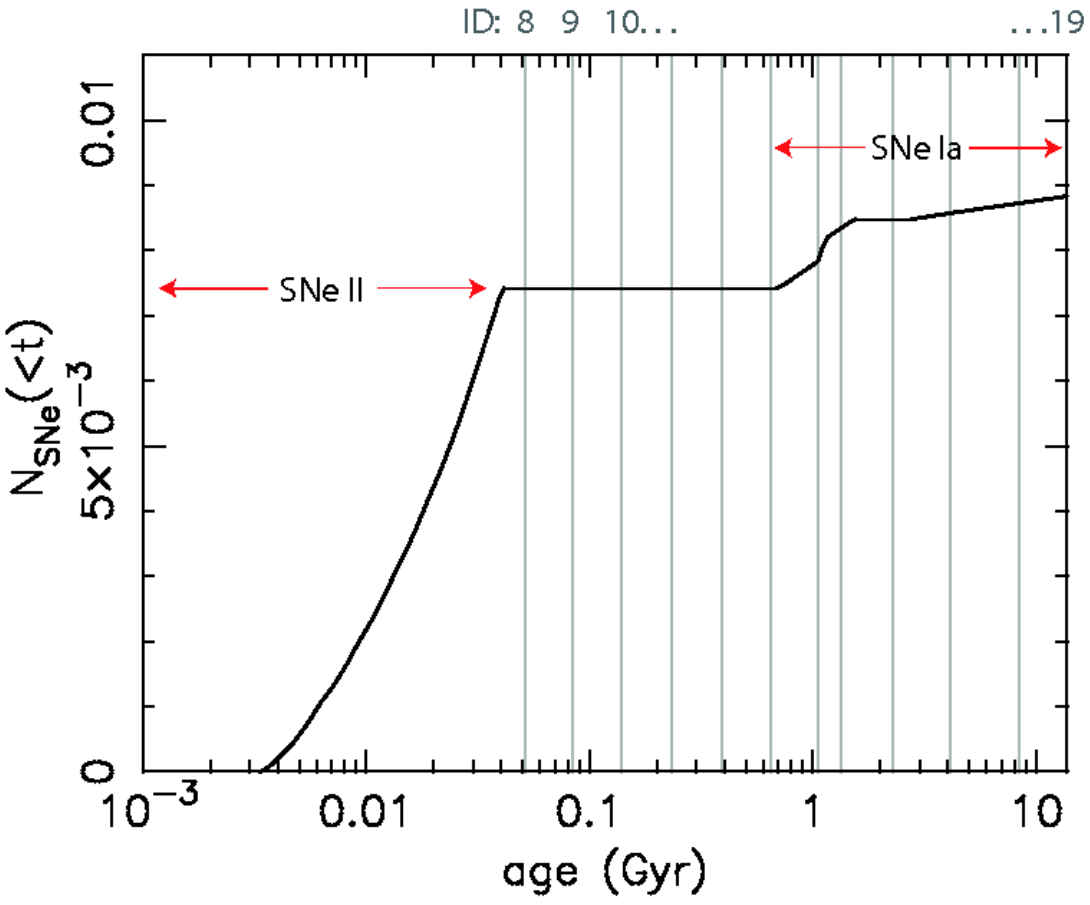

Figure 2.7: The number of supernovae versus age for each ID. The vertical lines show the division of each ID group. The first vertical line (from left) shows the end of ID $1-8$. SNe II stop slightly earlier than the lifetime of ID 1−8, but it is necessary. It means $1-8$ is also taking care of mass loss from stars slightly less than 8 $M_{\odot}$.

becomes a normal gas particle. Due to this algorithm, the particle mass of stars and gas is always constant, and the mass resolution is kept constant.

Chapter 3

Chemodynamical Analysis of Bulge Stars for Simulated Disc Galaxies

3.1 Introduction

In recent years, there has been progress in modelling disc galaxy formation in a Cold Dark Matter (CDM) Universe, using three dimensional numerical simulations (Katz, 1992; Steinmetz & Muller, 1994; Bekki & Chiba, 2000; Abadi et al., 2003a,b; Brook et al., 2004b; Governato et al., 2007; Okamoto et al., 2008). Some studies include both Type II (SNe II) and Type Ia (SNe Ia) supernovae and discuss the details of the chemical properties in the simulated galaxies in an isolated halo collapse (Raiteri et al., 1996; Berczik, 1999) or hierarchical clustering (Brook et al., 2005; Renda et al., 2005a). These studies mainly focus on the disc component of the simulated galaxies. None, except Nakasato & Nomoto (2003), study the bulge formation in three dimensional chemodynamical simulations. Nakasato & Nomoto (2003) suggest that the bulge may be composed of two chemically different components, one being formed through an early epoch subgalactic clump merger, and the other in the

inner region of the disc after this merger. This chapter focuses on the population of bulge stars built up through mergers, using higher resolution and more sophisticated chemodynamics simulations. Especially, we study the properties of accreted and *in situ* stars within the bulge, which Nakasato & Nomoto (2003) do not look at.

There are two major formation scenarios for bulge stars. The first scenario is secular evolution of the disc (see, e.g. Combes et al., 1990; Norman et al., 1996; Noguchi, 1998). In most secular evolution scenarios, gas and stars from the disc are funneled to the central regions of the galaxy. Combes et al. (1990) showed that it is possible to form a bulge via the secular formation of a bar, and Noguchi (1998) showed that the disc of a young galaxy may become gravitationally unstable and fragment into large pieces. These large clumps fall into the central region due to dynamical friction and proceed to form a massive bulge via mergers. Noguchi (1998) and Immeli et al. (2004) also suggest that several peculiar morphological structures seen in the Hubble Deep Field can be explained by a fragmented galactic disc model.

The other major formation scenario for bulge stars is via mergers of subclumps, first shown by Toomre & Toomre (1972). Using numerical simulations and including star formation, gas dynamics and SNe feedback, Katz (1992) showed that hierarchical clustering predicts a number of mergers at high redshift. In these merger processes, the number of bulge stars builds up by accreted stars which were already formed within the infalling galaxies, and by *in situ* stars which form within the main galaxy during and after the merger via starbursts. Although a number of studies focus on accreted stars (Brook et al., 2003; Helmi et al., 2006; Font et al., 2006), there have been few studies comparing the properties of these accreted satellite stars with those of the stars born *in situ* in the galaxy. Recently Zolotov et al. (2009) compared the properties of accreted and *in situ* stars in the halo of the galaxy. There are very few studies however, dedicated to the bulge chemodynamical properties. This is the first study to compare *in situ* and accreted stars within the bulge.

The chemical properties of stars are important to understand the formation history of the bulge. Chemical elements heavier than He are the end products of stellar

evolution. The so-called α-elements and iron (Fe) are of particular interest since it is known that they are produced primarily in SNe II and SNe Ia respectively. SNe Ia and SNe II have different timescales and thus studying the abundance ratios of the α elements with respect to Fe gives unique fossil information on the past conditions and evolution of the galaxy. Pure chemical evolution studies of the bulge such as Matteucci & Brocato (1990); Ferreras et al. (2003) are useful for reconstructing the star formation history of the bulge. Matteucci & Brocato (1990) studied the chemical abundances in the bulge, and looked at the [α/Fe] ratios for different elements. They predicted a relative enhancement of [α/Fe] in the bulge, due to the high Star Formation Rate (SFR). Based on the observed distribution of metallicities and using a simple star formation model, Ferreras et al. (2003) found that very short infall timescales are required in the bulge. These studies are useful to reconstruct the star formation history of the bulge. However, pure chemical evolution models do not answer how such a star formation history occurred in the galaxy, or predict any information about kinematics.

The findings of Matteucci & Brocato (1990) were confirmed by the observational studies of McWilliam & Rich (1994), Fulbright et al. (2006), and Zoccali et al. (2006). By looking through Baade's Window, McWilliam & Rich (1994) found that the primary enrichment process of the bulge was SNe II. Recently, 8m class large telescopes have enabled observers to observe stars in the Milky Way bulge in more detail. Using a larger sample of stars at higher resolution Zoccali et al. (2006) concluded that the Milky Way bulge likely formed through a short series of starbursts triggered by gas rich mergers in the early Universe. In the future, both kinematical and chemical properties of bulge stars will become available via projects such as APOGEE which can look through the obscuring dust to the bulge region of the Milky Way using near infrared multi-object spectrographs (Allende Prieto et al., 2008). ESA's *Gaia* mission should provide six dimensional phase space and chemical information on up to one billion stars in the Milky Way. These stars lie predominantly in the disc however there is some hope that *Gaia* may also

Table 3.1: Simulation parameters

Name	$M_{\rm vir}$ ($M_\odot$)	$r_{\rm vir}$ (kpc)	$m_{\rm gas}$ ($M_\odot$)	$m_{\rm DM}$ ($M_\odot$)	$e_{\rm gas}$ (kpc)	$e_{\rm DM}$ (kpc)	Ω_0	h_0	$\Omega_{\rm b}$
Gal1	8.8×10^{11}	240	9.2×10^5	6.2×10^6	0.57	1.1	0.3	0.7	0.039
Gal2	9.3×10^{11}	270	3.3×10^6	1.9×10^7	0.87	1.5	0.3	0.65	0.045

observe significant numbers of bulge stars (Robin et al., 2005). Ultimately, the *Japan Astrometry Satellite Mission for Infrared Exploration* (*JASMINE*), a planned Japanese space astrometry mission, will observe around ten million stars in the bulge by taking detailed astrometric readings in the infrared band (Gouda et al., 2006). This huge influx of new data is expected to sporn new scientific results in different fields of astronomy. However, to extract the formation history of galaxies from such a large amount of observational data, theoretical models and predictions are crucial. Therefore, we initiate a project to study how we can tell the past formation history of the bulge through the current properties of bulge stars.

We study both chemical and kinematical properties of bulge stars using ΛCDM cosmological simulations. We take two high resolution simulations from the sample of Bailin et al. (2005). In our ΛCDM simulation, bulges formed during hierarchical clustering of building blocks at high redshift. We therefore study the kinds of properties that are expected in bulge stars, if the bulge was formed through such a hierarchical clustering scenario. Therefore, our study does not mean to reproduce the Milky Way bulge which may or may not form through hierarchical clustering.

The outline for this chapter is as follows. In Section 3.2, we describe our numerical simulations and define our bulge stars. In Section 3.3, we present the results of our chemodynamical analyses on accreted and *in situ* stars within the bulge. Finally, we present our conclusions in Section 3.4.

3.2 The Code and Model

To simulate our galaxies, we use our original galactic chemodynamics evolution code GCD+ developed by Kawata & Gibson (2003a). GCD+ is a three-dimensional tree N-body/smoothed particle hydrodynamics (SPH; Lucy, 1977; Gingold & Monaghan, 1977) code (Barnes & Hut, 1986; Hernquist & Katz, 1989; Katz et al., 1996) that incorporates self-gravity, hydrodynamics, radiative cooling, star formation, supernova feedback, and metal enrichment. GCD+ takes into account chemical enrichment by both SNe II (Woosley & Weaver, 1995) and SNe Ia (Iwamoto et al., 1999; Kobayashi et al., 2000) and mass loss from intermediate-mass stars (van den Hoek & Groenewegen, 1997), and follows the chemical enrichment history of both the stellar and gas components of the system.

Radiative cooling, which depends on the metallicity of the gas (derived with MAPPINGSIII: Sutherland & Dopita, 1993) is taken into account. The cooling rate for a gas with solar metallicity is larger than that for gas of primordial composition by more than an order of magnitude. Thus, cooling by metals should not be ignored in numerical simulations of galaxy formation (Källander & Hultman, 1998; Kay et al., 2000). However, we ignore the effect of the UV background radiation for simplicity. Adding a UV background radiation would heat the lower temperature gas ($T < \sim 10^4$ K) and reduce the radiative cooling for the lower density gas. The gas accretion history, especially for lower mass haloes, like sub-clumps, could be affected.

The two galaxies simulated here are from the sample of Bailin et al. (2005), KGCD and AGCD, hereafter 'Gal1' and 'Gal2' respectively. Gal1 is a high resolution version of galaxy 'D1' in Kawata et al. (2004). We used the multi-resolution technique in order to maximise the mass resolution within the regions where the disc progenitors form and evolve (Kawata et al., 2004). The initial conditions for Gal2 were kindly provided by M. Steinmetz, and are described in Abadi et al. (2003a,b).

We summarise the properties of the galaxies in Table 3.1 taken from Connors

et al. (2006). The first column represents the galaxy name; the second column, the virial mass; Column 3, the virial radius; Columns 4 and 5 represent the mass of each gas and dark matter particle in the highest resolution region, and Columns 6 and 7 are the softening lengths in that region. The cosmological parameters for the simulation are presented in Columns 8–10. Ω_0 is the total matter density fraction, h_0 is the Hubble constant (100 $\mathrm{kms}^{-1}\mathrm{Mpc}^{-1}$) and Ω_b is the baryon density fraction in the universe. Note that the cosmology is slightly different between the two models, and the age of the Universe is 13.5 and 14.5 Gyr for Gal1 and Gal2 models, respectively. We employ $\sigma_8 = 0.9$ for both simulations.

To identify the main progenitor galaxy, at each output of the simulation, a friend-of-friend (FOF) group finder is used to identify stellar groups. Specifying a linking length b and identifying all pairs of particles with a separation equal to or less than b times the mean particle separation as friends, stellar groups are defined as sets of particles connected by one or more friendship relations. The other main parameter in FOF is the minimum number of particles. By setting this parameter sufficiently high, one avoids including spurious objects that may arise due to chance. In our simulations we use a linking parameter $b = 0.01$ and a threshold number of particles of 100. We define the largest group which has the highest number of the FOF identified particles as the main progenitor galaxy.

Note that the version of `GCD+` used in this chapter (Kawata & Gibson, 2003a) applies the SNe II yields calculated by Woosley & Weaver (1995). It is well known that this yield seems to be overestimated and leads to lower [α/Fe], compared with that observed in low-metallicity stars in the solar neighbourhood (Timmes et al., 1995; Gibson, 1997; Gibson et al., 1997). We adopted pure Woosley & Weaver yields for Gal1. On the other hand, we apply a half Fe yield for Gal2. As a result, [Mg/Fe] values in Gal1 are underestimated compared to Gal2. Therefore, we cannot compare the absolute value of [Mg/Fe] between Gal1 and Gal2. However, we compare the relative difference of [Mg/Fe] among different samples of stars within a simulated galaxy. Our code does not 'disperse' metals between gas particles. Therefore, the

spread in the metallicity distributions will be artificially high, while the peak of the distributions (the average) should be robust (or at least the distances between the peaks).

We identify bulge particles using the simulation output at the latest time. For Gal1, we use the output at $z = 0.1$, as going to any lower redshift results in an unacceptable amount of contamination from low-resolution particles in our simulated galaxy. For Gal2, we use the output at $z = 0$. To define the bulge, we first set the disc plane of our galaxies to be the $x - y$ plane and the rotation axis to be the z-axis. The bulge was defined as the central 2 kpc of the galaxy, excluding ± 1 kpc in the z-direction due to contamination with disc stars. Avoiding the disc plane will provide us with a 'cleaner' sample since the central region of the disc suffers from 'overcooling' problems and therefore produces too many stars throughout the simulations. All stars found within the remaining volume described above we refer to as 'bulge stars', and we analyse their properties in the next section.

In our cosmological simulations, gas particles cool too quickly at early times and sink towards the centre of their haloes which become dense and concentrated. This leads to a rapid increase in the star formation rate at early times, which uses up most of the gas. This is known as the overcooling problem. When these haloes with a centrally concentrated baryon component merge, the angular momentum of the baryons is transferred to the dark matter component. This results in a large bulge component and a small disc component which become more spheroidal, resembling an early-type spiral galaxy. This problem is often called the angular momentum catastrophe. Since the gas is used up too quickly at early epochs due to the overcooling problem, there is not much gas left to accrete at later epochs when the disc can grow, due to less merger activity. This also prevents the growth of the disc at later epochs.

3.3 Results

Fig. 3.1 shows [Fe/H] (upper panel) and [Mg/Fe] (lower panel) as a function of the time (t_f) when bulge stars in our two galaxies formed. There is clearly a different formation history for the bulges of the two galaxies. The bulge of Gal1 forms via a series of three mergers within the first 5 Gyr. The bulge of Gal2 is formed in a similar timescale, however without the distinctly separated star formation epochs. Star formation here is more smooth and continuous. Both galaxies formed through hierarchical clustering, and bulge formation is associated with a series of mergers at early epochs. However, Gal1 and Gal2 have different merger histories and therefore star formation histories. The aim of this study is to find out how we can tell such a difference in merger histories at a high redshift from the current properties of bulge stars. To this end, first we separate the bulge stars into accreted stars and *in situ* stars, and compare their properties in Section 3.3.1. From the current chemical and kinematical properties of bulge stars, we study how we can distinguish accreted stars from *in situ* stars. In Section 3.3.2, we compare the properties of the bulge stars with different formation epochs to see whether the memory of mergers at different epochs persists or not.

3.3.1 Accreted and *In situ* Stars

In this section, we compare the chemical and kinematical properties of accreted and locally formed stars. We trace back the formation time and location for all the bulge stars, and any stars that are born within a radius of 5 kpc from the largest progenitor are given the title '*in situ* stars'. Stars that form at a radius greater than 5 kpc from the centre of the galaxy and end up within the area defined above as the bulge, we term 'accreted stars'. We chose 5 kpc arbitrarily. We experimented using a larger radius up to 20 kpc, and generally found the same conclusion.

Fig. 3.1 shows [Fe/H] and [Mg/Fe] vs formation time for accreted and *in situ* stars with different symbols. Mg is one of the so-called α-elements. These elements

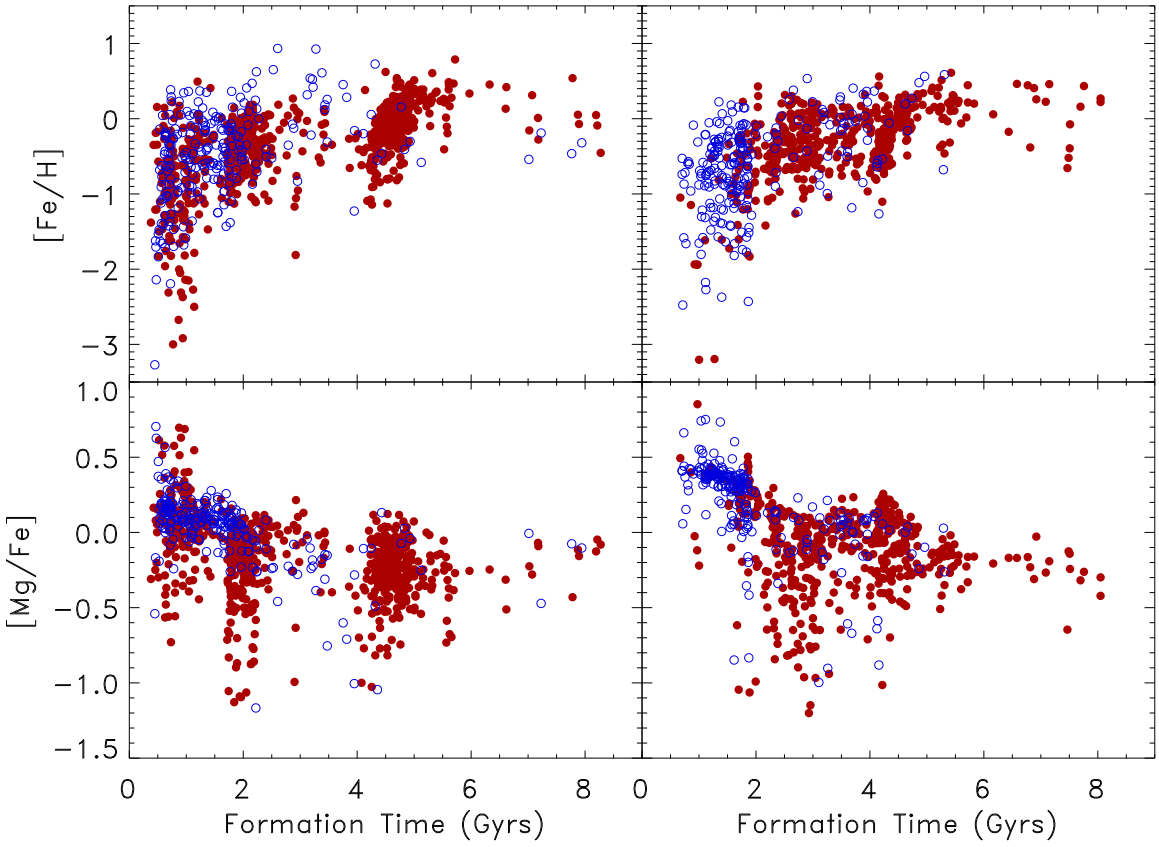

Figure 3.1: [Fe/H] (upper) and [Mg/Fe] (lower) against formation time (t_f) for Gal1 (left) and Gal2 (right). Red filled and blue open circles are *in situ* and accreted stars, respectively. There are 3 major periods of star formation clearly distinguishable in Gal1. Star formation is smoother in Gal2.

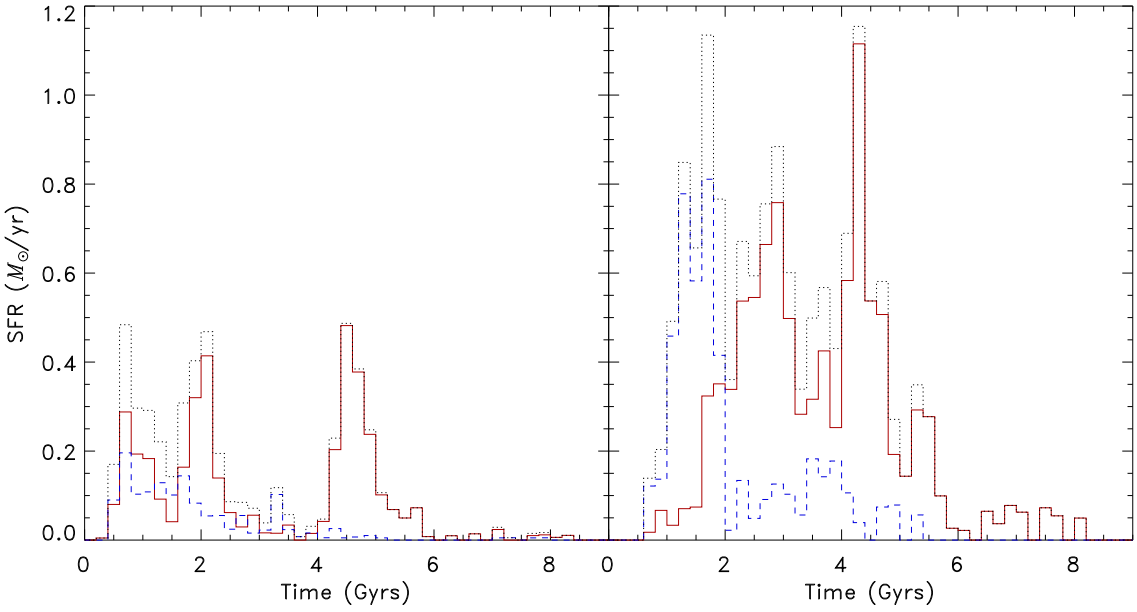

Figure 3.2: Global SFR for Gal1 (left) and Gal2 (right). Red solid, blue dashed and black dotted are *in situ*, accreted and total stars, respectively.

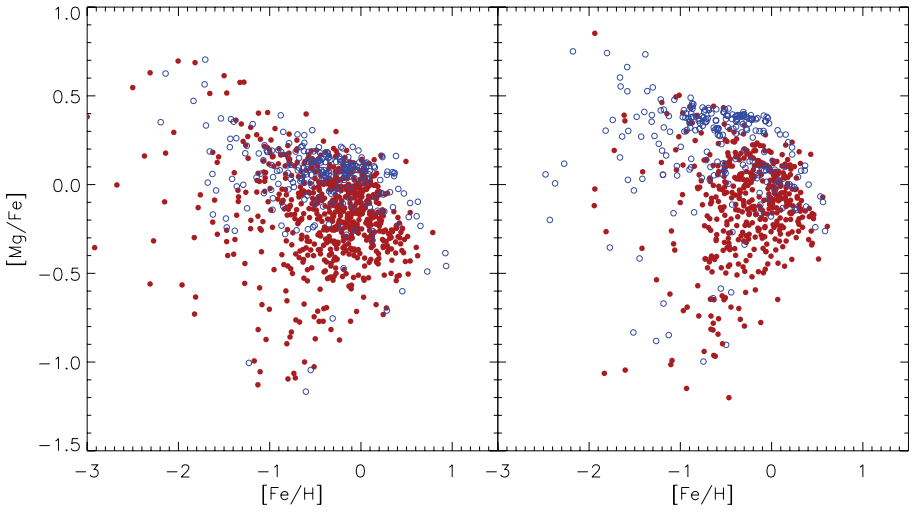

Figure 3.3: [Mg/Fe] vs [Fe/H] for Gal1 (left) and Gal2 (right). Red filled and blue open circles are *in situ* and accreted stars respectively. As expected from Fig. 3.1, accreted stars have generally higher [Mg/Fe] ratios. A population of accreted stars in Gal2 have high [Mg/Fe] because these stars formed in a large satellite which merged into the main galaxy at an early epoch.

are primarily produced when massive stars with short lifetimes explode as SNe II. Fe is produced predominantly in SNe Ia, from lower mass binary stars with longer lifetimes. Accreted stars have lower [Fe/H] and higher [α/Fe] since they form in early epochs before the enrichment from SNe Ia becomes important. *in situ* stars continue to undergo strong star formation for up to 5 Gyr (as seen in Fig. 3.2, which shows the SFR history for *in situ* and accreted stars). Fig. 3.3 shows [Mg/Fe] vs [Fe/H]. Note that there exists a distinct population of accreted stars in Gal2 with high [α/Fe]. This is because these accreted stars were formed in a large companion galaxy at early epochs ($t < 1.5$ Gyr) that underwent a major merger with the main galaxy (Fig. 3.2). This demonstrates that the probability distribution of high [Mg/Fe] stars may be sensitive to merger history at high redshift.

We find that Fig. 3.4 is the most useful for identifying the accreted stars. It shows the stars total energy ($E_{\rm tot}$) plotted against their z-component of angular momentum (L_z) which is also used to identify accreted stellar groups in halo stars (Helmi & de Zeeuw, 2000; Knebe et al., 2005; Font et al., 2006). The accreted stars have a relatively higher $E_{\rm tot}$ and are spread to a large range of L_z. This is especially the case for Gal1. For Gal2 however, the distinction is less clear. There exists a significant population of accreted stars with low $E_{\rm tot}$ in Gal2. This is due to the major merger this galaxy experienced at an early epoch in its history. These accreted stars with low $E_{\rm tot}$ were actually formed in the centre of a large satellite galaxy that merged with the main galaxy early on which explains why their $E_{\rm tot}$ is comparable to the *in situ* stars.

We conclude that the $E_{\rm tot} - L_z$ diagram is a powerful tool to identify accreted stars in the bulge. Its use is known for halo stars (Brook et al 2003, Morrison et al 2009). Our study shows that it can be applied for bulge stars which experienced more violent merger histories. However, there are significant overlaps with *in situ* stars. Especially, it is difficult to identify stars which are born in a large satellite galaxy that merged at an early epoch.

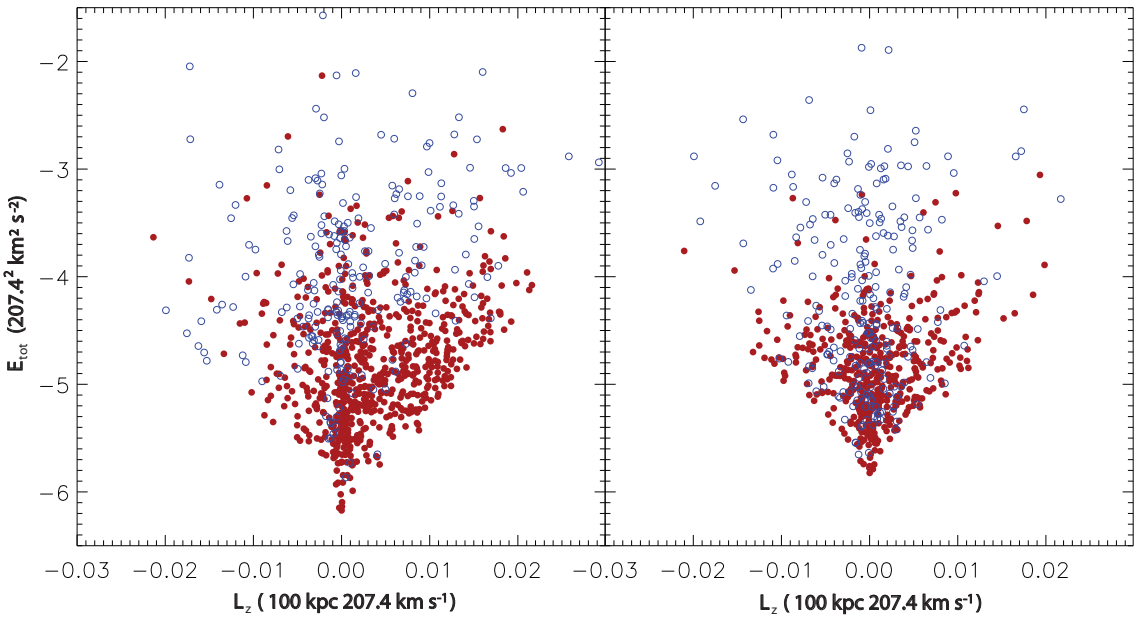

Figure 3.4: Total energy ($E_{\rm tot}$) vs angular momentum (L_z) for Gal1 (left) and Gal2 (right) for accreted (open blue circles) and *in situ* (filled red circles) stars. Accreted stars have higher $E_{\rm tot}$. For Gal2, the distinction is unclear. This is due to a major merger early in its history bringing stars of a satellite galaxy into the main galaxy as accreted stars. Note the axes are plotted in GCD+ simulation units, where the unit for length is 100 kpc, and the unit for velocity is 207.4 kms^{-1}.

3.3.2 Multiple Merger Bulge Formation

The left panel of Fig. 3.2 clearly shows that Gal1 has 3 bursts of star formation. From snapshots, we confirmed that each of the bursts corresponds to a merger. We therefore divided the bulge stars into 3 samples corresponding to each of the bursts. The stars formed during the period of the first burst ($t_f < 1.5$ Gyr) are referred to as 'old' bulge stars; those formed during the second burst ($1.5 < t_f < 3$ Gyr) are called 'intermediate' bulge stars; and those formed during and after the third and largest burst ($t_f > 3$ Gyr) are called 'young' bulge stars. From the right panel of Fig. 3.2 we see that Gal2 also has three bursts of star formation, although there is significant star formation between the bursts. Therefore, we also assign 3 periods of star formation for Gal2. Our definition for the 3 time periods here was slightly different to Gal1, reflecting the different star formation history in Gal2. The formation periods of old, intermediate and young stars for Gal2 are defined as t_f

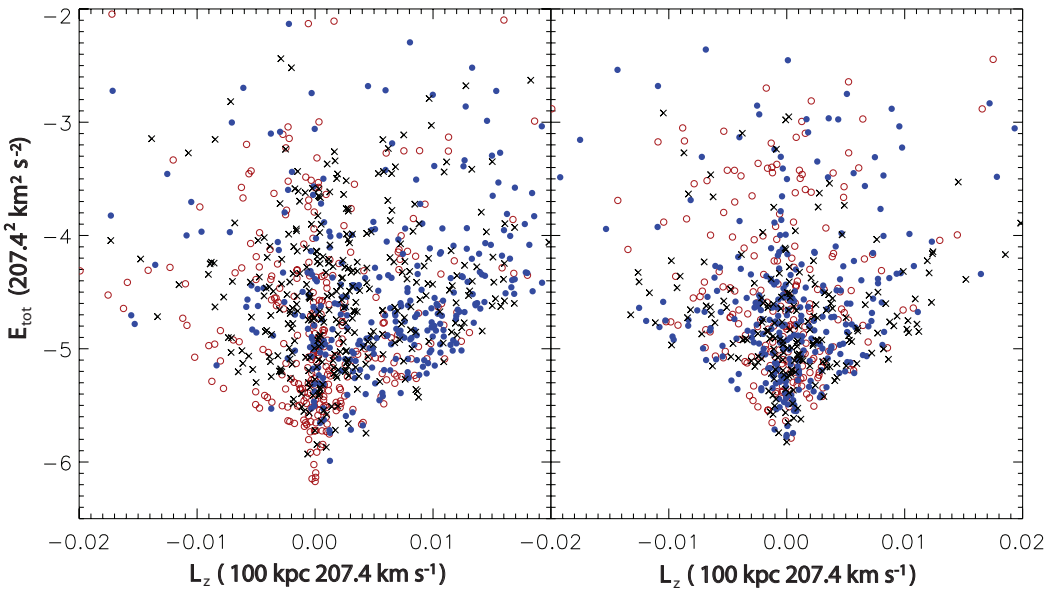

Figure 3.5: As in Fig. 3.4, but now using different aged bulge stars for Gal1 (left) and Gal2 (right). Red open circles, blue filled circles and black crosses are old, intermediate and young bulge stars, respectively. Trends are visible, especially in Gal1 which contains an intermediate aged population with a distinctly high L_z, possibly indicating the prograde orbit of a merger at that epoch.

< 2 Gyr, $2 < t_f < 4$ Gyr, and $t_f > 4$ Gyr respectively.

In Fig. 3.5, we replot $E_{\rm tot}$ vs L_z for the three different groups of bulge stars. In Gal1 (left panel), the old stars are generally clustered about the centre with low $|L_z|$ and $E_{\rm tot}$. Young stars have higher $E_{\rm tot}$ and are less clustered about low values of $|L_z|$. In Gal1, we clearly see that the majority of intermediate stars have high L_z. This indicated that the intermediate population may have resulted from a specific merger and are orbiting in a prograde direction. This demonstrates that some information from the ancient history of mergers can persist in $E_{\rm tot}$ and L_z properties. If then, in addition, the ages of the stars are measured very accurately, the diagram of $E_{\rm tot}$ and L_z may become a powerful tool to reconstruct the merger history. The picture for Gal2, again, is less clear. The three populations in Gal2 are well spread on the diagram. No group occupies a distinct region.

Fig. 3.6 shows that the old stars have the highest [Mg/Fe]. The younger stars

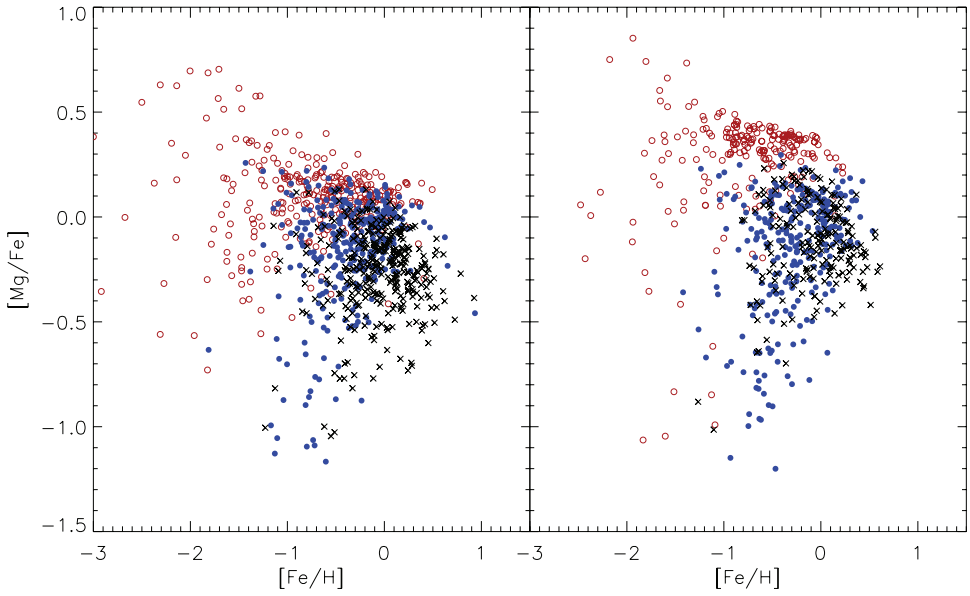

Figure 3.6: As in Fig. 3.3, but now using different aged bulge stars. Red open circles, blue filled circles and black crosses are old, intermediate and young bulge stars, respectively. For Gal1 again, the distinction between the different groups is clearer.

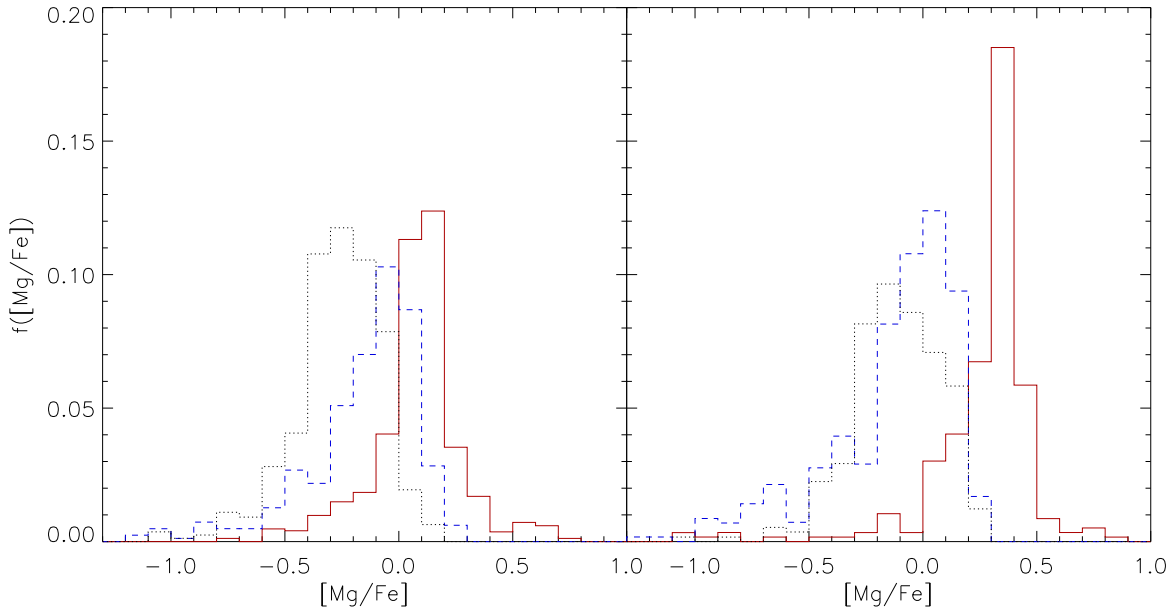

Figure 3.7: Histogram of [Mg/Fe] for different age samples of bulge stars for Gal1 (left) and Gal2 (right). Red solid, blue dashed and black dotted are old, intermediate and young bulge stars, respectively.

have lower [Mg/Fe] and a higher metallicity as expected. This is because at later times the contribution from SNe Ia has become significant. The pattern is less clear for Gal2, reflecting its more continuous formation history, which diffuses out any trends. We plot the 3 samples of bulge stars as a probability distribution function for [Mg/Fe] in Fig. 3.7. We see that they each occupy a separate distinct region, although there is some overlap. As mentioned in Section 3.2, our simulations do not take into account metal mixing between the gas particles. We overestimate the scatter of metal abundance and abundance ratios for star particles. Therefore, if the correct metal mixing is taken into account, [Mg/Fe] distributions of these 3 groups of stars will be more clearly different. Note, however, that here we have assumed that we have accurate age information available for bulge stars. However, in reality, with the current facilities, it is difficult to obtain the ages of the bulge stars. Our study demonstrates that if the accurate age information becomes available (as it will in the future), we can identify bulges formed through distinct multiple mergers using the age−[Mg/Fe] relation (Fig. 3.1). Then, for bulge stars that are formed as a result of mergers at different epochs, we would expect differing values for [Mg/Fe], and for younger stars to have lower [Mg/Fe]. In addition, the $E_{\rm tot} - L_z$ diagram can give us some information on the orbit of merging building blocks.

3.4 Summary

In this study we have analysed the chemistry and the dynamics of the bulge stars of two simulated disc galaxies. The two galaxies had different formation histories and were simulated under different cosmologies. However, both galaxies were similar in mass and size to the Milky Way, and contained distinct gas and stellar disc components (Bailin et al., 2005; Connors et al., 2006).

We started by defining the bulge region to be the central 2 kpc of the galaxy excluding ± 1 kpc in the z-direction to avoid contamination with disc stars. In this study we compared the properties of accreted and *in situ* stars within the bulge.

Since accreted stars tend to form in early epochs, they have lower [Fe/H] and higher [Mg/Fe] ratios. We also found that even within the bulge, the accreted stars tend to have higher $E_{\rm tot}$ although there is significant overlap with *in situ* stars. We found that accreted stars formed in a large satellite galaxy that merged into the main galaxy can have low $E_{\rm tot}$ and are difficult to distinguish from *in situ* stars.

The bulge of one of the simulated galaxies was formed via a series of three distinct mergers in the first 5 Gyr as confirmed by snapshots of the simulations. We found that such multiple star formation bursts will show up in the age−metallicity relation or more evidently in the age−[Mg/Fe] relation, provided there is accurate age information available. Then, stars that formed in earlier mergers tend to have higher [Mg/Fe], and different mergers have distinctively different [Mg/Fe]. Therefore, the probability distribution of [Mg/Fe] is sensitive to the number of mergers and the epochs of the mergers. We found that even in the bulge $E_{\rm tot}$ and L_z information persists reasonably well until $z = 0$. Therefore, if we could pick up stars formed in a merger at a specific epoch using the age information, $E_{\rm tot}$ and L_z would be able to tell us about the orbital information of the merger, like whether it was in a prograde or retrograde direction.

The other simulated galaxy had underwent a major merger at a very early epoch, followed by a series of minor mergers between two later major mergers, which led to a smoother star formation history. This meant that much of the chemodynamical information had been smeared out. We found that a significant number of accreted bulge stars had high values of [Mg/Fe], due to significant star formation in two large progenitors at early epochs. This sensitivity to the star formation rate at early epochs means that finding such bulge stars with high values for [Mg/Fe] could depend on the size of the progenitors at the very early epochs.

Despite differences, our two simulated galaxies share some common formation features. There is evidence for the bulge of both galaxies forming via three major bursts of star formation. This is because in hierarchical clustering scenarios, bulges are likely to form through multiple rather than single mergers. If then, such merger

epochs are separated by enough time, we may obtain information on these mergers from the properties observed in our simulated galaxies at $z = 0$.

It is not yet possible from the current observations to obtain accurate age information for bulge stars. However, in the near future, when increasingly accurate age information becomes available from combinations of the near-infrared astrometry satellite *JASMINE*, and high resolution spectroscopy in the optical (Fulbright et al., 2006) and near-infrared with APOGEE, (see Allende Prieto et al., 2008) our findings will prove useful for identifying a possible scenario for the past formation history of the Galactic bulge.

Chapter 4

Metallicity Gradients of Disc Stars for a Cosmologically Simulated Galaxy

4.1 Introduction

In recent years, there have been extensive efforts devoted to measuring chemical abundance trends within the Galactic disc (Friel et al., 2002; Chen et al., 2003; Daflon & Cunha, 2004; Esteban et al., 2005; Yong et al., 2005; Sestito et al., 2008; Maciel & Costa, 2009; Pancino et al., 2010; Bensby et al., 2010) using various tracers. The aim of these studies has been to find out how our Galactic disc formed and evolved with time. Around the solar neighborhood, good progress has been made recently, including the derivation of age information for several clusters (e.g. Pancino et al., 2010) and individual stars (e.g. Nordström et al., 2004; Pont & Eyer, 2004; Jorgensen & Lindegren, 2005; Holmberg et al., 2007, 2009). However, further out, at larger galactocentric radii, there is a striking lack of any large high quality datasets. To unravel the formation history of the Galactic disc, we need to know the abundance trends in the stars along the disc complemented with accurate age information.

In the near future ESA's *Gaia* mission should provide exceptional positional and proper motion information for up to one billion stars in the Milky Way. The vast majority (80%) of these stars will lie in the disc. For bright stars, the *Gaia* RVS will determine the abundances of iron and the α-elements. In addition, future and proposed ground-based projects including the Apache Point Observatory Galactic Evolution Experiment (APOGEE; Allende Prieto et al., 2008) and the High Efficiency and Resolution Multi-Element Spectrograph (HERMES) survey (Freeman & Bland-Hawthorn, 2008) will provide more detailed and accurate chemical abundance determinations which will complement the *Gaia* data.

The chemical properties of stars are important to understand the formation history of the disc. Chemical elements heavier than boron are the end products of stellar evolution. The so-called α-elements and iron (Fe) are of particular interest since it is known that they are produced primarily in Type II supernovae (SNe II) and Type Ia supernovae (SNe Ia), respectively. SNe Ia and SNe II have different time-scales and thus studying the abundance ratios of the α-elements with respect to Fe gives unique fossil information on the past conditions and evolution of the galaxy. In addition to studying various [α/Fe] ratios, we also look at how the ratio of [N/O] varies with galactocentric radius as this can also be used as a cosmic clock. Good cosmic clocks are obtained by taking the ratios of elements produced by different stellar masses and therefore on different time-scales. Nitrogen is primarily produced by intermediate-mass stars with longer lifetimes whereas oxygen is produced by SNe II progenitor stars which have a shorter lifetime. In any case, the actual abundance gradients and ratios of different elements will vary depending on the chemical evolution histories at different radii and therefore on the building-up history of the disc.

The chemical evolution at different radii of the disc is studied theoretically using pure chemical evolution models (e.g. Chiappini et al., 1997, 2001; Renda et al., 2005b). Chiappini et al. (1997) suggested that the Milky Way forms primarily out of two infall episodes: the first giving rise to the halo and subsequently the

bulge, and the second producing the disc via a much slower infall of primordial gas preferentially accumulating faster in the inner compared to the outer regions of the disc. This scenario is known as the 'inside-out' mechanism for disc formation. It is one of the possible mechanisms which can reproduce and explain the observed properties of the Milky Way. However, in order to be able to draw firmer conclusions, it is necessary to have observational data for the outer regions of the Galactic disc (Chiappini et al., 2001).

Inside-out formation may lead to some specific evolution of the abundance gradients. How do the abundance gradients evolve within the disc? There is still a lack of agreement between different authors; for some the gradients steepen with time (Chiappini et al., 1997), whilst to others the gradients flatten with time (Hou et al., 2000; Daflon & Cunha, 2004; Maciel & Costa, 2009). Note, however, that some authors have recently suggested that the traditional chemical evolution models such as those of Chiappini et al. (2001) may need to be revised as they do not sufficiently consider the important effects of radial mixing (Schönrich & Binney, 2009b).

In recent years, there has been progress in modelling disc galaxy formation in a Cold Dark Matter (CDM) Universe, using three dimensional numerical simulations (Katz, 1992; Steinmetz & Muller, 1994; Bekki & Chiba, 2000; Abadi et al., 2003a,b; Brook et al., 2004b; Governato et al., 2007; Okamoto et al., 2008; Scannapieco et al., 2008, 2009). Some studies include both SNe II and SNe Ia and discuss the details of the chemical properties in the simulated galaxies in an isolated halo collapse (Raiteri et al., 1996; Berczik, 1999) or hierarchical clustering (Brook et al., 2005; Renda et al., 2005a; Scannapieco et al., 2005; Martínez-Serrano et al., 2008) scenario. However, to date, no three-dimensional fully cosmological chemodynamical simulations have looked at radial abundance trends with age of disc stars. This is the first study to do so and it will be very interesting to see how our results will compare with the literature, both with theory and observations.

In this chapter, we analyse the chemodynamical properties of the disc stars in a Milky Way size disc galaxy in our ΛCDM cosmological simulation. Unfortunately,

Table 4.1: Simulation parameters

Name	$M_{\rm vir}$ ($M_\odot$)	$r_{\rm vir}$ (kpc)	$m_{\rm gas}$ [a] ($M_\odot$)	$m_{\rm DM}$ [b] ($M_\odot$)	$e_{\rm gas}$ (kpc)	$e_{\rm DM}$ (kpc)	Ω_0	h_0	$\Omega_{\rm b}$
Gal1	8.8×10^{11}	240	9.2×10^5	6.2×10^6	0.57	1.1	0.3	0.7	0.039

[a]Mass of gas per particle
[b]Mass of dark matter per particle

the simulated galaxy is not a late-type disc galaxy, such as the Milky Way, but closer to an early-type Sa galaxy. Nevertheless, since the detailed chemical distribution of disc stars is only available to us in the Milky Way, we compare our simulation with the Galaxy, and discuss what we could learn about the formation and evolution of a general disc component.

The outline for this chapter is as follows. In Section 4.2 we describe our numerical simulation and define our disc stars. In Section 4.3 we present the results of our chemodynamical analyses. We initially study the properties and differences between accreted and *in situ* stars within the disc in Section 4.3.1. In Section 4.3.2 we analyse any radial abundance trends in the disc and their relation to the age of the disc stars with the aim of unravelling the formation mechanisms of our disc. Finally we present our conclusions in Section 4.4.

4.2 The Code and Model

To simulate our galaxy, we use the original galactic chemodynamical evolution code `GCD+` developed by Kawata & Gibson (2003a) and described in Chapters 2 and 3.2. `GCD+` takes into account the metallicity dependence of the age of stars (Kodama & Arimoto, 1997), the metal dependent yields from SNe II and mass loss from intermediate mass stars. Radiative cooling, which depends on the metallicity of the gas, is taken into account. However, we ignore the heating effect of the cosmic UV background radiation and UV radiation from hot stars for simplicity.

Star formation is modelled using a method similar to that suggested by Katz

(1992) and Katz et al. (1996). For star formation to occur, the following three criteria must be satisfied: (i) the gas density is greater than some critical density; (ii) the gas velocity field is convergent and (iii) the Jeans instability condition is satisfied. Our star formation rate (SFR) formula corresponds to the Schmidt law. We assume that stars are distributed according to the Salpeter (1955) initial mass function (IMF). For more details see Kawata & Gibson (2003a). Note that we assume only thermal energy feedback from SNe. It is known that the thermal energy feedback model has a negligible effect on galaxy formation (e.g. Katz, 1992; Brook et al., 2004a). In real galaxies, the effects of SNe feedback are likely stronger, and could affect the chemical evolution in the disc component, as discussed in Scannapieco et al. (2008). However, there is still no model that can convincingly explain how SNe feedback affects galaxy formation and evolution. In this chapter rather than exploring a variety of feedback modelling, we have implemented one simple feedback model and study how chemical evolution takes place under this assumption. Our simulation, therefore, does not include any outflow, such as a Galactic fountain (Bregman, 1980). Although some authors (e.g. Recchi et al., 2001) suggest that SNe Ia dump more energy to the surrounding interstellar medium (ISM) than SNe II, we assume the same energy per SN for SNe II and SNe Ia for simplicity.

The galaxy simulated here is from the sample of Rahimi et al. (2010), referred to as 'Gal1'. Gal1 is a high-resolution version of galaxy 'D1' in Kawata et al. (2004). Rahimi et al. (2010) analyse a second galaxy ('Gal2'), but Gal2 has a lower resolution and a less prominent disc, and thus we focus only on Gal1 in this chapter. We used the multi-resolution technique in order to maximise the mass resolution within the regions where the disc progenitors form and evolve (Kawata et al., 2004). Here, only the high-resolution region includes the gas particles, and therefore star formation.

We summarise the properties of our simulated galaxy in Table 4.1 adapted from Rahimi et al. (2010). The second column represents the virial mass; the third column represents the virial radius; fourth and fifth columns represent the mass of each gas and dark matter particle in the highest resolution region and sixth and seventh

columns are the softening lengths in that region. The cosmological parameters for the simulation are presented in Columns 8−10. Ω_0 is the total matter density fraction, h_0 is the Hubble constant (100 $\mathrm{kms}^{-1}\mathrm{Mpc}^{-1}$) and Ω_b is the baryon density fraction in the universe. The age of the universe is 13.5 Gyr in our simulation.

To identify the main progenitor galaxy, a friends-of-friends (FOF) group finder is used at regular time intervals in the simulation. Specifying a linking length b and identifying all pairs of particles with a separation equal to or less than b times the mean particle separation as friends, stellar groups are defined as sets of particles connected by one or more friendship relations. The other main parameter in the FOF algorithm is the minimum number of particles. By setting this parameter sufficiently high, one avoids including spurious objects that may arise by chance. In our simulations we use a linking parameter $b = 0.01$ and a threshold number of particles of 100. We define the largest group which has the highest number of the FOF identified particles as the main progenitor galaxy.

Note that the version of `GCD+` used in this chapter (Kawata & Gibson, 2003a) applies the SNe II yields calculated by Woosley & Weaver (1995). The iron yield is ambiguous for the SNe II nucleosynthesis model, as there is a large uncertainty in its value. It is well known that the iron yield shown in Woosley & Weaver (1995) seems to lead to lower [α/Fe] values, compared to those observed in low-metallicity stars in the solar neighborhood. Therefore, some authors commonly use half of the Woosley & Weaver (1995) iron yield (e.g. Timmes et al., 1995; Gibson, 1997; Gibson et al., 1997). The version of GCD+ used in this chapter applies the actual value of the iron yield in Woosley & Weaver (1995). We, however, allow for this by only comparing the relative difference of [α/Fe] among different samples of stars within our simulated galaxy. Also note that although we disperse metals to neighbour gas particles when a star dies, weighted by a kernel, metal diffusion between gas particles was not considered in this simulation. Therefore, the spread in the metallicity distributions will be artificially high, while the peak of the distributions should be robust. Since we likely overestimate the scatter in our results, we take the median

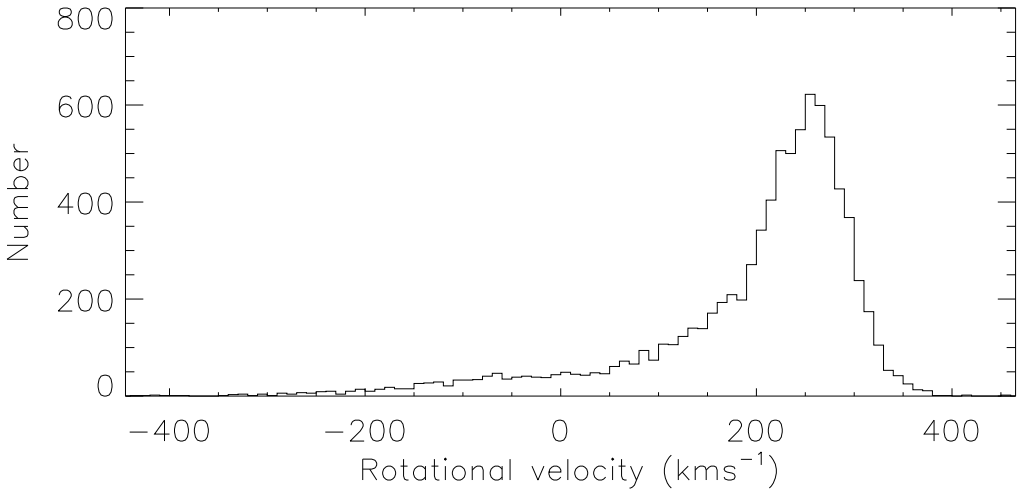

Figure 4.1: Histogram showing the rotational velocities of stars in our disc region. We defined disc stars to have rotational velocity between 150 and 350 kms^{-1}. The circular rotation speed in the central regions of our disc, at a radius of 7 kpc, was 260 kms^{-1}.

value for approximately every 100 stellar particles in each [Fe/H], [O/Fe] or radius bin in Section 4.3.1 and Section 4.3.2 respectively and plot it as a single point. This method reveals more clearly any trends present in the data.

We identify disc particles using the simulation output at the end of the simulation. We use the output at $z = 0.1$ (t $\sim$ 12.3 Gyr), as going to any lower redshift results in an unacceptable amount of contamination from low-resolution particles in our simulated galaxy. To define the disc, we first set the disc plane of our galaxy to be along the gas axis (x−y plane) and the rotation axis to be the z-axis. The disc was defined as extending radially between 4 and 10 kpc in the galactic plane and $\pm$1 kpc in the z-direction. We did not include in our sample any stars found at less than 4 kpc from the centre of the galaxy to minimise possible contamination with bulge stars. Furthermore, only stars with a rotational velocity between 150-350 kms^{-1} were included in our disc sample. This velocity range was a somewhat arbitrary choice. These combined criteria, however, worked well to isolate disc stars. In Fig. 4.1, we show the histogram of rotation velocity for the stars in our

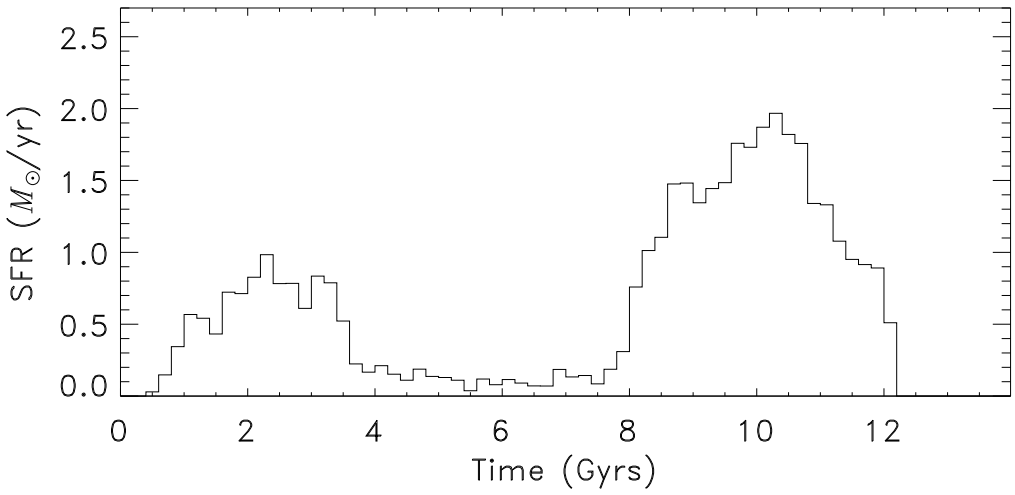

Figure 4.2: SFR history of disc stars . Two periods of star formation are visible.

disc region. Fig. 4.1 shows that the rotation component is clear and dominant in the disc region. Nevertheless, our sample does include some bulge stars, because the simulated galaxy has a large fraction of bulge stars. However, the rotation velocity criterion restricts the contamination only to the population of bulge stars which have a significant rotation velocity. Also note that in our simulated galaxy the bulge stars formed only at early epochs (Rahimi et al., 2010), so there should not be any contamination for the younger stars that are the focus of this chapter.

4.3 Results

Fig. 4.2 shows the total SFR as a function of time for our sample of disc stars. Note that Fig. 4.2 does not include particles which were born in the disc region, but at this particular time are not in the disc. We expect that a significant amount of stars, especially old stars, are kinematically heated up after they formed in the disc, due to our poor resolution. Therefore, we likely underestimate the population of disc stars, and our results focus on the population of relatively cold disc stars at the final timestep. From Fig. 4.2 we see that our simulated galaxy had two episodes of star

formation, the first occurring at an early epoch centred around 2 Gyr and ending before 4 Gyr. The other main episode of star formation occurred at much later times and was more intense and lasted longer. The major episode of star formation responsible for making the disc started after 7 Gyr and lasted till the final timestep. Note that our simulated galaxy stops at $z = 0.1$. Also note that the overall star formation history is not like that inferred from solar neighbourhood stars in the Milky Way, although there is no consensus as to what that is exactly (e.g. Bertelli & Nasi, 2001; Rocha-Pinto et al., 2004; Aumer & Binney, 2009). This also shows that our simulated galaxy is different from the Milky Way. We bear this in mind in the following discussion.

Our simulated galaxy formed through hierarchical clustering, and early disc formation is associated with a series of mergers at early epochs when bulges are also built up (Rahimi et al., 2010). One of the aims of this study is to show how we can infer such a merger history and building up history of the disc from the present-time properties of disc stars. To this end, first we separate the disc stars into accreted stars and stars formed *in situ*. From the current chemical and kinematical properties of disc stars, we study how chemical and kinematical properties differ between accreted and *in situ* stars in Section 4.3.1. In Section 4.3.2 we split our *in situ* disc stars into two samples based on the age of the stars. We then compare the properties of our two groups of disc stars at different galactocentric radii to see if we can find any metallicity gradients with galactocentric radius and how they relate to the formation history of the discs. Finally, in Section 4.4, we summarise our findings.

4.3.1 Accreted and *In situ* Stars

In this section, we compare the chemical and kinematical properties of accreted and *in situ* stars. We trace back the formation time and location for all the disc stars, and any stars that are born within a radius of 20 kpc from the largest progenitor and end up within the area defined as the disc at the final timestep are given the title '*in*

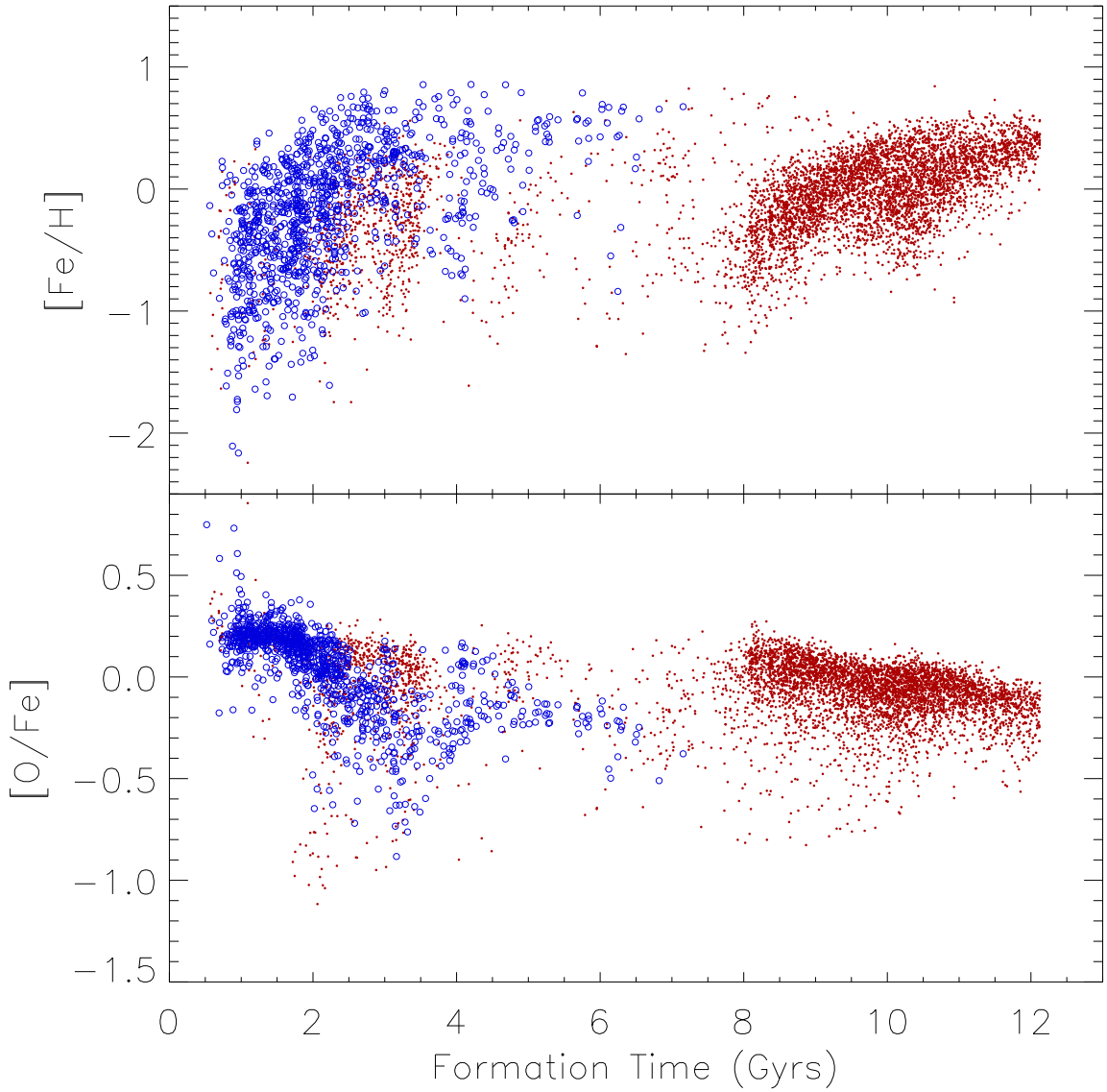

Figure 4.3: [Fe/H] (upper) and [O/Fe] (lower) against formation time (t_f) for our disc stars. Red filled and blue open circles are *in situ* and accreted disc stars respectively.

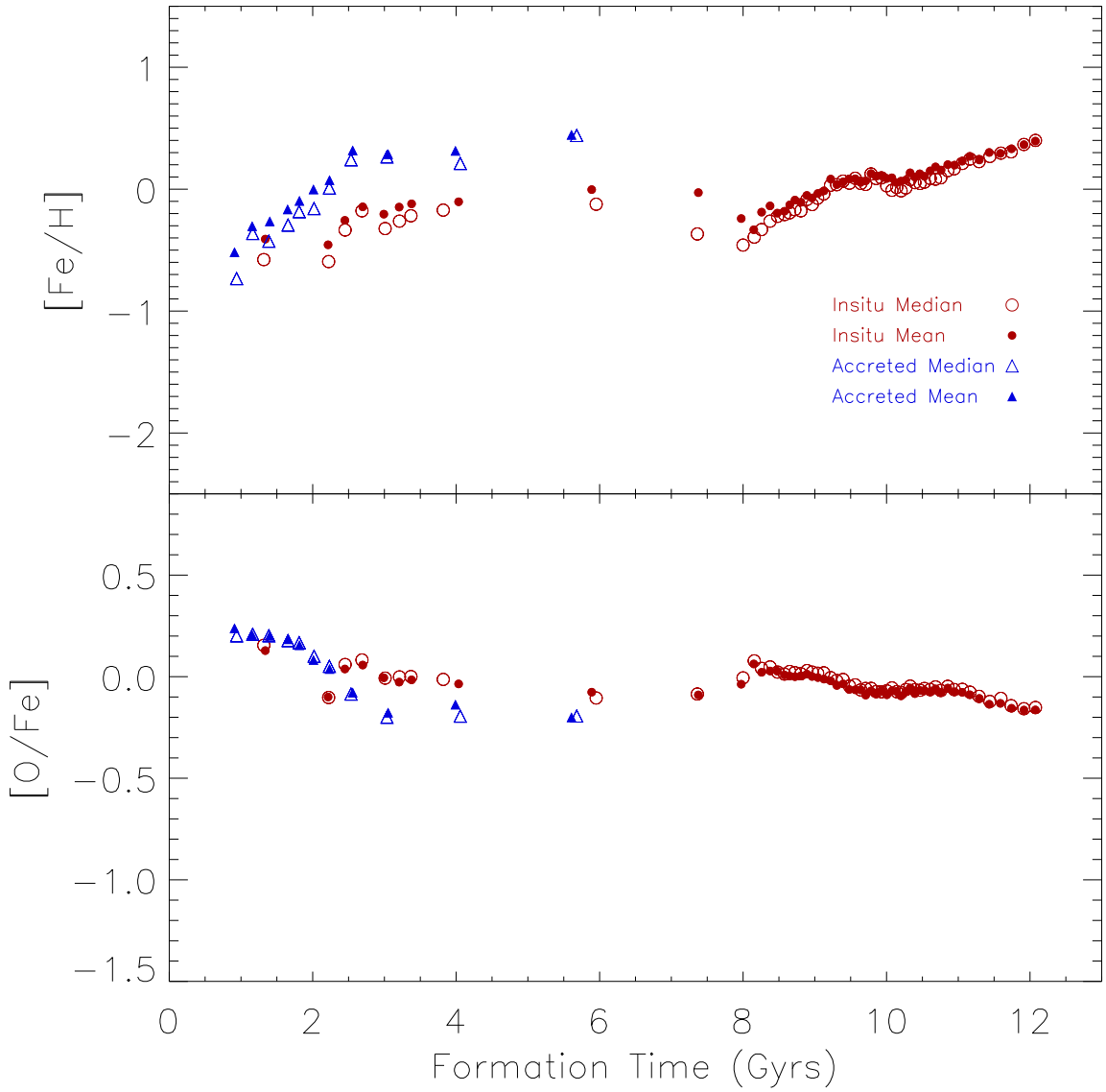

Figure 4.4: Same as in Fig. 4.3, however, now plotting only the median and mean every 100 particles to make the trends in our data clearer. The open and filled circles represent the median and mean for *in situ* stars, respectively, and the open and filled triangles the median and mean for accreted stars, respectively.

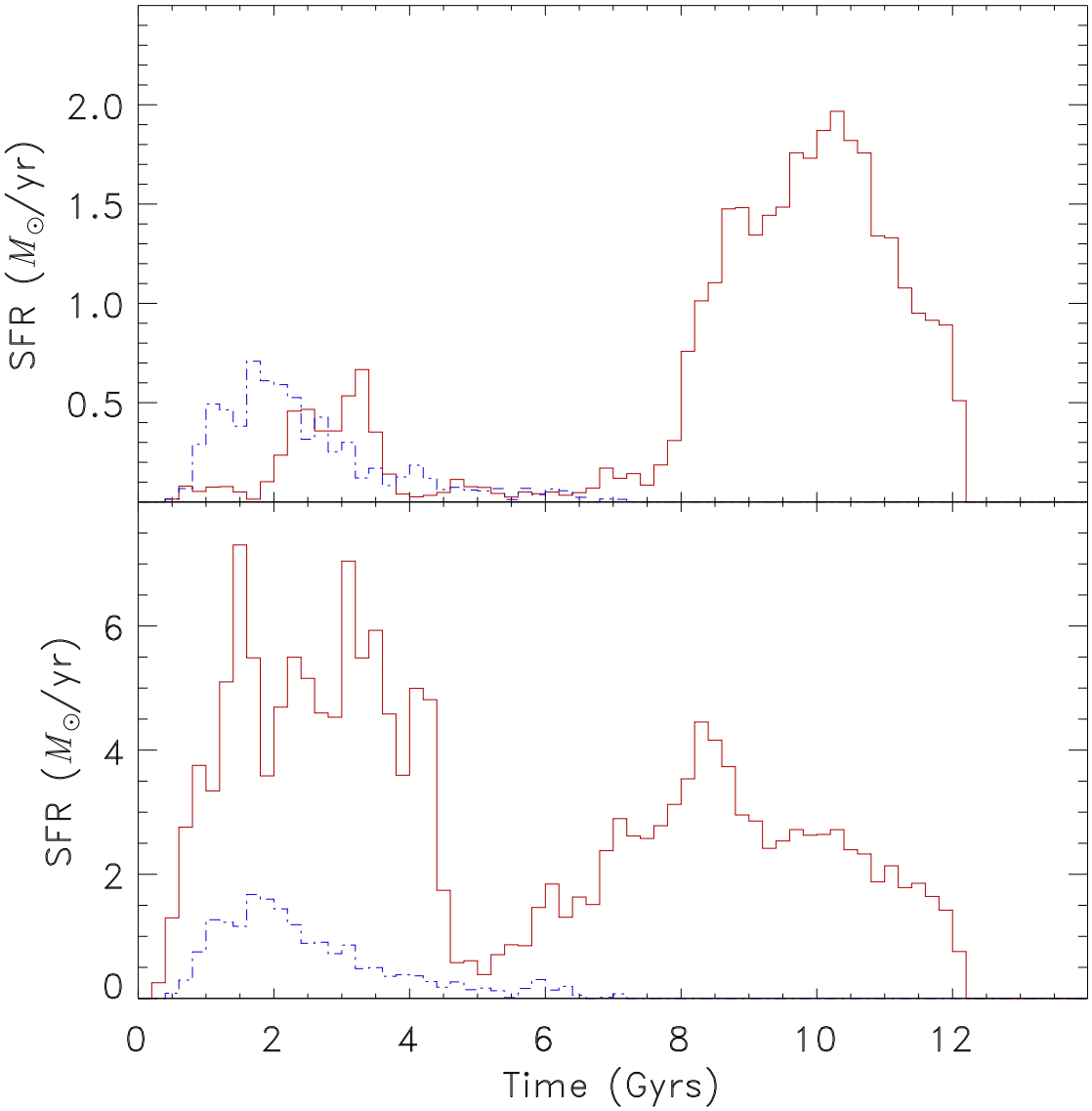

Figure 4.5: SFR history of our defined disc stars (upper panel) showing the contributions from *in situ* and accreted stars (red solid and blue dot-dashed lines, respectively). In the lower panel we replot the SFR for our sample of disc stars but now in the region $0 < R_{\rm GC} < 10$ kpc and $|z| < 1$ kpc, with a galactic rotation velocity between 150 and 350 kms^{-1}.

situ stars'. Stars that form at a radius greater than 20 kpc from the centre of the galaxy and end up within the disc at the final timestep, we term 'accreted stars'. We chose 20 kpc arbitrarily because we discuss only rough trends between the two populations. We experimented using a larger radius up to 30 kpc, and generally found the same conclusions.

Fig. 4.3 shows [Fe/H] and [O/Fe] versus formation time for accreted and *in situ* stars. The evolution of disc metallicity with time has been observed in disc stars of the Milky Way (Reddy et al., 2003; Bensby et al., 2004; Bernkopf & Fuhrmann, 2006) although only with small number statistics. Oxygen is one of the so-called α-elements. These elements are primarily produced in massive stars with short lifetimes that explode as SNe II. Iron is produced predominantly in SNe Ia, from lower mass binary stars with longer lifetimes (we apply the model proposed by Kobayashi et al., 2000). Accreted stars have lower [Fe/H] and higher [α/Fe] since in this particular galaxy they form in early epochs before the enrichment from SNe Ia becomes important. *In situ* stars continue to be born up until the final timestep of the simulation. Fig. 4.4 shows the same information but taking the median and mean every 100 particles to show the trends more clearly. There is only a very small difference between the two methods (especially for the younger stars which are the focus of this chapter).

In the upper panel of Fig. 4.5, we replot the SFR history for our sample of disc stars now including the individual contributions from *in situ* and accreted stars. We see that the accreted stars contribute prominently to the fraction of old stars in our sample. At later times we see that the disc grows due to the formation of stars *in situ* in the disc. *In situ* stars therefore are mainly responsible for the formation of the disc at times later than 7 Gyr. This is closely related to the formation time of the bulge of this galaxy, which takes place over the first few Gyr (see Fig. 3.1). We can therefore deduce that the disc of our simulated galaxy only really begins to build up after the bulge is fully formed. However, Fig. 4.5 also demonstrates that some disc stars can form *in situ* during the formation epoch of the bulge stars due to mergers.

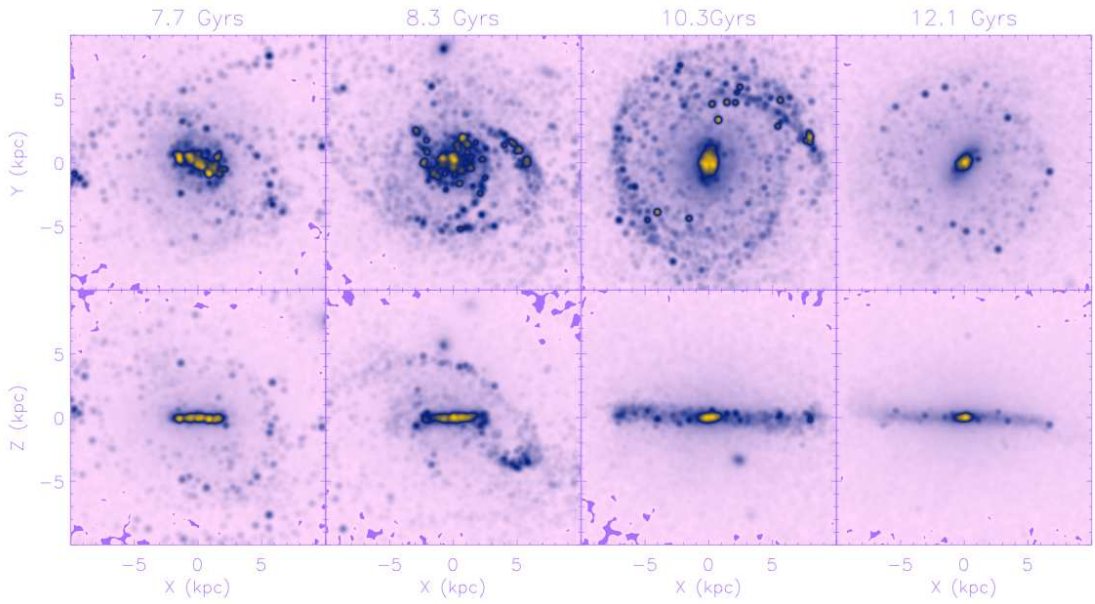

Figure 4.6: Face-on (upper) and edge-on (lower) view of the evolution of the galaxy from t = 7.7 to 12.1 Gyr, colour coded by the expected *V* band luminosity (Bruzual & Charlot, 2003). The brightest regions are the densest. The knots are due to young bright particles.

It is possible that some of these stars may have formed in the vicinity of the bulge, but ended up in the disc at the final timestep (Sellwood & Binney, 2002; Roŝkar et al., 2008; Sanchez-Blazquez et al., 2009). In the lower panel of Fig. 4.5, we replot the SFR history as in the upper panel, but now including the central 4 kpc of the bulge component. We see that star formation in the inner region starts earlier than in the outer region. In Fig. 4.6 we show how our simulated galaxy evolves from t = 7.7 to 12.1 Gyr. We can clearly see that before 8 Gyr the radial extent of the galaxy is less than 4 kpc. Only after 8 Gyr does the disc grow beyond 4 kpc. This explains why in Fig. 4.2 and the upper panel of Fig. 4.5, it appears as if the galaxy suddenly starts forming stars at around $t = 8$ Gyr. It is simply due to our selection criteria for the extent of the disc region. Notice that our simulated galaxy seems to grow to its maximum size at 10.3 Gyr. This is because our simulated galaxy suffers from the overcooling problem, whereby gas cools too rapidly at early times forming stars and causing the galaxy to be too gas poor at later times. At these later times when much of the gas has cooled out of the disc, the disc can easily be "overenriched"

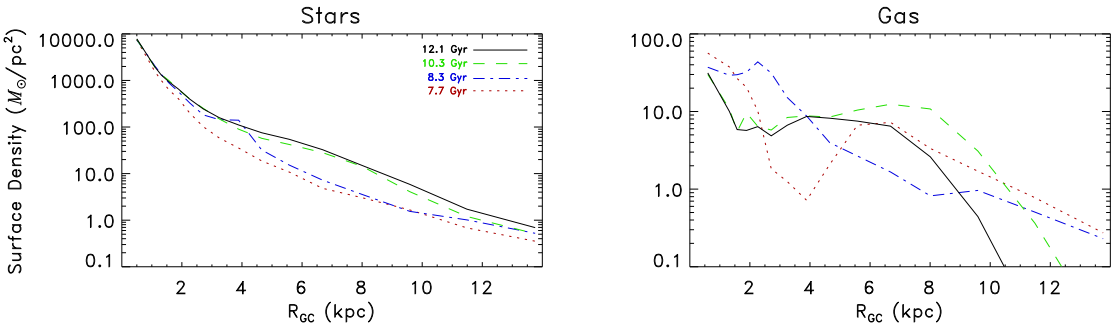

Figure 4.7: Surface density profile of stars (left) and gas (right) in the galaxy from t = 7.7 to 12.1 Gyr.

by feedback events. This means that we should not rely on the absolute values of our abundances in the disc. We focus only on the abundance *trends* along the disc and draw conclusions from these trends. Fig. 4.7 shows the surface density radial profiles of both the stars and gas for our galaxy corresponding to the times given in Fig. 4.6. The stellar surface density of the inner region ($R_{\rm GC} < 4$ kpc) increases earlier ($t < 8.3$ Gyr) than the outer region. From these figures, we deduce that the simulated galaxy formed inside-out. In our defined disc region, the gas density is greatest at 10.3 Gyrs. This corresponds to the peak of the SFR in the disc.

In Fig. 4.8 we plot the median of [O/Fe] versus [Fe/H], using the median value for every 100 particles as described in Section 4.2. Here, the abundance of oxygen is used to represent α-elements. Accreted stars have higher [α/Fe] and lower [Fe/H] compared to *in situ* stars, corresponding to them being formed earlier. We find that 90% of the accreted stars fell into the region within a radius of 10 kpc before $t = 8$ Gyr. This is before the disc starts forming at radii greater than 4 kpc (Figs. 4.3 and 4.5). As a result there exists a distinct population of accreted stars with high [α/Fe]. These accreted stars likely end up in a thick disc (Abadi et al., 2003b; Helmi et al., 2006). In fact, the velocity dispersion of the vertical component of the disc is 96 and 58 kms^{-1} for accreted and *in situ* stars, respectively, in the simulated galaxy. Note that this is significantly higher than what is observed around the solar neighbourhood (e.g. Holmberg et al., 2009).

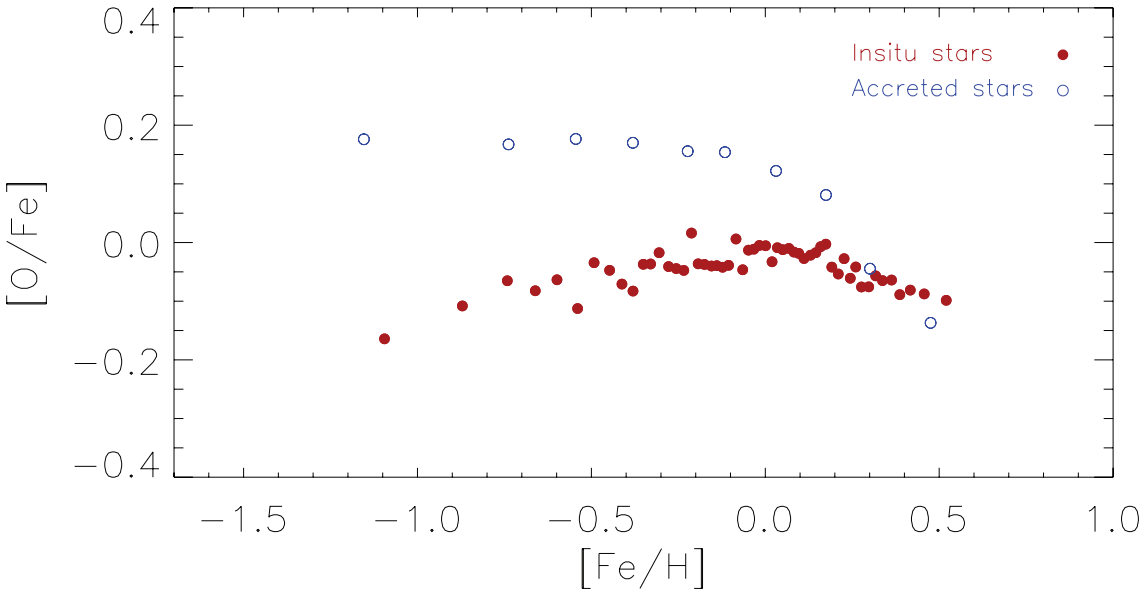

Figure 4.8: [O/Fe] versus [Fe/H] at the final timestep. Red filled and blue open circles are *in situ* and accreted stars, respectively. As expected from Fig. 4.3 accreted stars have higher [O/Fe] ratios.

Our chemodynamical simulation demonstrates that if such accreted stars are formed *exclusively* at early epochs, then an accretion origin for the thick disc can explain the observed distinct difference in [α/Fe] between the thick and thin disc in the Milky Way (e.g. Gratton et al., 1996, 2000; Fuhrmann, 1998; Prochaska et al., 2000; Tautvaišienė et al., 2001; Feltzing et al., 2003; Reddy et al., 2003; Schröder & Pagel, 2003; Bensby et al., 2005; Fuhrmann, 2008).

We note however that it is more difficult to explain the thick disc stars with higher metallicity as the accreted stars, because the accreted stars formed in smaller galaxies that are likely to be more metal poor. Although our simulation shows high metallicity and low [O/Fe] accreted stars, since we assume a negligible SNe feedback model (Section 4.2) and ignore the UV background radiation, our simulation likely overestimates the metallicity of the accreted stars formed in such small galaxies (e.g. Governato et al., 2007; Brooks et al., 2007). The majority of thick disc stars in the Milky Way are relatively metal rich, and may require more intense star formation which may be more readily associated with the *in situ* population (e.g. Chiappini

et al., 2001; Brook et al., 2004b; Schönrich & Binney, 2009c).

4.3.2 Radial Trend of Chemical Properties and Age Dependence

In our simulation, we follow the formation history of our galaxy from very early times to the final timestep of the simulation ($z = 0.1$). Since the differently aged populations in the galaxy likely hold different memories of the formation history, we analyse the properties of stars with different ages. Fig. 4.2 clearly shows that our simulated galaxy has two periods of disc star formation. The second and major episode is of particular interest as this is what predominately leads to the formation of disc stars from smooth gas accretion. Prior to this epoch, multiple mergers prevent smooth gas accretion to form a disc (Rahimi et al., 2010). The second and major period lasts from $t = 7$ to 12 Gyr and is characterised by a rapid rise and fall in the SFR. It would be interesting to consider the differences between the stars formed at the two different parts of this period of star formation. Furthermore, since we later would like to compare our results with the relatively young stars found in the Galactic disc, we therefore decided to divide the stars formed *in situ* during the second episode into 'intermediate' disc stars ($7 < t_f < 10$ Gyr) and 'young' disc stars formed during the final 2 Gyr ($t_f > 10$ Gyr). Note that in this section, we only focus on *in situ* stars, to track the building up history of the disc.

In the top panel of Fig. 4.9, we plot [Fe/H] against radius from the galactic centre, $R_{\rm GC}$, for intermediate-age and young stars. Here again we have plotted the median for every 100 particles in each radial bin. The straight and dashed red lines represent the best fit to the data. Here we only consider the disc stars within 10 kpc, because in the outer region there are too few particles to represent the lower density regions of the disc. We clearly see a negative [Fe/H] slope with $R_{\rm GC}$. The younger the stars, the higher the median metallicity at any given $R_{\rm GC}$. Table 4.2 shows the fitted slope to the median abundances for the intermediate-age and young

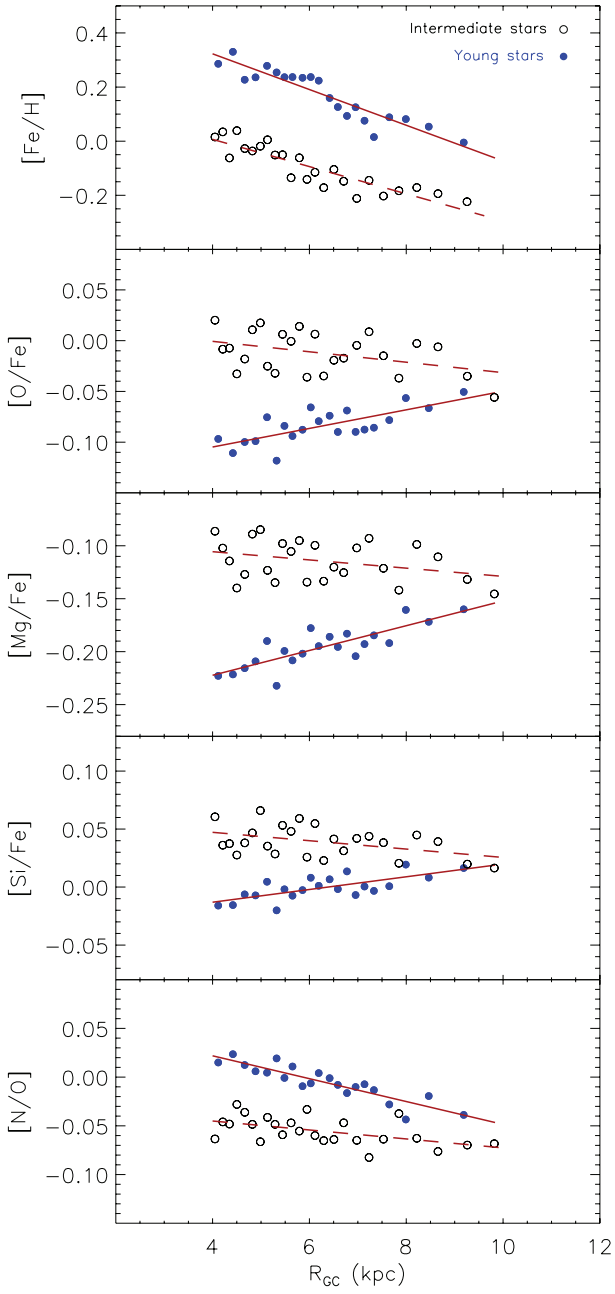

Figure 4.9: [Fe/H], [O/Fe], [Mg/Fe], [Si/Fe] and [N/O] versus galactocentric radius. The black open and blue filled circles represent intermediate-age and young stars, respectively. The red dashed and solid lines are the fitted linear function to the median of the intermediate-age and young stars, respectively, whose slopes are listed in Table 4.2.

Table 4.2: Abundance gradients for various element abundance ratios for the intermediate-age and young stars

Abundance Trends (dex kpc^{-1})		
Abundance ratio	Intermediate	Young
[Fe/H]	−0.050	−0.066
[O/Fe]	−0.005	0.009
[Mg/Fe]	−0.004	0.012
[Si/Fe]	−0.004	0.006
[N/O]	−0.005	−0.012

stars.

Note that the exact value of these gradients is not important and depends slightly on how we measure or sample the data. Below we only discuss qualitative trends of these gradients. The intermediate-age and young stars have a similar slope in [Fe/H], although for the young stars the slope is slightly steeper. Therefore, we find that during the major disc formation phase there is little evolution of the metallicity gradient, although the metallicity increases with time. This seems to be consistent with what was found by model A of Chiappini et al. (2001) in the latter epoch of evolution. However, note that our cosmological simulations involve more complex processes, such as radial mixing of gas and stars, and a complex gas accretion history. For the young stars of the disc we clearly see a negative slope in [Fe/H] with $R_{\rm GC}$. This kind of detailed abundance observations along the disc is only really available for our Milky Way. Interestingly, various observational studies (Twarog et al., 1997; Friel et al., 2002; Yong et al., 2005; Sestito et al., 2008; Magrini et al., 2009a; Pancino et al., 2010) have found similar abundance trends for young stars to what we see in our simulated galaxy.

The second row of Fig. 4.9 shows [O/Fe] against $R_{\rm GC}$ using the same plotting conventions, and Table 4.2 shows the slope in the median abundances for both the intermediate-age and young stars. Generally speaking we see a slope which is close to being consistent with flat. However for the young stars, we do see a slight positive

trend in the median. This positive slope is also observed for Galactic open clusters in Yong et al. (2005) and Pancino et al. (2010). One should note that the age range for the young stars roughly corresponds to the Yong et al. (2005) and Pancino et al. (2010) open clusters. Also note however that the Yong et al. (2005) sample had a stronger positive gradient than the Pancino et al. (2010) sample, and that the actual slope is still uncertain. Chiappini et al. (2001) showed that infalling gas from the halo can impact the metallicities in the outer regions of the disc. In Fig. 4.10, we analyse [O/Fe] for gas and stars younger than 1 Gyr at $t = 11.2$ Gyr when young stars in Fig. 4.9 are forming. Fig. 4.10 shows that stars inherit their abundance patterns from the gas. We also plot [O/Fe] for the yield in the last 1 Gyr from our disc stars, i.e. stars at $|z| < 1$ kpc and $4 < R_{\rm GC} < 10$ kpc and rotating with $150 < V_{rot} < 350$ kms^{-1}. More than 70% of stars in the disc region, i.e. $4 < R_{\rm GC} < 10$ kpc and $|z| < 1$ kpc satisfy our criteria for the rotation velocity of the disc stars, yet 93% of the mass fraction of metals is ejected from such disc stars, due to the young age of this population. It is therefore apparent that the yields from our disc stars are the dominant source of chemical enrichment, and the yield from the spherical component is negligible in our simulation[1].

Abundance ratios, such as [O/Fe] are very sensitive to the star formation histories. In order to investigate how the star formation history changes with $R_{\rm GC}$, and thereby better understand these trends, in Fig. 4.11 we plotted the SFR against time for three different $R_{\rm GC}$ bins along the disc. Our three regions, going radially outwards were defined as extending from 4−6 kpc, 6−8 kpc and 8−10 kpc. The magnitude of the SFR decreases with increasing $R_{\rm GC}$. By 8−10 kpc (third panel from the left) there is a significant reduction in the magnitude of the SFR. More interestingly, however, the peak of the SFR occurs at slightly later times as $R_{\rm GC}$

[1]In Fig. 4.10, [O/Fe] of stars, gas and yields are slightly different from each other. However, stellar abundances come from young stars which formed in the last 1 Gyr, yields are only for the last 1 Gyr, and the gas is the abundance at 11.2 Gyr. In addition, the plotted stellar and gas metallicities are median values at each radial region. Stars formed only from high-density gas. Considering these facts, it is not surprising that they are different.

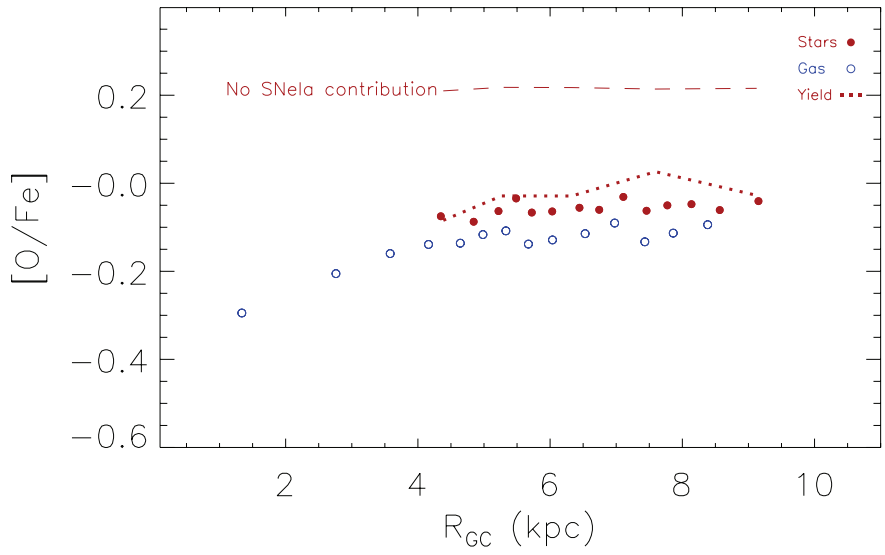

Figure 4.10: [O/Fe] versus galactocentric radius at 11.2 Gyr. The blue open circles and red dots represent gas and young stars, respectively. The small red dots represent the yield from the disc stars in the last 1 Gyr. The red dashed line redraws this yield excluding the contribution from SNe Ia.

increases. Together with Figs 4.5−4.7 this provides clear evidence for the inside-out formation of the disc. As a result, there is a higher fraction of young stars in the outer regions of the disc. This can explain the [O/Fe] enhancement because a more significant enrichment from SNe II is occurring in the outer region. On the other hand, in the inner region, there are relatively more old stars which are the precursors of SNe Ia (producing more Fe). Fig. 4.10 also shows the yield coming exclusively from SNe II, which show a constantly high [O/Fe] at all radii. This also indicates that the difference in the significance of SNe Ia enrichment is driving the positive [O/Fe] gradient. Therefore, we conclude that inside-out formation of the disc naturally leads to a higher fraction of young stars in the outer regions and a positive [α/Fe] slope in the young population of the disc.

In Fig. 4.9 we also show how [Mg/Fe] and [Si/Fe] vary with $R_{\rm GC}$ and Table 4.2 shows the value for the median fitted slopes for the intermediate-age and young stars. Magnesium and silicon are also α-elements, and are mainly produced in massive stars. Therefore we observe similar trends to the [O/Fe] case. However,

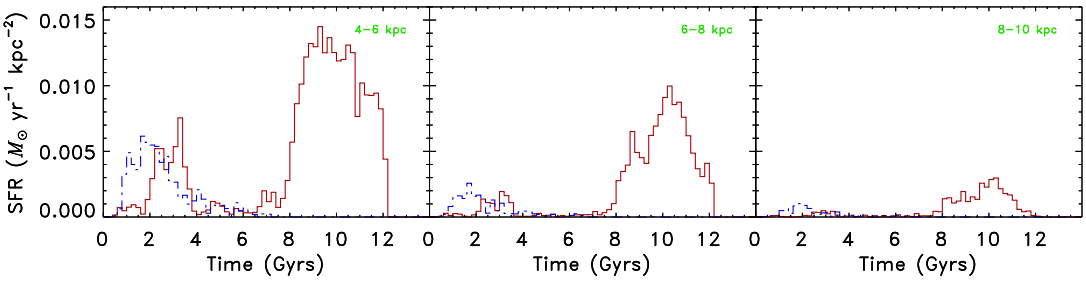

Figure 4.11: SFR versus time at different radial regions along the disc plane

for the young stars, [Si/Fe] shows a slightly flatter slope compared to [O/Fe] and [Mg/Fe] cases. This could be because silicon is also significantly produced by SNe Ia (we adopt the yields in Iwamoto et al., 1999) compared to SNe II as also shown in Gibson et al. (1997).

We also analyse [N/O] as shown in the final row of Fig. 4.9 and the fitted slopes are presented again in Table 4.2. [N/O] is expected to show an opposite trend to the [α/Fe] case. Accordingly, for the young stars we see a negative slope that has an opposite sign to the [α/Fe] case. From Fig. 4.11, this is because at the outer radii, a greater fraction of young stars exist which end up as SNe II and thereby produce more oxygen making [N/O] lower. On the other hand, more intermediate-mass stars (we adopt yields in van den Hoek & Groenewegen, 1997) died in the inner regions, producing more nitrogen, which makes [N/O] higher.

As mentioned above, in the Milky Way, [α/Fe] in open clusters also shows a tentative trend of increasing with radius (Yong et al., 2005; Pancino et al., 2010). If the chemical composition of open clusters represents the properties of the field disc stars at similar galactocentric radii, our simulation demonstrates that the observed abundance trends can be explained by a higher fraction of young stars in the outer region due to an inside-out formation of the Galactic disc. Note that although we

rely on the yields from SNe II, SNe Ia and intermediate-mass stars as explained in Section 4.2, some of these values are still controversial and there are a variety of yields suggested by several groups. Some different yield sets may be able to lead to the positive [O/Fe] gradient without having inside-out star formation. In addition, if somehow the infalling gas strongly contributes to the chemical abundance in the gas disc, and has lower [O/Fe] in the inner region, this can also explain the positive [O/Fe] gradient. Needless to say, there are more scenarios that can explain the positive [O/Fe] gradient. Our scenario is not a unique solution, but our simulation demonstrates one possible explanation (derived with a fully cosmological simulation) which is also naturally predicted from disc galaxy formation in a ΛCDM universe.

4.4 Summary

In this study we have analysed the chemistry and the dynamics of the disc stars in a cosmologically simulated disc galaxy. The galaxy was similar in mass and size to the Milky Way, and contained distinct gas and stellar disc components (Bailin et al., 2005; Connors et al., 2006).

The simulated galaxy showed two episodes of star formation which led to the build-up of the stellar disc. The first occurred at very early epochs and was mainly due to accreted stars being brought into the galaxy as a result of mergers. These early mergers also built up the bulge (Rahimi et al., 2010). Therefore, our simulation demonstrates that some stars accreted earlier can become disc stars, if they happen to have the right angular momentum. Our simulation also has old stars formed *in situ*. It is interesting to note that even during the mergers that are mainly building up the bulge some disc stars can form *in situ* and stay in the disc for a long time. Intriguingly, in this galaxy, a fraction of the bulge stars have a significant rotational velocity component (Rahimi et al., 2010).

The second episode of star formation starts after the mergers cease and continues till the final timestep. In this period, smooth gas accretion builds up the disc and

stars formed *in situ*. We have analysed the radial trend of [Fe/H], [O/Fe], [Mg/Fe], [Si/Fe] and [N/O] for these *in situ* stars, especially focussing on the relatively young stars ($t_f < 2$ Gyr). Our simulated galaxy shows a negative [Fe/H] gradient with $R_{\rm GC}$. Interestingly, the Milky Way has a similar trend as recently observed for open clusters (Friel et al., 2002; Pancino et al., 2010) and cepheids (Luck et al., 2003; Andrievsky et al., 2004; Lemasle et al., 2008; Pedicelli et al., 2009). More interestingly, we also found a positive [α/Fe] gradient for the young stars in the disc. This trend is similar to the recently observed [α/Fe] gradient for open clusters in the Milky Way (Yong et al., 2005; Pancino et al., 2010) as well as to predictions from some chemical evolution models (e.g. Magrini et al., 2009a).

We find that inside-out formation of the disc can naturally produce such negative [Fe/H] and positive [α/Fe] gradients. In our simulated galaxy, the magnitude of the SFR declines in the outer disc. Thus we induce a more progressed enrichment in the inner region and negative [Fe/H] slope. We also find that the peak of the SFR occurs at a later epoch in the outer regions of our simulated galaxy, which is clear evidence for inside-out disc formation. As a result, the outer region in the disc harbours a greater fraction of young stars that produce more SNe II and cause higher [α/Fe]. This also leads to a negative slope of [N/O], because in the inner region a greater fraction of low-mass stars produce more nitrogen. These results demonstrate that such radial gradients of chemical abundances are sensitive to the formation history of the disc.

Note that our simulated galaxy is not a late-type galaxy like the Milky Way, but is more like an early-type disc galaxy. Therefore, the age distribution of the disc stars in our simulated galaxy is very different from the Milky Way disc stars. However, we should be able to apply our simple conclusion to any disc that formed *in situ* as a result of smooth gas accretion. Therefore, we suggest that the observed positive [α/Fe] gradients in the Milky Way disc stars can be explained if the Milky Way also experienced a clear inside-out formation and harbours a greater fraction of young stars in the outer region. Although this is not a unique scenario and we

do not reject other scenarios, this is naturally expected in a ΛCDM universe.

Recently, Williams et al. (2009) found clear evidence for inside-out disc formation in M33 and claimed that there is a greater fraction of old stars in the inner regions of the disc of M33. Various authors have found that the metallicity gradient in the M33 disc decreases going away from the centre (e.g. Magrini et al., 2007a,b; Viironen et al., 2007; Rosolowsky & Simon, 2008; Rubin et al., 2008; Magrini et al., 2009b; Cioni, 2009). More measurements of abundance ratios across the M33 disc would be extremely interesting (such as: e.g. Esteban et al., 2009). Recently, there have also been attempts to measure the chemical properties along the disc radius for disc galaxies other than our Milky Way (e.g. Ryder et al., 2005; MacArthur et al., 2009). Interestingly, Yoachim & Dalcanton (2008) find a tentative detection of more α-enhanced populations and younger luminosity weighted mean ages in the outer disc region of the disc galaxy FGC 1440.

Our results are useful for comparing observations to our simulation where we can trace the formation history. However, we also admit that the current chemodynamical simulation model should be improved. For example, since we do not allow metal mixing between particles, we likely overestimate the scatter of the metallicity distribution and [α/Fe] at different radii. We are working on improving our chemodynamical model, and new simulations will provide valuable information to disentangle the formation history of the disc galaxies from current and future observations.

Chapter 5

Towards a Self-consistent Numerical Model of Late-type Galaxies: Calibrating the Effects of Sub-grid Physics on Galactic Models

5.1 Introduction

The process of galaxy formation and evolution remains one of the most outstanding problems in modern astrophysics. From a cosmological point of view, great progress has been made including the development of a theory, Λ cold dark matter (ΛCDM) cosmology which accurately explains the present-day large-scale distribution of galaxies from the primordial small-scale density fluctuations in the early Universe. The actual processes which govern individual galaxy formation and evolution are far less well understood however. One of these important processes is that of star formation itself. Schmidt (1959) suggested that the star formation rate

(SFR) density and the interstellar gas density in our Galaxy were related by a simple power-law relation of the form $\rho_{\rm SFR} \propto (\rho_{\rm gas})^n$, where n is the power-law index. Schmidt (1959) originally suggested a value for n of 2, so that the rate of star formation varies with the square of the gas density. Studying the form of the observed star formation law, Kennicutt (1989, 1998b) analysed the SFR *surface* density and the gas *surface* density for a much larger sample of galaxies and over a wider range of gas densities, determining the power-law index n to be equal to 1.4 (see also Kennicutt, 1998a). We now refer to the empirical relation between SFR and gas surface density as the Schmidt−Kennicutt (SK) relation. Recently, the SK relation has been studied in much more depth (e.g. Bigiel et al., 2008; Leroy et al., 2008), including observing the relation for individual components of the gas (HI and molecular) and as a function of environment. Several observational studies found evidence for a two-slope SK relation (e.g. Bigiel et al., 2008). Bigiel et al. (2008) showed that a break exists at gas surface densities of 9 $\rm M_\odot\ pc^{-2}$, below which the slope of the SFR steepens. This break corresponds to the transition between the HI and molecular phase of the gas. Theoretical models also predict such breaks in the SK relation. For example Krumholz et al. (2009) made a theoretical model consisting of three prescriptions: molecular self-shielding, internal feedback and turbulent regulation in molecular clouds which address the physics responsible for determining the SFR on local scales and successfully managed to reproduce the observed trends in the SK relation.

The SK relation is of great importance as it is used for the calibration of numerical codes of galaxy formation and evolution, with the SFR often explicitly required to obey a SK-type law (e.g. Springel & Hernquist, 2003; Booth et al., 2007; Shaye & Dalla Vecchia, 2008). Some more recent studies, however, do not force the SFR to follow a SK-like relation, and so its adherence to this law is a prediction of the model (e.g. Kravtsov, 2003; Tasker & Bryan, 2006, 2008; Wada & Norman, 2007; Saitoh et al., 2008; Governato et al., 2010; Hopkins et al., 2011). For example, Saitoh et al.

(2008) use very high resolution simulations to resolve the star-forming regions. Using a high star formation density threshold $n_{\rm H} = 100$ cm^{-3} they find that at higher resolutions, their results become much less sensitive to the choice of sub-grid physics prescription, and almost independent of the star formation efficiency parameter.

Recent observational studies show that the gas velocity dispersion is also an important factor to consider for any galaxy evolution model. Dib et al. (2006) demonstrate that there is a characteristic value of $\sim 8{-}10$ km s^{-1} for the observed HI gas velocity dispersion for galaxies with a lower star formation rate. They also show that there are galaxies with gas velocity dispersion higher than ~ 10 km s^{-1} and their velocity dispersion is correlated with the star formation rate. Using HI line width maps obtained for 11 disc galaxies of The HI Nearby Galaxy Survey (THINGS; Walter et al., 2008), Tamburro et al. (2009) demonstrate that all of their sample galaxies (except IC 2574) showed a high HI velocity dispersion (>10 km s^{-1}) at the centre and a systematic radial decline reaching ~ 10 km s^{-1} by r_{25} − roughly the radial extent of the star-forming disc. The radial decline in velocity dispersion was well correlated with the radial decline of SFR and therefore they suggested that high gas velocity dispersion is induced by supernovae feedback. Agertz et al. (2009) showed that turbulence driven by gravitational instabilities can explain the observed gas velocity dispersion at the level of 10 km s^{-1}, and further demonstrated that supernovae feedback contributes to increase the gas velocity dispersion where the star formation rate is higher than 10^{-3} M$_\odot$ yr^{-1} kpc^{-2}.

The implications of such studies are that the gas velocity dispersion should now be used as an additional constraint for any new numerical simulation codes of galaxy evolution. Recently, Dobbs et al. (2011) performed isolated disc galaxy evolution simulations to investigate how the properties of the interstellar medium (ISM), molecular clouds and SFR depend on the level of stellar feedback, comparing their results against both the observed SK relation and gas velocity dispersion. They found that supernovae were vital in reproducing the observed velocity dispersions and scale heights of the individual components of the ISM. Recently, Pilkington

et al. (2011) analysed both the SK and HI velocity dispersion relations for a fully consistent cosmologically simulated late-type dwarf spiral galaxy.

In this chapter, we initiate a project to create an accurate and self-consistent numerical model for late-type spiral galaxies. To this end, we have been developing our numerical simulation code `GCD+` (Kawata & Gibson, 2003a). The new version of the code includes new features and improvements to a number of aspects of the modelling of galaxy formation and evolution, including new star formation and feedback recipes. The overall effect of these changes is that the code can now capture and accurately follow the effects of powerful supernovae explosions on the evolution of the galaxy. The details of the new model are described in the next section. In this study, we set up an isolated disc galaxy consisting of gas and stellar discs with no bulge component, in a static dark matter halo gravitational potential. To calibrate our new model, we here focus on M33-*like* bulgeless galaxies. M33 is a suitably chosen late-type bulgeless spiral galaxy. Its close proximity in the Local Group means it has been a favourite choice for detailed observational campaigns (e.g. Heyer et al., 2004; Verley et al., 2010). Its smaller size compared to the Milky Way also means that we can simulate it to much higher resolution using the same number of particles. M33 also lacks a supermassive black hole at its centre (Merritt et al., 2001), a factor which helps simplify the modelling and analysis. Therefore, M33-*like* galaxies are ideal target galaxies for testing and calibrating the numerical modelling of the physical processes in galaxy evolution. Note that our aim is *not* to reproduce completely the observed properties of M33. It is likely that M33 had a recent interaction with M31 (McConnachie et al., 2009; Putman et al., 2009) and so it may not be a typical galaxy. We focus more on the *general* observed properties for M33-*sized* disc galaxies, such as the SK relation and the gas velocity dispersion. Also note that the simulations shown in this chapter adopt similar resolution to the current highest resolution cosmological simulations of Milky Way sized galaxies (e.g. Guedes et al., 2011). We demonstrate that at this resolution, sub-grid model parameters are important.

The chapter is organised as follows. In Section 5.2, we describe the galaxy model together with some new features of our numerical simulation code. In Section 5.3, we present our results and analyses. We summarise our findings and present our conclusions and planned future work in Section 5.4.

5.2 The Code and Model

5.2.1 New Version of GCD+

To simulate our galaxy, we use an updated version of our original galactic chemodynamical evolution code GCD+ (Kawata & Gibson, 2003a). GCD+ can be used in studies of galaxy formation and evolution in both a cosmological and isolated setting. GCD+ incorporates self-gravity, hydrodynamics, radiative cooling, star formation, supernova feedback, and metal enrichment. The new version of the code includes metal diffusion suggested by Greif et al. (2009). Our recent update and performance in various test suites will be presented in a series of our forthcoming papers (Kawata et al. in preparation). Here we briefly describe the major points of our recent upgrade. We have implemented a modern scheme of SPH suggested by Rosswog & Price (2007). We follow their artificial viscosity switch (Morris, 1997) and artificial thermal conductivity to resolve the Kelvin−Helmholtz instability (Kawata et al., 2009). Following Springel & Hernquist (2002), instead of the energy equation, we integrate the entropy equation. As suggested by Saitoh & Makino (2009), we have added the individual time step limiter, which is crucial for correctly resolving the expansion bubbles induced by supernovae feedback (see also Merlin et al., 2010; Durier & Dalla Vecchia, 2012). We also implement the fully asynchronous split time-integrator scheme (Saitoh & Makino, 2010) which allows the use of different timesteps for integrating hydrodynamics and gravity. The code now also includes adaptive softening for both the stars and gas (Price & Monaghan, 2007) although in this current study we only implement it for the gas particles (see below).

Radiative cooling and heating is calculated with `CLOUDY` (v08.00: Ferland et al., 1998). We tabulate cooling and heating rates and the mean molecular weight as a function of redshift, metallicity, density and temperature adopting the 2005 version of the Haardt & Madau (1996) ultraviolet (UV) background radiation. We also add a thermal energy floor following Robertson & Kravtsov (2008) to keep the Jeans mass higher than $2N_{\rm nb}m_{\rm p}$, where $N_{\rm nb}$ is the number of neighbour particles and $m_{\rm p}$ is the particle mass, to avoid numerical instability[1] (see also Bate & Burkert, 1997). In the resolution of simulations presented in this chapter (see below), the gas particle meets this condition around $n_{\rm H} = 1$ cm^{-3}, and the resolution is not high enough to resolve individual molecular clouds. Therefore, we allow the gas particle to become a star particle if the density becomes greater than $n_{\rm H} = 1$ cm^{-3}, i.e. the star formation threshold density, and if their velocity field is convergent, following the Schmidt law as described in Kawata & Gibson (2003a):

$$\frac{d\rho_*}{dt} = -\frac{d\rho_{\rm g}}{dt} = \frac{C_*\rho_{\rm g}}{t_{\rm g}}, \tag{5.1}$$

where C_* is a dimensionless SFR parameter and $t_{\rm g}$ is the dynamical time.

We assume that stars are distributed according to the Salpeter (1955) initial mass function (IMF). `GCD+` takes into account chemical enrichment by both Type II supernovae (SNe II; Woosley & Weaver, 1995) and Type Ia supernovae (SNe Ia; Iwamoto et al., 1999; Kobayashi et al., 2000) and mass-loss from intermediate-mass stars (van den Hoek & Groenewegen, 1997), and follows the chemical enrichment history of both the stellar and gas components of the system. The new version of `GCD+` uses a different scheme for star formation and feedback. We now keep the mass of the baryon (gas and star) particles completely the same, unlike Kawata & Gibson (2003b) or the majority of SPH simulations which include star formation. Although the basic strategy is similar to Lia et al. (2002) and Martínez-Serrano et al. (2008), a

[1]Robertson & Kravtsov (2008) define the Jeans mass limit for the thermal energy floor as $2N_{\rm Jeans}N_{\rm nb}m_{\rm p}$ rather than $2N_{\rm nb}m_{\rm p}$ and use $N_{\rm Jeans} = 15$, which is a much bigger mass limit than what we applied.

slightly different implementation is adopted. First, every star particle formed in the simulation is randomly assigned a mass group ID ranging from 1 to 61 (although 61 is chosen arbitrarily, it is a compromised selection to sample the stellar mass range and be similar to our resolution, i.e. number of neighbour particles). We can calculate that about 13 per cent of the mass is ejected by SNe II from a star cluster following the assumed IMF and Woosley & Weaver (1995). Therefore we set ID $= 1 - 8$ particles to be 'SNe II particles'. Each SNe II particle receives 1/8 of the energy and metals produced by SNe II depending on the age and initial metallicity. After the age reaches a time when 8/61 of the mass is ejected (about the lifetime of an 8-$M_\odot$ star, depending on metallicity), the whole star particle is changed back to a gas particle. We assume each supernova produces thermal energy $E_{\rm SN}$ (erg). We also assume that stellar winds from massive stars (> 30 $M_\odot$) produce thermal energy $E_{\rm SW}$ (erg s^{-1}) and add this to the SNe particles. We explore the effect of these parameters applying $E_{\rm SN} = 10^{50}$ and 10^{51} erg and $E_{\rm SW} = 10^{36}$ and 10^{37} erg s^{-1} (e.g. Weaver et al., 1977; Shull, 1980; Oey & Massey, 1994; Gibson, 1994). Consequently, SNe II particles have higher temperature and become metal rich. They can reach temperatures of $\sim 10^7$ K. Our method does not use the kinetic feedback scheme (e.g. Navarro & White, 1993; Springel & Hernquist, 2003; Kawata & Gibson, 2003a). We do not take into account radiative cooling until the particle turns back into a gas particle, similar in spirit to the blastwave feedback used in Mori et al. (1997); Thacker & Couchman (2000); Brook et al. (2004a) and Stinson et al. (2006). However, we calculate thermal energy for the SNe II particles following the SPH scheme and add the pressure from the SNe II particles to their neighbour particles, while the dynamics of the SNe II particles are only affected by gravity (see also Pelupessy et al., 2004). Note that we do not distribute the energy to the neighbouring particles, only the SNe II particle itself receives the thermal energy produced by SNe II and stellar winds. This guarantees to make the SNe II particles hot enough not to suffer from rapid cooling (see also Booth et al., 2007). The metals produced by SNe II are distributed from the SNe II particles through the

metal diffusion scheme of Greif et al. (2009), i.e. the metal diffusion applied to the SNe II particles is the same as the other normal gas particles. We apply a similar algorithm to star particles with different IDs. From the IMF about 30 per cent of the mass will be ejected after a cosmic time. Therefore, star particles with IDs ranging from 9 to 19 will turn back into a gas particle depending on the age of the star particle, which models the mass-loss from intermediate-mass stars and SNe Ia feedback. For these particles, we turn on radiative cooling during their mass-loss and SNe Ia. For example, ID 9 particles with solar metallicity represent mass-loss from 7 to 5.6 $M_\odot$ stars. When their age becomes older than the lifetime of a 7 $M_\odot$ star, they become a 'feedback particle'. The particle inherits the original metal abundance and receives additional metals that stars in this mass range produce (van den Hoek & Groenewegen, 1997), which are then diffused via the metal diffusion scheme applied. Their thermal energy is calculated taking into account radiative cooling with the SPH scheme, and the additional pressure from these feedback particles are applied to their neighbouring particles (especially for the higher ID particles with SNe Ia feedback). Once the particle becomes older than the lifetime of a 5.6 $M_\odot$ star, the particle becomes a normal gas particle. Due to this algorithm, the particle mass of stars and gas is always constant, and the mass resolution is kept constant.

The main free parameters of the new version of `GCD+` include the star formation efficiency, C_*, energy per supernova, $E_{\rm SN}$, and stellar wind energy per massive star, $E_{\rm SW}$. Especially, these parameters control the effect of feedback on star formation, which is the most unknown and possibly most important process in galaxy formation and evolution. This chapter explores the effect of these parameters and calibrates these parameters against the observed properties, such as the SK relation and the gas velocity dispersion.

5.2.2 Model Galaxy Setup

We are interested in investigating the evolution of a late-type disc galaxy of the order of size of M33. We therefore set up an isolated disc galaxy which consists of gas and stellar discs with no bulge component in a static dark matter halo potential. We use the standard Navarro−Frenk−White (NFW) dark matter halo density profile (Navarro et al., 1997), assuming a standard ΛCDM cosmological model with cosmological parameters of $\Omega_0 = 0.266$, $\Omega_{\rm b} = 0.044$ and $H_0 = 71 {\rm kms}^{-1}{\rm Mpc}^{-1}$:

$$\rho_{dm} = \frac{3H_0^2}{8\pi G}(1+z_0)^3 \frac{\Omega_0}{\Omega(z)} \frac{\rho_c}{cx(1+cx)^2}, \tag{5.2}$$

where

$$c = \frac{r_{200}}{r_s}, \quad x = \frac{r}{r_{200}}, \tag{5.3}$$

and

$$r_{200} = 1.63 \times 10^{-2} (\frac{M_{200}}{h^{-1}M_\odot})^{\frac{1}{3}} [\frac{\Omega_0}{\Omega(z)}]^{-\frac{1}{3}} (1+z_0)^{-1} h^{-1} \text{ kpc}, \tag{5.4}$$

where ρ_c is the characteristic density of the profile, r is the distance from the centre of the halo and r_s is the scale radius. The halo mass is set to be $M_{200} = 5.0 \times 10^{11}$ $\rm M_\odot$ and the concentration parameter is set at $c = 10$ (Robertson & Kravtsov, 2008).

The stellar disc is assumed to follow an exponential surface density profile:

$$\rho_d = \frac{M_d}{4\pi z_d R_d} {\rm sech}^2(\frac{z}{z_d}) \exp -(\frac{R}{R_d}), \tag{5.5}$$

where M_d is the disc mass, R_d is the scale length and z_d is the scale height. Following suggestions from observations of M33 and carrying out several test runs at lower resolution, we decided to use $M_d = 4.0 \times 10^9$ $\rm M_\odot$, $R_d = 1.4$ kpc and $z_d = 0.3$ kpc. A summary of the numerical values used for our model parameters in the initial model set-up is given in Table 5.1. We used 4×10^5 stellar particles in our simulations, giving each star particle a mass of 1×10^4 $\rm M_\odot$.

The gaseous disc is set up following the method described in Springel et al. (2005a). The radial surface density profile is assumed to follow an exponential law

Table 5.1: Simulation parameters

$C_{\rm NFW}$	$M_{\rm vir}$ ($\rm M_\odot$)	$r_{\rm vir}$ (kpc)	$M_{\rm Star}$ ($\rm M_\odot$)	$M_{\rm Gas}$ ($\rm M_\odot$)	$R_{\rm d,star}$ (kpc)	$R_{\rm d,gas}$ (kpc)	$z_{\rm d,star}$
10	5.0×10^{11}	163	4.0×10^9	2.0×10^9	1.4	4.0	0.3

like the stellar disc with a scale length, $R_{d,gas}$ almost three times larger than the stellar disc. The initial vertical distribution of the gas is iteratively calculated to reach hydrostatic equilibrium assuming the equation of state calculated from our assumed cooling and heating function. The total gas mass is 2.0×10^9 $\rm M_\odot$ and is equal to half the total stellar mass. Since we use 2×10^5 gas particles in each run, each SPH particle also has a mass of 1×10^4 $\rm M_\odot$. Note that this means both the star and gas particles have the same mass resolution in our simulations. This is not by chance but required from our new modelling of star formation, feedback and metal diffusion shown in Section 5.2.1. We apply the spline softening and variable softening length suggested by Price & Monaghan (2007) for SPH particles. We set the minimum softening length at 198 pc, which corresponds to the required softening for gas with solar metallicity and density of $n_{\rm H} = 1$ cm^{-3}, i.e. the assumed density threshold for star formation. For the star particles, we applied a fixed spline softening of 198 pc softening length. We summarise our simulation properties in Table 5.1. Column 1 represents the NFW halo concentration parameter. The second column represents the virial mass; the third column is the virial radius; columns 4 and 5 represent the mass of the stellar and gas disc, respectively. Columns 6 and 7 represent the scale lengths of the stellar and gas discs, respectively, and column 8 is the scale height for the stellar disc.

Before carrying out these simulations, test runs at ten times lower resolution were carried out with a greater range and more varied values for our parameters. Since these simulations could be completed in a short time (less than 24 hours) their purpose was to fix some of our simulation and model parameters as well as quickly analysing the effects of varying the model parameters and the initial conditions on

Table 5.2: Model parameters

Model	C_*	$E_{\rm SN}$ (erg)	$E_{\rm SW}$ (ergs^{-1})
Run 1	0.02	1.0×10^{50}	1.0×10^{36}
Run 2	0.2	1.0×10^{50}	1.0×10^{36}
Run 3	0.2	1.0×10^{51}	1.0×10^{36}
Run 4	0.2	1.0×10^{51}	1.0×10^{37}
Run 5	0.02	1.0×10^{51}	1.0×10^{37}
Run 6	0.05	1.0×10^{51}	1.0×10^{37}

the simulation results. For example, we fixed the initial gas fraction to keep the SFR and metal enrichment at reasonable values (too high gas fraction leads to too high SFR and too efficient enrichment). We also find that to prevent the bar instability the halo concentration parameter should not be too low, and we have chosen $\mathrm{C_{NFW}} = 10$. As we increase the mass resolution of the simulation, the simulation results should be less sensitive to the model parameters, such as the energy input from supernovae and stellar winds as well as the star formation efficiency (e.g. Saitoh et al., 2008; Governato et al., 2010). Of course, increasing the resolution gives more accurate results. However, the current resolution was chosen as it was the highest at which we could carry out the simulations in a reasonably short period of time. The results of the simulations are still sensitive to the model parameters at this resolution, and the calibrations of the parameters are still required.

5.3 Results

Using the galaxy simulation parameters shown in Table 5.1, we carried out six primary simulation runs, named runs 1−6 where we consecutively changed one extra model parameter between runs 1 and 4. Run 5 is for comparison with runs 1 and 4 and run 6 is our fine-tuned 'best model'. Our varying model parameters include C_*, $E_{\rm SN}$ and $E_{\rm SW}$. Run 1 has low values for all three of our model parameters. We carried out a simulation run (run 2) with $C_* = 0.2$, ten times higher star formation

efficiency. We shall refer to this model as the 'high-C_* model'. Another run (run 3) was done with $C_* = 0.2$ and $E_{\rm SN} = 1.0 \times 10^{51}$ erg. We call this run 'high-$E_{\rm SN}$ model'. In our fourth model run, we also increase $E_{\rm SW}$ by a factor of 10. We call this model our 'highest-feedback model'. Run 5 has the same high feedback parameters as in run 4, but with a low C_* value as in run 1. Run 6 is identical to run 5, except that we increase the value of C_* from 0.02 to 0.05. We chose this value based on the results of the previous runs, believing this to be our best model. Table 5.2 summarises the simulation runs and model parameters.

Fig. 5.1 shows face-on and edge-on snapshots of the stars and gas after 1 Gyr of evolution for our six runs. Large holes or 'bubbles' of varying sizes are clearly visible in the face-on gas distributions. These bubbles are produced mainly by SNe II explosions. The bubbles are much larger in runs 3−6 since the energy released per supernova explosion is 10 times greater in these models. The large bubbles in these models may survive for longer than one galactic rotation. The models with high feedback and star formation efficiency parameters (runs 3 and 4) produce the most turbulent vertical gas distribution, as can be seen in the edge-on images. Conversely, the vertical gas distribution of the discs of runs 1 and 2 are razor thin in comparison. Clearly then, SNe play a critical role in shaping the ISM properties. We shall look into this more quantitatively later. The vertical gas distribution of runs 5 and 6 are slightly less turbulent (compared to runs 3 and 4) since these runs employ a significantly lower C_* value.

Fig. 5.2 shows the total SFR as a function of time for our different simulation models. From Fig. 5.2 we see that model runs 1 and 5 have the lowest SFR. This is due to their low C_* value. Runs 2−4 have a global SFR varying between 0.2 and 0.4 $\rm M_\odot\ yr^{-1}$ over 1 Gyr of evolution. There are important differences between these models however. Model run 2 starts with a initially high SFR at 0.4 $\rm M_\odot yr^{-1}$ and decreases fairly consistently towards 0.2 $\rm M_\odot\ yr^{-1}$ after 1 Gyr. This is because the high star formation efficiency of this model means an initially high SFR, but as time passes and the gas reservoir from which the stars are formed quickly gets

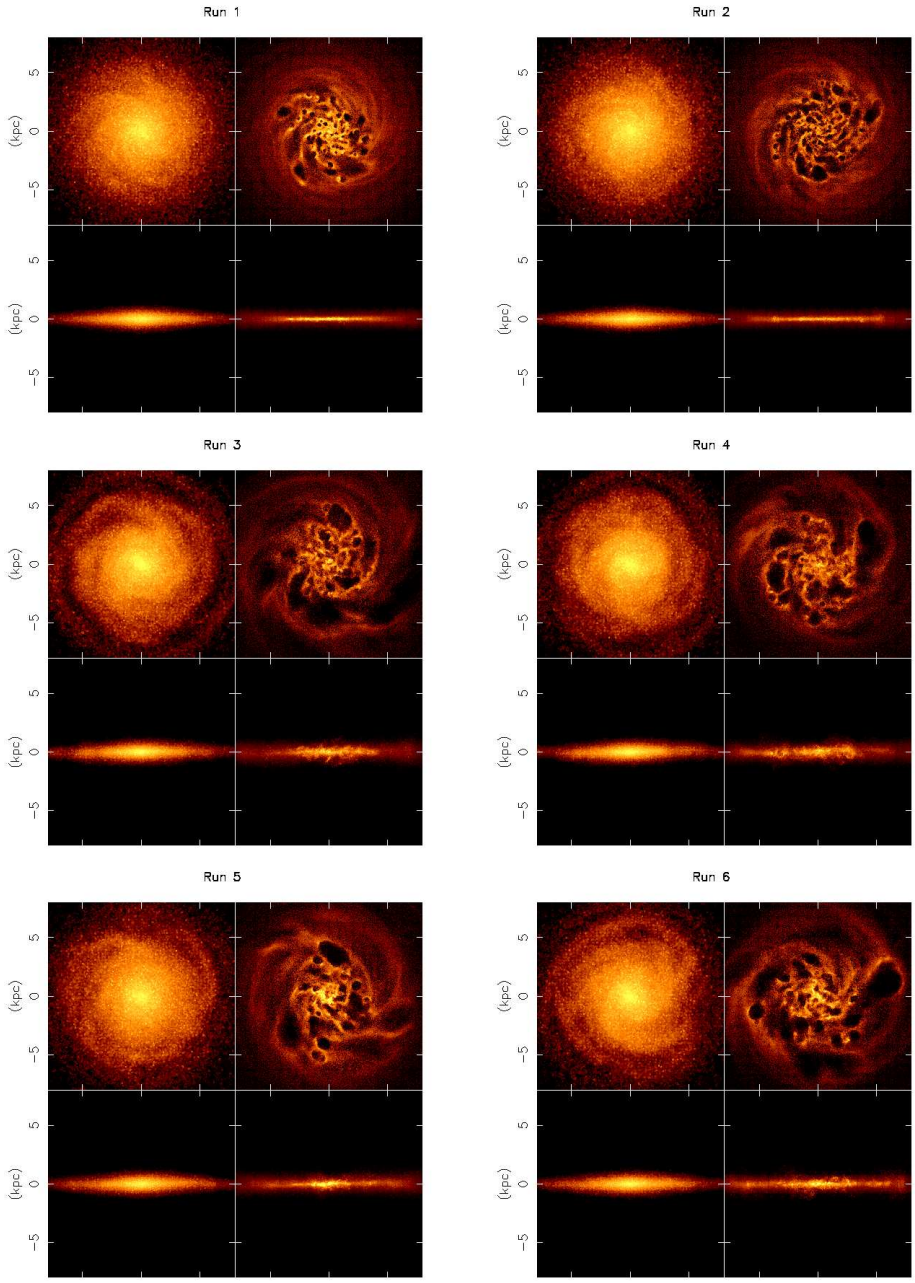

Figure 5.1: Face on (top row) and edge on (bottom row) view of the stellar (left-hand column) and gas (right-hand column) distribution for our six simulation runs at $t = 1$ Gyr when we carry out our analyses. The large holes in the gas distribution are caused by supernovae. The holes are larger in runs 3−6 since $E_{\rm SN}$ is 10 times higher in these runs compared to runs 1 and 2. Consequently, the gas discs of runs 1 and 2 are razor thin compared to runs 3−6 which have a larger vertical gas velocity dispersion.

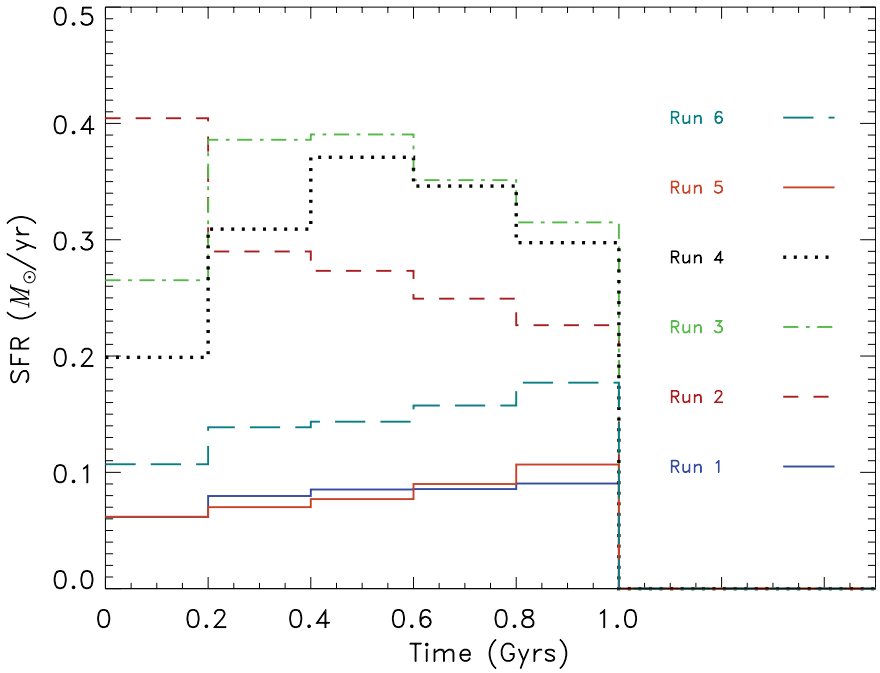

Figure 5.2: SFR history of the simulations. The solid, dashed, dot-dashed, dotted, triple dot-dashed and long-dashed lines represent runs 1, 2, 3, 4, 5 and 6 respectively.

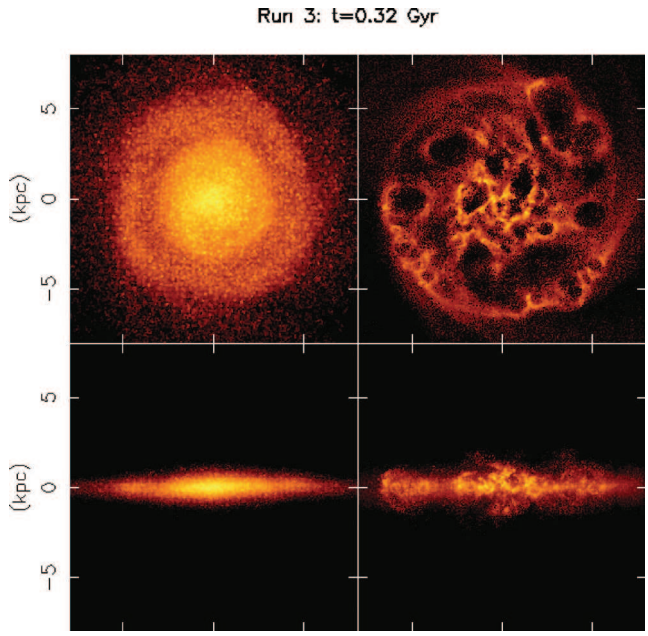

Figure 5.3: Face-on (upper) and edge-on (lower) snapshot of the galaxy at $t = 0.32$ Gyr for stars (left-hand column) and gas (right-hand column) colour coded by density for run 3. The brightest regions are the densest. Large holes or bubbles are visible in the gas distribution due to powerful SNe explosions. The large-scale vertical turbulence this causes is visible in the edge-on gas distribution.

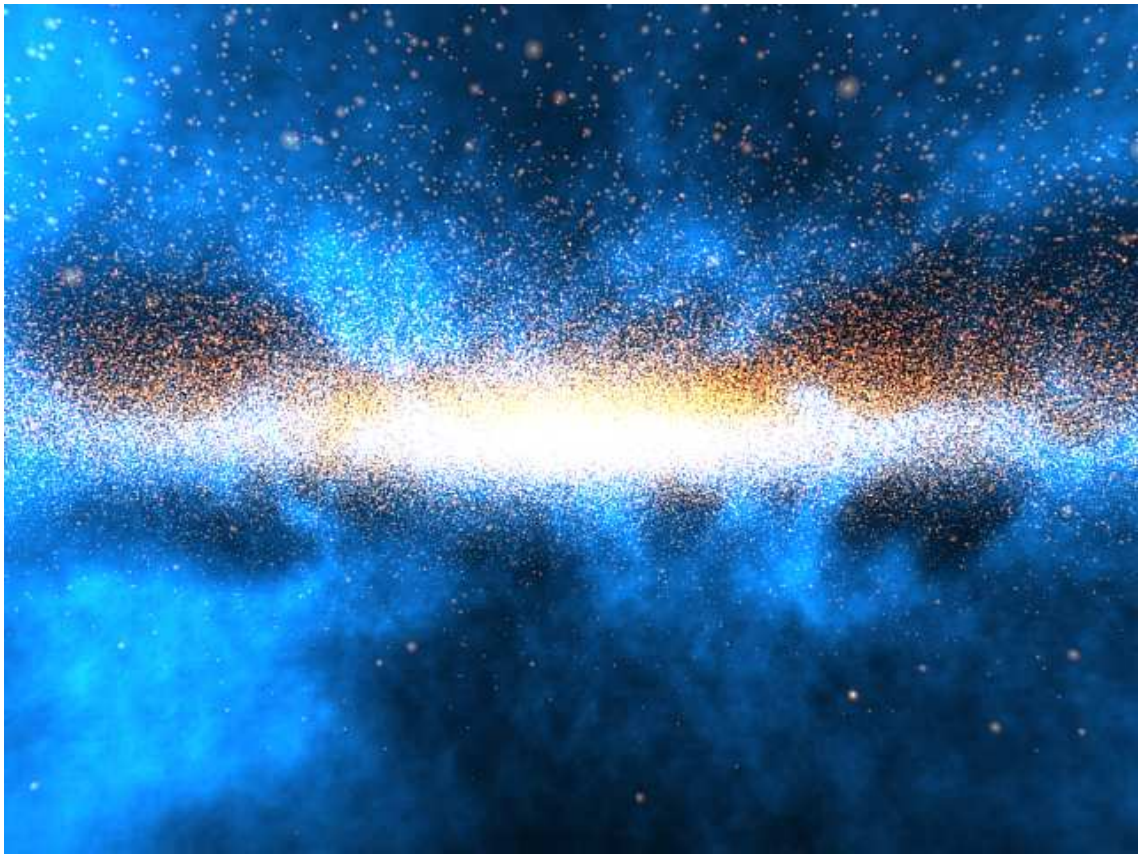

Figure 5.4: 3D perspective view of the early chaotic scenes in one of our high feedback simulations (run 4). This snapshot was taken with the observer embedded just below the plane of the disc at a radius of $\sim$ 6.5 kpc and looking toward the centre of the galaxy. The size of the field of view is 9 $\times$ 6.5 kpc at the centre of the galaxy. The yellow spheres represent the stars and the blue (diffuse) material represents the gas. The colour coding is by density, so whiter or bluer regions represent more dense conglomerations of stars and gas, respectively. The clumpy and highly inhomogeneous nature of the gas is clearly visible, as are the holes punched out by SNe. The size of the stars represents their distance from the camera. The larger stars are closer to the observer position.

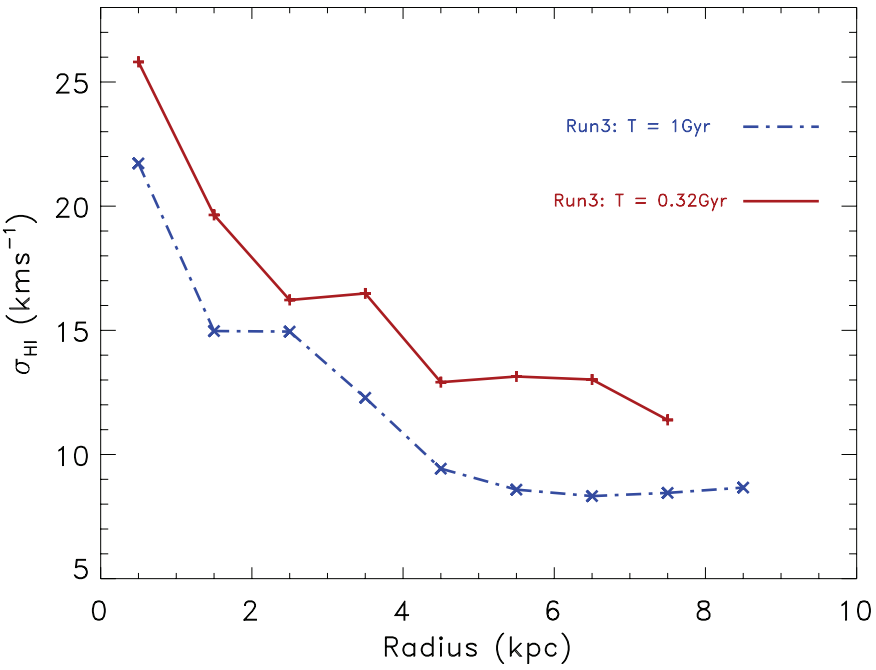

Figure 5.5: Vertical gas velocity dispersion against radius seen at two different times in the same simulation (run 3). The solid red line shows the result at an early and chaotic time, whereas the blue dot-dashed line shows the velocity dispersion at much later times. During the large bubble phase, the velocity dispersion is unrealistically high.

used up, the SFR correspondingly decreases. Runs 3 and 4 initially have a lower SFR compared to run 2. This is due to large outflows or 'bubbles' which drive out the gas at very early times. After this initial violent period the SFR increases and peaks after 0.5 Gyr at 0.4 $M_{\odot}yr^{-1}$ after which it decreases slightly to 0.3 $M_{\odot}$ yr^{-1} by 1 Gyr of evolution. This means the higher energy produced from SNe and stellar winds initially slightly suppress star formation at very early times but that more gas becomes available for later star formation. The early time suppression of star formation is slightly stronger in run 4 compared to run 3 since in this model we implement higher energy release from stellar winds as well as from SNe. Run 5 has identical feedback parameters to run 4, with the only difference being that C_* is low as in run 1. Run 5 has a similar SFR history to run 1, showing that the SFR is extremely sensitive to the star formation efficiency (C_*) as expected. Run 6 has roughly double the SFR of run 5 as expected from its higher C_* value. After approximately 0.5 Gyr, the SFR does not evolve significantly in all our simulation

runs. Before 0.5 Gyr, the ISM can be extremely turbulent, especially for the high-feedback models, as can be seen in Fig. 5.3 which shows the 2-D face-on and edge-on stellar and gas distribution at an early time (0.32 Gyr) for our high-$E_{\rm SN}$ model (run 3). At this time, many large gas outflows are seen to occur. Fig. 5.4 shows a 3-D visualisation of both the stellar and gas distributions of the galaxy at early times for run 4. The clumpy and chaotic nature of the ISM is clearly apparent at these early times, with large gas outflows and bubbles visible. Fig. 5.5 shows that during the time when a large gas outflow occurs, the velocity dispersion of the gas component (measured as described below) is correspondingly very high. At a much later time when the disc is more settled (e.g. 1 Gyr), the velocity dispersion is correspondingly lower. Note that our initial condition is not in perfect equilibrium and small transient features develop initially. Focussing on the output only at 1 Gyr safely avoids the unwanted effect from the initial conditions. On the other hand, because we do not take into account later gas accretion, and the gas is consumed by star formation, it is unrealistic to integrate the system for a long time. Therefore, 1 Gyr was chosen as a compromise and sufficiently long enough time to wait for the system to settle before carrying out our main analysis and comparison to the observations.

Fig. 5.6 shows the relation between gas and SFR surface densities for our six sample runs where we have plotted the units to be identical to the observed sample of spiral galaxies in fig. 13 of Bigiel et al. (2008). Bigiel et al. (2008) show the surface SFR density against total hydrogen surface density. Taking advantage of our self-consistent chemodynamical modelling, we analyse the hydrogen fraction for each gas particle and self-consistently show the total hydrogen surface density in Fig. 5.6, where in our notation: $\Sigma_{\rm H} = \Sigma_{\rm HI} + \Sigma_{\rm H_2}$. The results were obtained using a pixel-by-pixel methodology using a square-cell resolution of 333 pc $\times$ 333 pc and a smoothing length of two pixel box lengths. The surface SFRs are calculated using the surface densities of young stars less than 0.5 Gyr old. We only include the pixels which have at least 10 young star particles contributing to them. In Fig. 5.6, we also plot diagonal dotted lines of constant star formation efficiency (SFE), exactly

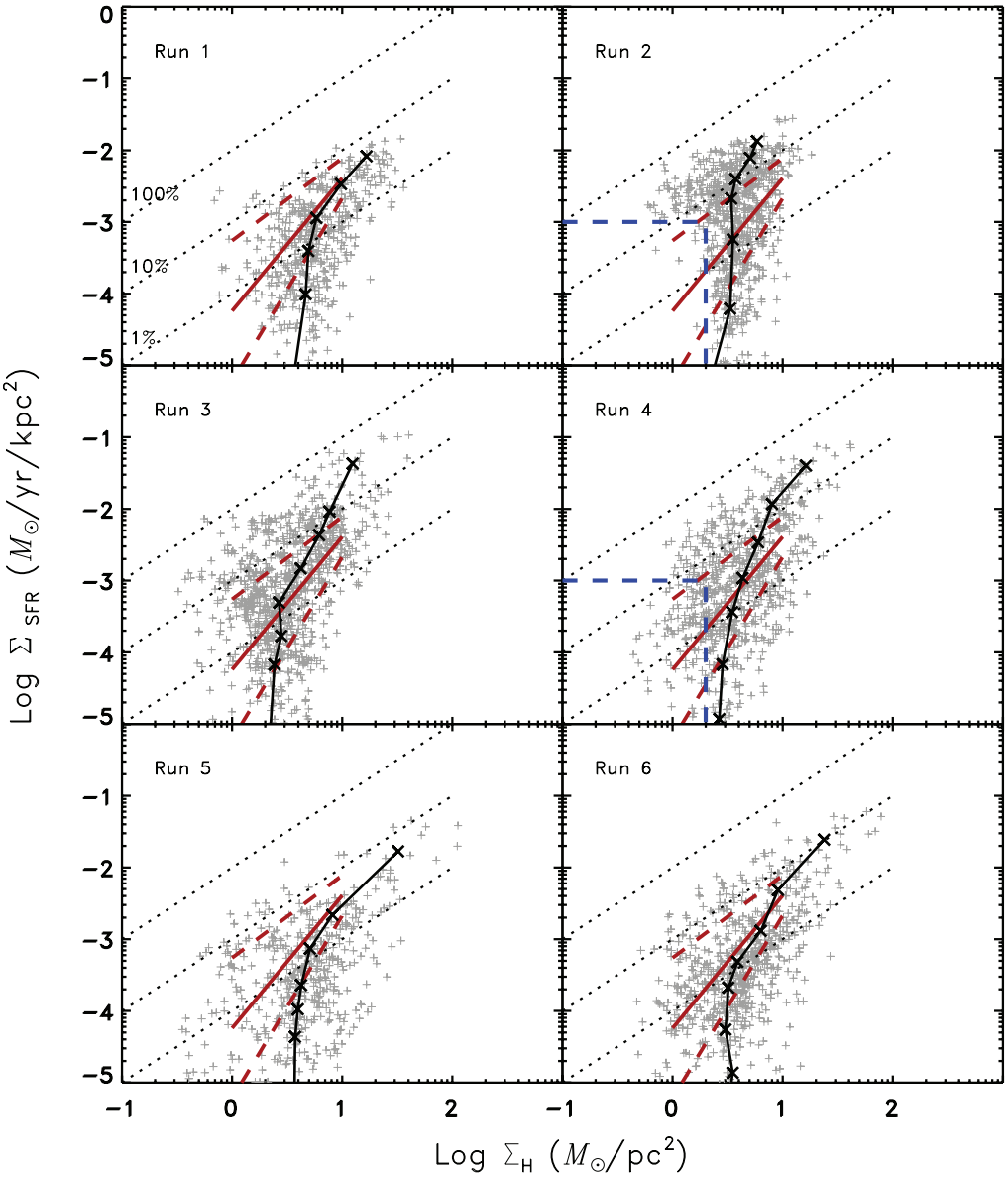

Figure 5.6: Surface SFR density as a function of surface gas density for our six models at 333 pc resolution (grey plus signs). The surface SFR densities are calculated using the surface densities of young stars less than 0.5-Gyr-old. The diagonal dotted lines represent lines of constant SFE, indicating the level of $\Sigma_{\rm SFR}$ needed to consume 1, 10 and 100 per cent of the gas reservoir in 10^8 years, exactly as in fig. 13 of Bigiel et al. (2008). Therefore, the lines also correspond to constant gas depletion times of 10^{10}, 10^9 and 10^8 years, respectively. The red solid and dashed lines represent the mean and 1σ upper and lower bounds, respectively, for the Bigiel et al. (2008) data between log $\Sigma_{\rm H}$ values of 0 and 1. The blue dashed horizontal and vertical lines in run 2 are drawn to emphasise the region of low $\Sigma_{\rm H}$ and $\Sigma_{\rm SFR}$ where there are barely any pixels present. The same region is marked in run 4 to show that this model can successfully produce regions with both low $\Sigma_{\rm H}$ and $\Sigma_{\rm SFR}$. The location of these pixels are shown in Fig. 5.7. In this figure $\Sigma_{\rm H} = \Sigma_{\rm HI} + \Sigma_{\rm H_2}$. We also overplot the results obtained using azimuthally averaged ring annuli of width 1 kpc (black crosses connected by solid lines).

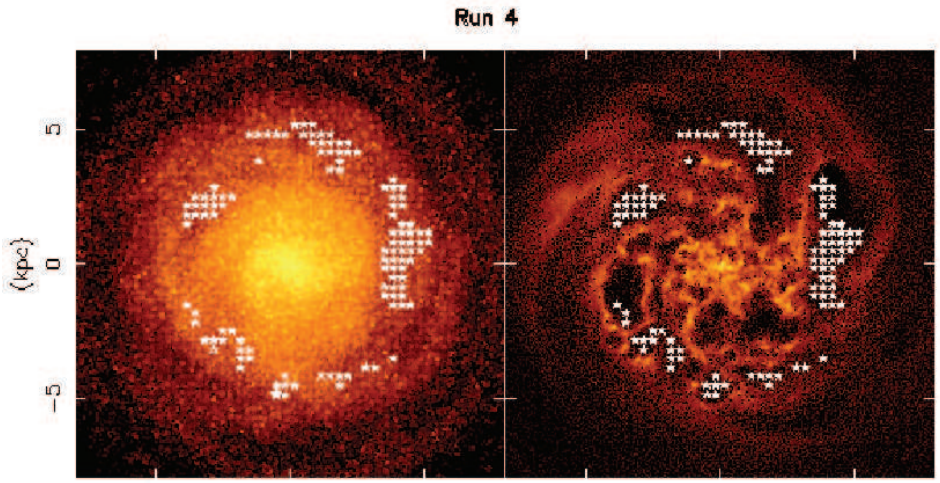

Figure 5.7: Face on view of the stellar (left) and gas (right) distribution at $t = 1$ Gyr for model run 4. The white stars represent the spatial locations of the pixels selected in run 4 of Fig. 5.6, which contain both low surface gas and SFR densities (enclosed by the dashed blue lines and the axes). We can clearly see that all of these pixels are located in bubble regions where the gas density is low.

as in Bigiel et al. (2008) in order to make the comparison easier, indicating the level of $\Sigma_{\rm SFR}$ needed to consume 1, 10 and 100 per cent of the gas reservoir in 10^8 years. We also overplot a best-fitting line (solid red line) to represent the mean values for the Bigiel et al. (2008) data between log $\Sigma_{\rm H}$ values of 0 and 1 (see e.q. 2 of Bigiel et al., 2008) and show the 1σ upper and lower bounds (dashed red lines). We can clearly see that the $\Sigma_{\rm SFR}$ for model run 1 is too low at all values of $\Sigma_{\rm H}$. This is because this simulation had a very low star formation efficiency. Increasing the SFE parameter (run 2) does increase $\Sigma_{\rm SFR}$ but at the expense of accurately following the slope of the observations. Our high-C_* model (run 2) therefore still fails to accurately follow the observed trends. The high-$E_{\rm SN}$ model (run 3) and our highest feedback model (run 4) better follow the observed slope and values for the SK law. Interestingly, the increased energy released from SNe explosions and stellar winds in these models help to increase the star formation rate at very low gas densities. The major difference between runs 2 and 4 comes from the lack of pixels with low values for both $\Sigma_{\rm H}$ and $\Sigma_{\rm SFR}$ in run 2, unlike the higher feedback models such as run 4. By selecting the pixels that fall into the bottom-left region (enclosed by the dashed

blue lines) for run 4 in Fig. 5.6, we investigated where these pixels were located and found that they predominantly lie in large holes blasted out by SNe (Fig. 5.7). This suggests that SNe may play a vital role in shaping observed SK-laws, especially at low gas densities. Run 5 also employs high feedback parameters, but with a low C_* value of 0.02 as in run 1. Correspondingly, we see that $\Sigma_{\rm SFR}$ is too low like in run 1. In run 6, we have increased the value of C_* to 0.05. This represents our best compromised model. We see that increasing C_* results in higher $\Sigma_{\rm SFR}$ values and a better fit to the observations. We note that due to the relatively low mass of our simulated galaxy, which does not have a very high SFR or contain very dense regions, we cannot inspect a wide range of $\Sigma_{\rm H}$ parameter space and are therefore limited to making our comparisons in a narrow range of $\Sigma_{\rm H}$.

In Fig. 5.6 we also overplot the results obtained using a radial ring analysis method (black crosses connected by solid lines) whereby we have calculated the values of $\Sigma_{\rm H}$ and $\Sigma_{\rm SFR}$ in azimuthally averaged ring annuli of width 1 kpc. We see that both the radial ring and pixel-by-pixel methods produce broadly consistent results, with the possible exception being that the radial ring method does not probe well the low $\Sigma_{\rm H}$ regime. Some of the data points in this regime represent ring annuli regions lying just outside the main star-forming disc of our galaxy.

In Fig. 5.8 we compare the kinetic energy density of the HI gas, $E_k = (3/2)\Sigma_{\rm HI}\sigma^2_{\rm HI}$, against the SFR surface density as in Tamburro et al. (2009). Here $\sigma_{\rm HI} = \sqrt{\sigma^2_{\rm th} + \sigma^2_{\rm t}}$ where $\sigma_{\rm th}$ and $\sigma_{\rm t}$ are the velocity dispersions due to thermal and turbulent motions, respectively. In addition, to mimic HI observations, we only take into account the gas particles whose density is in the region $0.1 < \rho_{\rm HI} < 50$ cm^{-3} and have temperature less than 10^4 K. We also use the same units for the axes and show with solid lines the supernova energy input for different SNe efficiency values, $\epsilon_{\rm SN} = 1$, 0.1 and 0.01 exactly as in Tamburro et al. (2009). Their observations show a linear correlation between E_k and $\Sigma_{\rm SFR}$, with typical $\epsilon_{\rm SN}$ values between 0.1 and 1. At higher $\Sigma_{\rm SFR}$ regimes, the E_k slightly falls off. Comparing against our simulated galaxies with their fig. 4, we see that runs 3−6 best follow the observations. Runs 1 and 2 fail

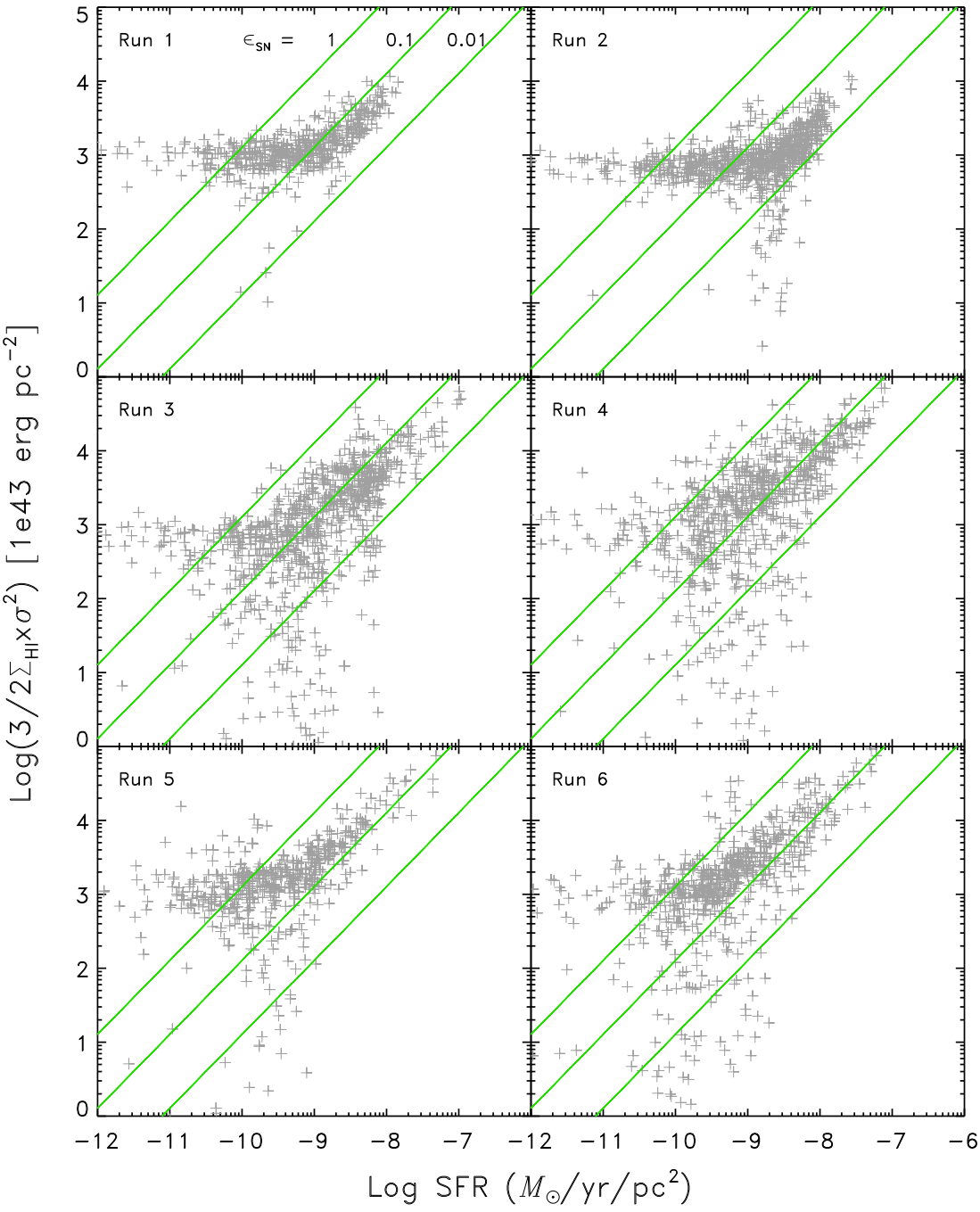

Figure 5.8: Pixel-by-pixel scatter plot of the kinetic energy versus surface star formation rate for our six model galaxy runs (grey plus signs). The solid lines of unity slope represent the supernova energy input for different supernova efficiency values, $\epsilon_{\rm SN} = 1, 0.1, 0.01$ (top to bottom).

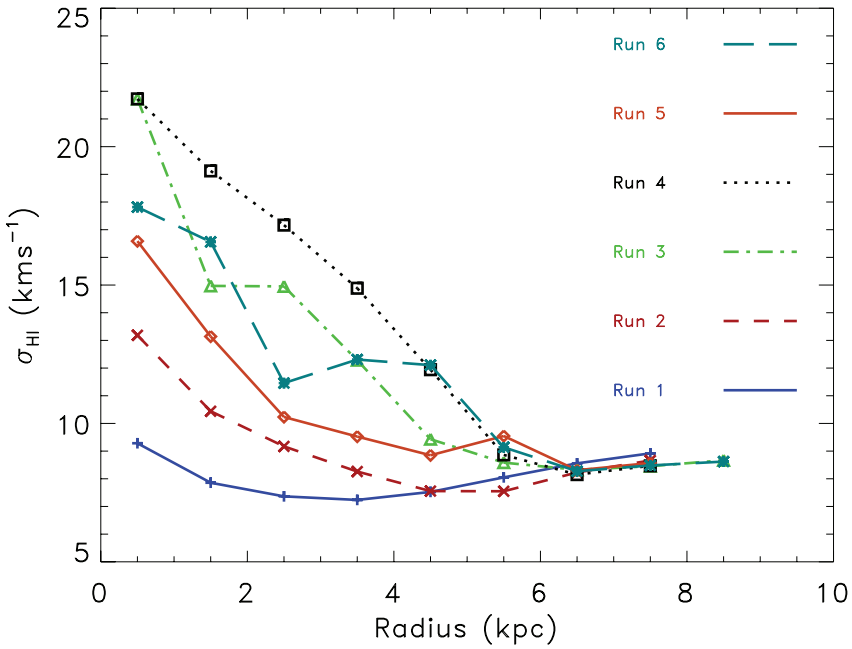

Figure 5.9: Gas velocity dispersion versus radius for our six models. The 'higher-feedback' with high-C_* models (runs 3 and 4) has larger velocity dispersion. Our results show that the velocity dispersion is primarily sensitive to our SNe energy ($E_{\rm SN}$) parameter.

to capture the observed trends, especially, E_k is lower at $-9.5 < \mathrm{Log}\,\Sigma_{\rm SFR} < -8.5$ compared to fig. 4 of Tamburro et al. (2009).

We also analysed the azimuthally averaged radial profile for the HI velocity dispersion, by calculating the average value of $\sigma_{\rm HI}$ (following the same method as above) within ring annuli of radial width 1 kpc. Observations of spiral galaxies show a radial decline for the HI velocity dispersion with a value of $\sim$ 20 km s^{-1} in the inner region, declining to $\sim$ 10 km s^{-1} by r_{25} (Tamburro et al., 2009). Fig. 5.9 shows that our higher feedback models (runs 3 and 4) closely follow the aforementioned observed trends. All of our models had similar $\sigma_{\rm HI}$ values of around 10 km s^{-1} by r_{25} similar to what was found in Tamburro et al. (2009). With the exception of run 1, all models showed a radial decline of $\sigma_{\rm HI}$. The decline was small for our high-C_* model (run 2) and more noticeable for our higher feedback models (runs 3 and 4). This is understandable since the higher feedback models produce larger gas outflows and bubbles which increases $\sigma_{\rm HI}$. Interestingly, our model with high $E_{\rm SN}$

and $E_{\rm SW}$ (run 4) did not have a noticeable difference with our high-$E_{\rm SN}$ model (run 3), proving that it is the supernova energy which mainly drives the turbulence in the ISM in our models. Further evidence of this lies in the comparison of the velocity dispersion of runs 1 and 5, with run 5 having a noticeably larger $\sigma_{\rm HI}$. Despite this, $\sigma_{\rm HI}$ for run 5 is still too low compared with observations of Tamburro et al. (2009). Therefore in run 6, we slightly increased the value of C_* and found that $\sigma_{\rm HI}$ also increased to a level which is consistent with the observations.

5.4 Summary and Conclusions

We aim to build the most accurate and self-consistent numerical model for late-type spiral galaxies to date. To this end, we have been developing our numerical simulation code `GCD+`. We include new star formation and feedback recipes which allow our simulations to follow the effects of powerful SNe explosions on galaxy evolution.

In this study, we set up an isolated M33-sized disc galaxy consisting of gas and stellar discs with no bulge component, in a static dark matter halo gravitational potential. We carried out six main simulation runs in which we varied three of our model parameters; the star formation efficiency (C_*), the thermal energy released per SNe explosion ($E_{\rm SN}$) and the thermal energy released per unit time from stellar winds ($E_{\rm SW}$). We studied the effect of varying these parameters on the SK Law and vertical gas velocity dispersion versus radius relation comparing to observations from Bigiel et al. (2008) and Tamburro et al. (2009), respectively. We find that our models with higher energy feedback (runs 3−6) more closely resemble the observations. Powerful supernova explosions cause the formation of large holes or bubbles in the gas distribution in the galaxy and stir the ISM turbulence and are thus essential for producing the observed gas velocity dispersions. The gas velocity dispersion is also affected (albeit less strongly) by the star formation efficiency. Our model with high energy feedback from SNe and stellar winds and intermediate star formation

efficiency (run 6) most closely resembled the observations. This run represented our 'best compromised model' since we had fine-tuned the star formation efficiency and feedback parameters. In our pixel-by-pixel analysis of the star formation law, we found that our model with high star formation efficiency and low energy feedback (run 2) produced a SK relation with an unrealistically steep slope. Models with low energy feedback had a distinct lack of pixels with both low $\Sigma_{\rm H}$ and $\Sigma_{\rm SFR}$, resulting in a failure to accurately reproduce the observed star formation law. By increasing the energy feedback parameters, $E_{\rm SN}$ and $E_{\rm SW}$ (as in run 4) we managed to rectify this problem and found that the pixels which had low values for both $\Sigma_{\rm H}$ and $\Sigma_{\rm SFR}$ were predominantly located inside bubble regions, which were more numerous and larger in size for the higher feedback runs. Our results therefore suggest that SNe can play a pivotal role in shaping the star formation law. We used both a pixel-by-pixel and radial ring method to analyse the star formation law in our galaxies and found that overall, both methods gave broadly consistent results.

In this chapter, we employed static potentials for the dark matter halo and stellar disc. The main benefits of not using a live halo include the prevention of numerical effects such as artificial disc heating due to the scattering of baryonic particles by more massive dark matter particles which may be an issue in lower resolution cosmological simulations. Our numerical simulations thus do not suffer from these global disc instabilities. However, we underestimate the perturbation from accreting satellites (e.g. Purcell et al., 2011) and globular clusters (e.g. Vande Putte et al., 2009).

In this chapter, we demonstrate that reproducing both the SK relation and the observed gas velocity dispersions puts stronger constraints on the sub-grid modelling for galaxy evolution simulations. Encouraged by the success of this work, we are currently in the process of running higher resolution simulations. This should result in us being able to probe deeper into the origins of the $\Sigma_{\rm GAS}-\Sigma_{\rm SFR}$ relation. It should also mean that higher resolution models will be less sensitive than what is shown in this chapter to the employed value of the star formation efficiency, if we can

reach high enough resolution to resolve molecular cloud formation processes (Saitoh et al., 2008). At such higher resolutions, we can adopt higher star formation density thresholds, and we may need less supernovae feedback energy to reproduce the observations (e.g. Governato et al., 2010). As discussed previously, our lower resolution cosmological simulations of Chapters 3 and 4 suffer from overcooling problems. The new feedback scheme employed in this chapter coupled with much higher resolution can address these issues. After calibrating our code at this higher resolution, we then aim to run new extremely high-resolution cosmological simulations. The fully self-consistent nature of the new higher resolution cosmological simulation will be a powerful tool to unravel the mysteries behind the formation and evolution of late-type spiral galaxies like M33.

Chapter 6

Conclusions and Future Directions

Our current best theory of cosmology, the Λ cold dark matter (ΛCDM) model, is fantastically successful in explaining the large-scale structure of our Universe. Its power lies in its ability to make predictions about the present-day Universe that we live in: including its structure and content. Recently, several important cosmological surveys have taken place. These include observations of the cosmic microwave background radiation, distant Type Ia supernovae and Baryon Acoustic Oscillations. Indeed, the 2011 Nobel Prize in physics was awarded 'for the discovery of the accelerating expansion of the Universe through observations of distant supernovae'. As a result of these various recent observational campaigns, today we are living in an era of 'precision cosmology'. We now know that we live in a flat and accelerating Universe, composed primarily of dark energy and dark matter with only $\sim$4.5% of the mass-energy budget of the Universe composed of visible baryonic matter. Despite the spectacular achievements of this model, there remain a lot of unanswered questions, especially at smaller scales. Perhaps one of the most important is the formation and evolution of the individual galaxies and the outstanding issues remaining in this field, for example pertaining to observations of dark matter on galactic scales. At these scales, the relatively minor $\sim$4.5% baryonic material may play a very significant role. We therefore must include the baryonic processes in our galactic models. This leads to a large increase in the level of complexity of

the models. These baryonic processes are perhaps nowhere more important than in spiral galaxies, which are the sites of ongoing star formation and contain a large mass of gaseous material in different phases. Therefore, throughout this thesis, the formation and evolution of spiral galaxies has been studied by the use of chemo-dynamical simulations, to investigate how these objects formed and subsequently evolved.

Prior to surveying future work, a very brief summary of the key results of this thesis are presented:

- *Disc bulge stars*: The kinematics and chemistry of stars found in the bulge of two simulated spiral galaxies were analysed. These stars are either born *in situ* or are accreted via multiple mergers early in the history of the galaxies. The signature of their accretion is their high total energy. Stars formed during mergers at different epochs show different [α/Fe]. Additionally, we established that ancient orbital information may still be preserved in the present day kinematics of bulge stars.

- *Abundance gradients in the disc*: The radial abundance gradients along the disc of a simulated galaxy were analysed and compared with recent observations from the Milky Way. It was found that the simulated disc contained a greater fraction of young stars in the outer regions, with more old stars in the inner regions. This could explain the positive [α/Fe] and negative [N/O] gradients with radius. These radial trends were a natural outcome of an inside-out formation of the disc and thus could explain the recently observed positive [α/Fe] gradients seen in Milky Way disc open clusters.

- *Simulations of late-type spirals using updated* `GCD+`: Several isolated galaxy evolution simulations were carried out using the new and improved version of our N-body/SPH code `GCD+`, allowing more accurate modelling of the stellar and gaseous components of the system including powerful supernovae feedback. It was found that our models with higher energy feedback from supernovae

and stellar winds more closely resembled the observations of spiral galaxies.

Several important issues have emerged as a result of the studies carried out in this thesis which are worth mentioning in a little more detail. These include the need for:

- Creating a virtual *Gaia* catalogue.
- Higher resolution simulations.
- Improved modelling.

The European Space Agency's (ESA's) future *Gaia* mission will revolutionise galactic astronomy by providing exquisite kinematic data on up to 1 billion stars in the Milky Way. *Gaia*, in tandem with future and ongoing ground-based spectroscopic surveys such as RAVE, SEGUE, LAMOST, APOGEE, HERMES and the Gaia-ESO survey will also provide radial velocity and chemical information for faint stars. One way to prepare for this era is to build a virtual *Gaia* catalog. By carrying out as many chemodynamical cosmological simulations of Milky Way-like galaxies as possible, when the *Gaia* data becomes available, we can compare it against all of our model galaxies data to see which fits best. Since we can easily find out the past formation mechanism for the galaxies in our simulations, we will thus be able to deduce the most likely formation scenario for our own Milky Way.

In the studies carried out in this thesis, each star particle has a mass ranging from $\sim 10^4 - 10^6$ $M_\odot$, meaning that each star particle can be thought of as representing at best 10000 Suns, or a star cluster. We are however, on some level at least, comparing this cluster with individual stars. This is obviously an unsatisfactory situation. Much of the important processes involved in galaxy formation and evolution (such as star formation) occurs on scales below the resolution of the current simulations and so must be modelled in a phenomenological manner. The particle mass used in the current state-of-the-art Milky Way sized cosmological simulations is $\sim 10^4$ $M_\odot$. Perhaps the next immediate target is resolving down to the scale of star

forming molecular clouds with $100-1000$ $M_\odot$ particles. In the future, as computing power continues to increase, this situation will be remedied until eventually each star particle in the numerical simulation will have the same mass as the stars that they are supposed to be representing in nature. This achievement may not be too far away for a galaxy the size of our Milky Way. We may reach it anywhere in the next $15-50$ years. Soon afterwards, it may be possible to model other smaller bodies such as planets. This process may continue to even smaller scales. Indeed it is permissible to envision a day when the whole Universe can be simulated on an atom-by-atom basis using quantum computing or some other future technology. Resolving down to such fine scales will be a serious challenge in galaxy formation simulations, because the dynamical range of the system is huge and the timescales of the physical processes being modelled are vastly different. More efficient parallelisation will be extremely demanding, and is a significant problem that we are currently facing. Therefore, just as important as improvements in computer hardware are improvements in software and algorithms. For example, the introduction of tree codes such as the algorithm of Barnes & Hut (1986) represented a paradigm shift, allowing us to do the kinds of cosmological simulations that we are familiar with today, as presented in Chapters 4 and 5 of this thesis. Some groups (e.g. Okamoto et al., 2010; Brook et al., 2011, 2012; Governato et al., 2012) have recently claimed that the remaining outstanding problems of the ΛCDM model; namely, the angular momentum catastrophe, the missing satellites problem and the core-cusp problem, can all be resolved (without needing to look beyond the CDM model) by altering the feedback amount and implementation in simulations. This demonstrates the power and need for better and more accurate modelling. Currently, our code is not utilising the full capabilities of the state-of-the-art supercomputers. In the future, it is vitally important to continue work on improving our numerical simulation codes as progress in this field is reliant on advances in both software and hardware.

Other exciting, more speculative future studies

With the newly improved modelling of supernovae and metal enrichment, it is possible to carry out other more extravagant studies with our updated galactic chemodynamical software package. One possibility is a theoretical study in the field of Galactic Astrobiology. With the discovery of thousands of new extra-solar planets and an increasing number of 'earth-like' planets in the past few years, this is a very topical subject and will only become more important with time. One of the major aims of Astrobiology is to find habitable planets outside of our solar system in the Galaxy. There has already been theoretical interest in linking habitability of a planet with the larger scale Galactic environment in which it resides, the so called 'Galactic Habitable zone' (e.g. Lineweaver et al., 2004). This idea assumes that there exists a region or regions in our Galaxy which have favourable environmental conditions which can support the development of life. It therefore also assumes that there must exist regions where life cannot develop. For example, avoiding the spiral arms is thought to be crucial for the development of life. A planetary system transiting the spiral arms would receive intense radiation and gravitational disruption. Furthermore spiral arms are host to many massive young stars. This makes them the top candidate for hosting massive Type II supernovae.

It is believed that supernovae explosions constitute the most dangerous threat to the development of life in a galaxy. Their frequency, with one estimated to go off every 50 years in our Milky Way, indicates that they are relatively common events. Luckily for us, all recorded supernovae in recent human history have occurred at sufficiently far away distances in our Galaxy as not to affect the biosphere of the Earth. However, going back further in time, this may not always have been the case. There is evidence that periodic mass extinctions occurring on timescales of tens or hundreds of millions of years on Earth may have been caused by nearby supernovae events (e.g. Melott et al., 2004).

It therefore seems that the habitability of a planetary system in a galaxy is

strongly dependent on its orbit around the centre, with ideal orbits missing or minimising the time spent crossing the potentially lethal supernovae rich spiral arms. Luckily our solar system's orbital speed around the Galactic centre is thought to be similar to the pattern speed of the local spiral arms, and so it is suggested that we do not cross spiral arms too often. It has also been suggested that circular stellar orbits around the Galaxy are favourable to elliptic orbits as a more elliptic orbit may increase the chances of crossing spiral arms. The majority of stars in the Galaxy may not be able to support habitable planets simply because their rotation is not synchronised with the rotation of the Galaxy's spiral arms. Orbital path is hence hypothesised to be extremely important for habitability. However, as of yet, these are all still hypotheses.

It would therefore be very interesting to apply *as a first step* our well calibrated Galactic model to do an actual statistical study of 'Galactic Habitable Orbits'. The past orbit of star particles ending up around the solar radius could be traced to see which kind of orbits are the 'safest' for the development of life, assuming that close proximity to any supernova during the orbit can lead to a danger of extinction. The supernovae rate of the neighbouring particles should depend on the orbit itself and the proximity to star forming regions, for example how often they pass through the spiral arms and therefore the pattern speed of the spiral arms. Recent studies suggest that spiral arms are transient and co-rotating features (e.g. Grand et al., 2012). If this theory is true, stars near spiral arms migrate radially and spend more time close to the arm. This may present a greater danger for the development of life. Therefore, Galactic Habitable Orbits should also be sensitive to the theory of the spiral arms. This proposed future study may provide a new venue to tackle the theory of spiral arms. Similarly, radial migration (e.g. Sellwood & Binney, 2002; Roŝkar et al., 2008) may also have a strong effect on habitability and so this work would also simultaneously be addressing other important topics of Galactic astronomy.

In the near future, ESA's cornerstone mission, *Gaia*, will map the position and

velocity of about 1 billion disc stars. By comparing the current phase space position of the 'safest' orbit from the simulation prediction with this observational data, it may become possible to identify the safest stars in the *Gaia* data. These stars could then become an interesting target for the future planet finding satellite missions and ground-based survey campaigns. If planets orbiting such stars are found, they would become a prime target for follow-up observations with 30 m class telescopes, i.e. direct spectroscopy of these planets, with the aim being to find any possible signs of life. The study of Galactic Habitable Orbits would be unique in both the subject and methodology, and would be an excellent application and demonstration of the capabilities of galaxy simulations for multi-disciplinary studies.

Closing Remarks

We are currently living in a golden age of Astronomy. The next decade will be an extremely fascinating time. *Gaia*, *Euclid*, *James Webb Space Telescope* (JWST), *Square Kilometre Array* (SKA) and the *European Extremely Large Telescope* (E-ELT) are just some of the new missions that will each revolutionise astronomy in their own right. Indeed innovative solutions need to be invented just to store the vast quantity of raw data that will soon become available with processing and mining the data posing another substantial computational challenge. Theoretical models will then play a crucial role in interpreting and unravelling the implication and significance of the data. This will ensure that theoretical modelling such as the chemodynamical numerical simulations employed in this thesis, will continue to play a crucial role in the future.

Bibliography

Aarseth S. J., 1963, MNRAS, 126, 223

Abadi M. G., Navarro J. F., Steinmetz M., Eke V. R., 2003a, ApJ, 591, 499

Abadi M. G., Navarro J. F., Steinmetz M., Eke V. R., 2003b, ApJ, 597, 21

Agertz O., Lake G., Teyssier R., Moore B., Mayer L., Romeo A. B., 2009, MNRAS, 392, 294

Agertz O., Moore B., Stadel J., Potter D., Miniati F., Read J., Mayer L., Gawryszczak A., Kravtsov A., Nordlund ., Pearce F., Quilis V., Rudd D., Springel V., Stone J., Tasker E., Teyssier R., Wadsley J., Walder R., 2007, MNRAS, 380, 963

Allende Prieto C., Majewski S. R., Schiavon R., Cunha K., Frinchaboy P., Holtzman J., Johnston K., Shetrone M., Skrutskie M., Smith V., Wilson J., 2008, ApJ, 329, 1018

Andrievsky S. M., Luck R. E., Martin P., Lepiné J. R. D., 2004, A&A, 413, 159

Astier P., Guy J., Regnault N., Pain R., Aubourg E., Balam D., Basa S., Carlberg R. G., Fabbro S., Fouchez D., Hook I. M., Howell D. A., Lafoux H., Neill J. D., Palanque-Delabrouille N., Perrett K., Pritchet C. J., Rich J., Sullivan M., Taillet R., Aldering G., Antilogus P., Arsenijevic V., Balland C., Baumont S., Bronder J., Coutois H., Ellis R. S., Filiol M., Goncalves A. C., Goobar A., Guide D., Hardin

D., Lusset V., Lidman C., McMahon R., Mouchet M., Mourao A., Perlmutter S., Ripoche P., Tao C., Walton N., 2006, A&A, 447, 31

Aumer M., Binney J. J., 2009, MNRAS, 397, 1286

Babusiaux C., Gilmore G., 2005, MNRAS, 358, 1309

Bailin J., Kawata D., Gibson B. K., Steinmetz M., Navarro J. F., Brook C. B., Gill S. P. D., Ibata R. A., Knebe A., Lewis G. F., Okamoto T., 2005, ApJ, 627, L17

Barnes J., Hut P., 1986, Nature, 324, 446

Batalha N. M., Rowe J. F., Bryson S. T., Barclay T., Burke C. J., Caldwell D. A., Christiansen J. L., Mullally F., Thompson S. E., Brown T. M., Dupree A. K., Fabrycky D. C., Ford E. B., Fortney J. J., Gilliland R. L., Isaacson H., Latham D. W., Marcy G. W., Quinn S., Ragozzine D., Shporer A., Borucki W. J., Ciardi D. R., Gautier T. N. I., Haas M. R., Jenkins J. M., Koch D. G., Lissauer J. J., Rapin W., Basri G. S., Boss A. P., Buchhave L. A., Charbonneau D., Christensen-Dalsgaard J., Clarke B. D., Cochran W. D., Demory B., Devore E., Esquerdo G. A., Everett M., Fressin F., Geary J. C., Girouard F. R., Gould A., Hall J. R., Holman M. J., Howard A. W., Howell S. B., Ibrahim K. A., Kinemuchi K., Kjeldsen H., Klaus T. C., Li J., Lucas P. W., Morris R. L., Prsa A., Quintana E., Sanderfer D. T., Sasselov D., Seader S. E., Smith J. C., Steffen J. H., Still M., Stumpe M. C., Tarter J. C., Tenenbaum P., Torres G., Twicken J. D., Uddin K., Van Cleve J., Walkowicz L., Welsh W. F., 2012, ArXiv e-prints: 1202.5852

Bate M. R., Burkert A., 1997, MNRAS, 288, 1060

Bekki K., Chiba M., 2000, ApJ, 534, L89

Belokurov V., Evans N. W., Irwin M. J., Hewett P. C., Wilkinson M. I., 2006, ApJ, 637, L29

Belokurov V., Evans N. W., Irwin M. J., Lynden-Bell D., Yanny B., Vidrih S., Gilmore G., Seabroke G., Zucker D. B., Wilkinson M. I., Hewett P. C., Bramich D. M., Fellhauer M., Newberg H. J., Wyse R. F. G., Beers T. C., Bell E. F., Barentine J. C., Brinkmann J., Cole N., Pan K., York D. G., 2007, ApJ, 658, 337

Bensby T., Alves-Brito A., Oey M. S., Yong D., Melendéz J., 2010, A&A, 516, L13

Bensby T., Feltzing S., Lundström I., 2004, A&A, 421, 969

Bensby T., Feltzing S., Lundström I., Ilyin I., 2005, A&A, 433, 185

Berczik P., 1999, A&A, 348, 371

Bernkopf J., Fuhrmann K., 2006, MNRAS, 369, 673

Bertelli G., Nasi E., 2001, AJ, 121, 1013

Bertschinger E., 2001, ApJS, 137, 1

Bigiel F., Leroy A., Walter F., Brinks E., de Blok W. J. G., Madore B., Thornley M. D., 2008, AJ, 136, 2846

Binney J., Gerhard O., Spergel D., 1997, MNRAS, 288, 365

Binney J., Gerhard O. E., Stark A. A., Bally J., Uchida K. I., 1991, MNRAS, 252, 210

Bissantz N., Englmaier P., Gerhard O., 2003, MNRAS, 340, 949

Blitz L., Spergel D. N., 1991, ApJ, 379, 631

Booth C. M., Theuns T., Okamoto T., 2007, MNRAS, 376, 1588

Bovy J., Rix H., David W., 2012, ApJ, 751, 131

Bower R. G., Benson A. J., Crain R. A., 2012, MNRAS, 422, 2860

Bregman J. N., 1980, ApJ, 236, 577

Brook C. B., Gibson B. K., Martel H., Kawata D., 2005, ApJ, 630, 298

Brook C. B., Governato F., Rôskar R., Stinson G., Brooks A. M., Quinn T., Gibson B. K., Snaith O., Pilkington K., House E., Pontzen A., 2011, MNRAS, 415, 1051

Brook C. B., Kawata D., Gibson B. K., Flynn C., 2003, ApJ, 585, L125

Brook C. B., Kawata D., Gibson B. K., Flynn C., 2004a, MNRAS, 349, 52

Brook C. B., Kawata D., Gibson B. K., Freeman K. C., 2004b, ApJ, 612, 894

Brook C. B., Stinson G., Gibson B. K., Rôskar R., Wadsley J., Quinn T., 2012, MNRAS, 419, 771

Brooks A. M., Governato F., Booth C. M., Willman B., Gardner J. P., Wadsley J., Stinson G., Quinn T., 2007, ApJ, 655, L17

Bruzual G., Charlot S., 2003, MNRAS, 344, 1000

Carlberg R. G., 1984, ApJ, 286, 403

Carney B. W., Latham D. W., Laird J. B., Aguilar L. A., 1994, AJ, 107, 2240

Carollo D., Beers T. C., Lee Y. S., Chiba M., Norris J. E., Wilhelm R., Sivarani T., Marsteller B., Munn J. A., Bailer-Jones C. A. L., Re Fiorentin P., York D. G., 2007, Nature, 450, 1020

Cassan A., Kubas D., Beaulieu J. P., Dominik M., Horne K., Greenhill J., Wambsganss J., Menzies J., Williams A., Jørgensen U. G., Udalski A., Bennett D. P., Albrow M. D., Batista V., Brillant S., Caldwell J. A. R., Cole A., Coutures C., Cook K. H., Dieters S., Prester D. D., Donatowicz J., Fouqué P., Hill K., Kains N., Kane S., Marquette J. B., Martin R., Pollard K. R., Sahu K. C., Vinter C., Warren D., Watson B., Zub M., Sumi T., Szymański M. K., Kubiak M., Poleski R., Soszynski I., Ulaczyk K., Pietrzyński G., Wyrzykowski Ł., 2012, Nature, 481, 167

Cattaneo A., Blaizot J., Weinberg D. H., Kereš D., Colombi S., Davé R., Devriendt J., Guiderdoni B., Katz N., 2007, MNRAS, 377, 63

Chen L., Hou J. L., Wang J. J., 2003, AJ, 125, 1397

Chiappini C., Matteucci F., Gratton R., 1997, ApJ, 477, p.765

Chiappini C., Matteucci F., Romano D., 2001, ApJ, 554, 1044

Cioni M. R. L., 2009, A&A, 506, 1137

Cole S., Aragon-Salamanca A., Frenk C. S., Navarro J. F., Zepf S. E., 1994, MNRAS, 271, 781

Cole S., Lacey C. G., Baugh C. M., Frenk C. S., 2000, MNRAS, 319, 168

Combes F., Debbasch F., Friedli D., Pfenniger D., 1990, A&A, 233, 82

Connors T. W., Kawata D., Bailin J., Tumlinson J., Gibson B. K., 2006, ApJ, 646, L53

Croton D. J., Springel V., White S. D. M., De Lucia G., Frenk C. S., Gao L., Jenkins A., Kauffmann G., Navarro J. F., Yoshida N., 2006, MNRAS, 365, 11

Daflon S., Cunha K., 2004, ApJ, 617, 1115

Dalcanton J. J., Bernstein R. A., 2002, AJ, 124, 1328

de Blok W. J. G., 2010, Advances in Astronomy, id. 789293

De Lucia G., Boylan-Kolchin M., Benson A. J., Fontanot F., Monaco P., 2010, MNRAS, 406, 1533

de Vaucouleurs G., 1964, IAU Symp. 20, 195

Dib S., Bell E., Burkert A., 2006, ApJ, 638, 797

Diemand J., Zemp M., Moore B., Stadel J., Carollo C. M., 2005, MNRAS, 364, 665

Dobbs C. L., Burkert A., Pringle J. E., 2011, MNRAS, 417, 1318

Dubinski J., 1996, New Astronomy, 1, 133

Dubinski J., Carlberg R. G., 1991, ApJ, 378, 496

Durier F., Dalla Vecchia C., 2012, MNRAS, 419, 465

Eisenstein D. J., Seo H., Sirko E., Spergel D. N., 2007, ApJ, 664, 675

Esteban C., Bresolin F., Peimbert M., García-Rojas J. and. Peimbert A., Mesa-Delgado A., 2009, ApJ, 700, 654

Esteban C., García-Rojas J., Peimbert M., Peimbert A., Ruiz M. T., Rodríguez M., Carigi L., 2005, ApJ, 618, L95

Feltzing S., Bensby T., Lundström I., 2003, A&A, 397, L1

Ferland G. J., Korista K. T., Verner D. A., Ferguson J. W., Kingdon J. B., Verner E. M., 1998, PASP, 110, 761

Ferreras I., Wyse R. F. G., Silk J., 2003, MNRAS, 345, 1381

Font A. S., Johnston K. V., Bullock J. S., Robertson B. E., 2006, ApJ, 646, 886

Frebel A., Aoki W., Christlieb N., Ando H., Asplund M., Barklem P. S., Beers T. C., Eriksson K., Fechner C., Fujimoto M. Y., Honda S., Kajino T., Minezaki T., Nomoto K., Norris J. E., Ryan S. G., Takada-Hidai M., Tsangarides S., Yoshii Y., 2005, Nature, 434, 871

Freeman K., Bland-Hawthorn J., 2008, Astronomical Society of the Pacific Conference Series, 399, p.439

Freeman K. C., 1970, ApJ, 160, 811

Friel E. D., Janes K. A., Tavarez M., Scott J., Katsanis R., Lotz J., Hong L., Miller N., 2002, AJ, 124, 2693

Fuhrmann K., 1998, A&A, 338, 161

Fuhrmann K., 2008, MNRAS, 384, 173

Fulbright J. P., McWilliam A., Rich M. R., 2006, ApJ, 636, 821

Fux R., 1999, A&A, 345, 787

Gibson B. K., 1994, MNRAS, 271, 35

Gibson B. K., 1997, MNRAS, 290, 471

Gibson B. K., Loewenstein M., Mushotzky R. F., 1997, MNRAS, 290, 623

Gillessen S., Eisenhauer F., Trippe S., Genzel R., Martins F., Ott T., 2009, ApJ, 692, 1075

Gilmore G., Reid N., 1983, MNRAS, 202, 1025

Gingold R. A., Monaghan J. J., 1977, MNRAS, 181, 375

Gonzalez O. A., Rejkuba M., Minniti D., Zoccali M., Valenti E., Saito R. K., 2011, A&A, 534, L14

Gouda N., Kobayashi Y., Yamada Y., Yano T., Tsujimoto T., Suganuma M., Niwa Y., Yamauchi M., Kawakatsu Y., Matsuhara H., Moda A., Tsuiki A., Utashima M., Ogawa A., Sako N., 2006, Exploiting Large Surveys for Galactic Astronomy, 26th meeting of the IAU, Joint Discussion 13

Governato F., Brook C., Mayer L., Brooks A., Rhee G., Wadsley J., Jonsson P., Willman B., Stinson G., Quinn T., Madau P., 2010, Nature, 463, 203

Governato F., Willman B., Mayer L., Brooks A., Stinson G., Valenzuela O., Wadsley J., Quinn T., 2007, MNRAS, 374, 1497

Governato F., Zolotov A., Pontzen A., Christensen C., Oh S. H., Brooks A. M., Quinn T., Shen S., Wadsley J., 2012, MNRAS, 422, 1231

Grand R. J. J., Kawata D., Cropper M., 2012, MNRAS, 421, 1529

Gratton R., Carretta E., Matteucci F., Sneden C., 1996, in Morrison H. L., Sarajedini A., eds, ASP Conf. Ser., Vol. 92, Formation of the Galactic Halo...Inside and Out, p. 307

Gratton R. G., Carreta E., Matteucci F., Sneden C., 2000, A&A, 358, p.671

Greggio L., Renzini A., 1983, A&A, 118, 217

Greif T. H., Glover S. C. O., Bromm V., Klessen R. S., 2009, MNRAS, 392, 1381

Guedes J., Callegari S., Madau P., Mayer L., 2011, ApJ, 742, 76

Haardt F., Madau P., 1996, ApJ, 461, 20

Harfst S., Gualandris A., Merritt D., Spurzem R., Portegies S. Z., Berczik P., 2007, New Astronomy, 12, 357

Hashimoto M., Iwamoto K., Nomoto K., 1993, ApJ, 414, L105

Helmi A., de Zeeuw P. T., 2000, MNRAS, 319, 657

Helmi A., Navarro J. F., Nordström B., Holmberg J., Abadi M. G., Steinmetz M., 2006, MNRAS, 365, 1309

Hernquist L., Katz N., 1989, ApJS, 70, 419

Heyer M. H., Corbelli E., Schneider S. E., Young J. S., 2004, ApJ, 603, 723

Holmberg J., Nordström B., Anderson J., 2007, A&A, 475, 519

Holmberg J., Nordström B., Anderson J., 2009, A&A, 501, 941

Hopkins P. F., Quataert E., Murray N., 2011, MNRAS, 421, 3488

Hou J. L., Prantzos N., Boissier S., 2000, A&A, 362, 921

Ibata R., Gilmore G. F., 1995, MNRAS, 275, 605

Immeli A., Samland M., Westera P., Gerhard O., 2004, ApJ, 611, 20

Iwamoto K., Brachwitz F., Nomoto K., Kishimoto N., Umeda H., Hix W. R., Thielemann F., 1999, ApJS, 125, 439

Jarosik N., Bennett C. L., Dunkley J., Gold B., Greason M. R., Halpern M., Hill R. S., Hinshaw G., Kogut A., Komatsu E., Larson D., Limon M., Meyer S. S., Nolta M. R., Odegard N., Page L., Smith K. M., Spergel D. N., Tucker G. S., Weiland J. L., Wollack E., Wright E. L., 2011, ApJS, 192, 14

Jorgensen B. R., Lindegren L., 2005, A&A, 436, 127

Jurić M., Ivezić v., Brooks A., Lupton R. H., Schlegel D., Finkbeiner D., Padmanabhan N., Bond N., Sesar B., Rockosi C. M., Knapp G. R., Gunn J. E., Sumi T., Schneider D. P., Barentine J. C., Brewington H. J., Brinkmann J., Fukugita M., Harvanek M., Kleinman S. J., Krzesinski J., Long D., Neilsen E. H. J., Nitta A., Snedden S. A., York D. G., 2008, ApJ, 673, 864

Källander D., Hultman J., 1998, A&A, 333, 399

Katz N., 1992, ApJ, 391, 502

Katz N., Gunn J. E., 1991, ApJ, 377, 365

Katz N., Weinberg D. H., Hernquist L., 1996, ApJS, 105, 19

Kauffmann G., White S. D. M., Guiderdoni B., 1993, MNRAS, 264, 201

Kawata D., 1999, PASJ, 51, 931

Kawata D., 2001, ApJ, 558, 598

Kawata D., Gibson B. K., 2003a, MNRAS, 340, 908

Kawata D., Gibson B. K., 2003b, MNRAS, 346, 135

Kawata D., Gibson B. K., Windhorst R. A., 2004, MNRAS, 354, 387

Kawata D., Okamoto T., Gibson B. K., Barnes D. J., Cen R., 2009, ArXiv e-prints: 0902.4002v2

Kay S. T., Pearce F. R., Jenkins A., Frenk C. S., White S. D. M., Thomas P. A., Couchman H. M. P., 2000, MNRAS, 316, 374

Kennicutt R. C., 1989, ApJ, 344, 685

Kennicutt R. C., 1998a, ARA&A, 36, 189

Kennicutt R. C., 1998b, ApJ, 498, 541

Klypin A., Kravtsov A. V., Bullock J. S., Primack J. R., 2001, ApJ, 554, 903

Klypin A., Kravtsov A. V., Valenzuela O., Prada F., 1999, ApJ, 522, 82

Knebe A., Gill S. P. D., Kawata D., Gibson B. K., 2005, MNRAS, 357, L35

Kobayashi C., Tsujimoto T., Nomoto K., 2000, ApJ, 539, 26

Kodama T., 1997, PhD thesis, Univ. Tokyo

Kodama T., Arimoto N., 1997, A&A, 320, 41

Komatsu E., Smith K. M., Dunkley J., Bennett C. L., Gold B., Hinshaw G., Jarosik N., Larson D., Nolta M. R., Page L., Spergel D. N., Halpern M., Hill R. S., Kogut A., Limon M., Meyer S. S., Odegard N., Tucker G. S., Weiland J. L., Wollack E., Wright E. L., 2011, ApJS, 192, 18

Kravtsov A. V., 2003, ApJ, 590, L1

Kroupa P., 2002, MNRAS, 330, 707

Krumholz M. R., McKee C. F., Tumlinson J., 2009, ApJ, 699, 850

Larson R. B., 1969, MNRAS, 145, 405

Larson R. B., 1974, MNRAS, 166, 585

Larson R. B., 1975, MNRAS, 173, 671

Larson R. B., 1976, MNRAS, 176, 31

Lemasle B., Francois P., Piersimoni A., Pedicelli S., Bono G., Laney C. D., Primas F., Romaniello M., 2008, A&A, 490, 613

Leroy A., Walter F., Brinks E., Bigiel F., de Blok W. J. G., Madore B., Thornley M. D., 2008, AJ, 136, 2782

Lia C., Portinari L., Carraro G., 2002, MNRAS, 330, 821

Lineweaver C. H., Fenner Y., Gibson B. K., 2004, Science, 303, 59

Lovell M. R., Eke V., Frenk C. S., Gao L., Jenkins A., Theuns T., Wang J., White S. D. M., Boyarsky A., Ruchayskiy O., 2012, MNRAS, 420, 2318

Luck R. E., Gieren W. P., Andrievsky S. M., Kovtyukh V. V., Fouqué P., Pont F., Kienzle F., 2003, A&A, 401, 939

Lucy L. B., 1977, AJ, 82, 1013

MacArthur L. A., González J. J., Courteau S., 2009, MNRAS, 395, 28

Maciel W. J., Costa R. D. D., 2009, ApJ, 254, 38

Magrini L., Corbelli E., Galli D., 2007a, A&A, 470, 843

Magrini L., Sestito P., Randich S., Galli D., 2009a, A&A, 494, 95

Magrini L., Stanghellini L., Villaver E., 2009b, ApJ, 696, 729

Magrini L., Vílchez J. M., Mampaso A., Corradi R. L. M., Leisy P., 2007b, A&A, 470, 865

Makino J., 1991, PASJ, 43, 859

Martínez-Serrano F. J., Serna A., Domínguez-Tenreiro R., Mollá M., 2008, MNRAS, 388, 39

Martínez-Serrano F. J., Serna A., Domínguez-Tenreiro R., Mollá M., 2008, MNRAS, 388, 39

Matteucci F., Brocato E., 1990, ApJ, 365, L539

Mayer L., Governato F., Kaufmann T., 2008, ASL, 1, 7

McConnachie A. W., Irwin M. J., Ibata R. A., Dubinski J., Widrow L. M., Martin N. F., Côté P., Dotter A. L., Navarro J. F., Ferguson A. M. N., Puzia T. H., Lewis G. F., Babul A., Barmby P., Bienaymé O., Chapman S. C., Cockcroft R., Collins M. L. M., Fardal M. A., Harris W. E., Huxor A., Mackey A. D., Peñarrubia J., Rich R. M., Richer H. B., Siebert A., Tanvir N., Valls-Gabaud D., Venn K. A., 2009, Nature, 461, 66

McMillan P. J., 2011, MNRAS, 414, 2446

McWilliam A., Rich M. R., 1994, ApJ, 91, L749

Melott A. L., Lieberman B. S., Laird C. M., Martin L. D., Medvedev M. V., Thomas B. C., Cannizzo J. K., Gehrels N., Jackman C. H., 2004, International Journal of Astrobiology, 3, 55

Merlin E., Buonomo U., Grassi T., Piovan L., Chiosi C., 2010, A&A, 513, 36

Merritt D., Ferrarese L., Joseph C. L., 2001, Science, 293, 1116

Moore B., Ghigna S., Governato F., Lake G., Quinn T., Stadel J., Tozzi P., 1999a, ApJ, 524, L19

Moore B., Quinn T., Governato F., Stadel J., Lake G., 1999b, MNRAS, 310, 1147

Mori M., Yoshii Y., Tsujimoto T., Nomoto K., 1997, ApJ, 478, L21

Morris J., 1997, Journal of Computational Physics, 136, 41

Mulchaey J. S., Davis D. S., Mushotzky R. F., Burstein D., 1993, ApJ, 404, L9

Nakasato N., Nomoto K., 2003, ApJ, 588, 842

Navarro J. F., Frenk C. S., White S. D. M., 1995, MNRAS, 275, 56

Navarro J. F., Frenk C. S., White S. D. M., 1997, ApJ, 490, 493

Navarro J. F., Steinmetz M., 1997, ApJ, 478, 13

Navarro J. F., White S. D. M., 1993, MNRAS, 265, 271

Noguchi M., 1998, Nature, 392, 253

Nordström B., Mayor M., Anderson J., Holmberg J., Pont F., Jorgensen B. R., Olsen E. H., Udry S., Mowlavi N., 2004, A&A, 418, 989

Norman C. A., Sellwood J. A., Hasan H., 1996, ApJ, 462, 114

Oey M. S., Massey P., 1994, ApJ, 425, 635

Okamoto T., Frenk C. S., Jenkins A., Theuns T., 2010, MNRAS, 406, 208

Okamoto T., Nemmen R. S., Bower R. G., 2008, MNRAS, 385, 161

Ostriker J. P., Peebles P. J. E., 1973, ApJ, 186, 467

Pancino E., Carrera R., Rossetti E., Gallart C., 2010, A&A, 511, 56

Pedicelli S., Bono G., Lemasle B., Francois P., Groenewegen M., Lub J., Pel J. W., Laney D., Piersimoni A., Romaniello M., Buonanno R., Caputo F., Cassisi S., Castelli F., Leurini S., Pietrinferni A., Primas F., Pritchard J., 2009, A&A, 504, 81

Peebles P. J. E., 1971, A&A, 11, 377

Pelupessy F. I., van der Werf P. P., Icke V., 2004, A&A, 422, 55

Perlmutter S., Aldering G., della Valle M., Deustua S., Ellis R. S., Fabbro S., Fruchter A., Goldhaber G., Groom D. E., Hook I. M., Kim A. G., Kim M. Y., Knop R. A., Lidman C., McMahon R. G., Nugent P., Pain R., Panagia N., Pennypacker C. R., Ruiz-Lapuente P., Schaefer B., Walton N., 1998, Nature, 391, 51

Pilkington K., Gibson B. K., Calura F., Brooks A. M., Mayer L., Brook C. B., Stinson G. S., Thacker R. J., Few C. G., Cunnama D., Wadsley J., 2011, MNRAS, 417, 2891

Pont F., Eyer L., 2004, MNRAS, 351, 487

Price D. J., 2008, Journal of Computational Physics, 227, 10040

Price D. J., Monaghan J. J., 2007, MNRAS, 374, 1347

Prochaska J. X., Naumov S. O., Carney B. W., McWilliam A., Wolfe A. M., 2000, AJ, 120, 2513

Purcell C. W., Bullock J. S., Tollerud E. J., Rocha M., Chakrabarti S., 2011, Nature, 477, 301

Putman M. E., Peek J. E. G., Muratov A., Gnedin O. Y., Hsu W., Douglas K. A., Heiles C., Stanimirovic S., Korpela E. J., Gibson S. J., 2009, ApJ, 703, 1486

Rahimi A., Kawata D., 2012, MNRAS, 422, 2609

Rahimi A., Kawata D., Brook C. B., Gibson B. K., 2010, MNRAS, 401, 1826

Raiteri C. M., Villata M., Navarro J. F., 1996, A&A, 315, 105

Recchi S., Matteucci F., D'Ercole A., 2001, MNRAS, 322, 800

Reddy B. E., Tomkin J., Lambert D. L., Allende Prieto C., 2003, MNRAS, 340, 304

Reid M. J., Menten K. M., Brunthaler A., Moellenbrock G. A., 2009, Astro2010: The Astronomy and Astrophysics Decadal Survey

Renda A., Gibson B. K., Mouhcine M., Ibata R. A., Kawata D., Flynn C., Brook C. B., 2005a, MNRAS, 363, L16

Renda A., Kawata D., Fenner Y., Gibson B. K., 2005b, MNRAS, 356, 1071

Robertson B. E., Kravtsov A. V., 2008, ApJ, 680, 1083

Robin A. C., Reyle C., Picaud S., Schultheis M., 2005, A&A, 430, 129

Rocha-Pinto H. J., Flynn C., Scalo J., Hänninen J., Maciel W. J., Hensler G., 2004, A&A, 423, 517

Rocha-Pinto H. J., Scalo J., Maciel W. J., Flynn C., 2000, A&A, 358, 869

Roŝkar R., Debattista V. P., Quinn T. R., Stinson G. S., Wadsley J., 2008, ApJ, 684, 79

Rosolowsky E., Simon J. D., 2008, ApJ, 675, 1213

Rosswog S., Price D., 2007, MNRAS, 379, 915

Rubin R. H., Simpson J. P., Colgan S. W. J., Dufour R. J., Brunner G., McNabb I. A., Pauldrach A. W. A., Erickson E. F., Haas M. R., Citron R. I., 2008, MNRAS, 387, 45

Russeil D., 2003, A&A, 397, 133

Ryder S. D., Fenner Y., Gibson B. K., 2005, MNRAS, 358, 1337

Saitoh T. R., Daisaka H., Kokubo E., Makino J., Okamoto T., Tomisaka K., Wada K., Yoshida N., 2008, PASJ, 60, 667

Saitoh T. R., Makino J., 2009, ApJ, 697, L99

Saitoh T. R., Makino J., 2010, PASJ, 62, 301

Salpeter E. E., 1955, ApJ, 121, 161

Sanchez-Blazquez P., Courty S., Gibson B. K., Brook C. B., 2009, MNRAS, 398, 591

Scannapieco C., Tissera P. B., White S. D. M., Springel V., 2005, MNRAS, 364, 552

Scannapieco C., Tissera P. B., White S. D. M., Springel V., 2008, MNRAS, 389, 1137

Scannapieco C., Wadepuhl M., Parry O. H., Navarro J. F., Jenkins A., Springel V., Teyssier R., Carlson E., Couchman H. M. P., Crain R. A., Dalla Vecchia C., Frenk C. S., Kobayashi C., Monaco P., Murante G., Okamoto T., Quinn T., Schaye J., Stinson G. S., Theuns T., Wadsley J., White S. D. M., Woods R., 2012, MNRAS, 396, 2970

Scannapieco C., White S. D. M., Sringel V., Tissera P. B., 2009, MNRAS, 396, 696

Schmidt B. P., Suntzeff N. B., Phillips M. M., Schommer R. A., Clocchiatti A., Kirshner R. P., Garnavich P., Challis P., Leibundgut B., Spyromilio J., Riess A. G., Filippenko A. V., Hamuy M., Smith R. C., Hogan C., Stubbs C., Diercks A., Reiss D., Gilliland R., Tonry J., Maza J., Dressler A., Walsh J., Ciardullo R., 1998, ApJ, 507, 46

Schmidt M., 1959, ApJ, 129, 243

Schönrich R., Asplund M., Casagrande L., 2011, MNRAS, 415, 3807

Schönrich R., Binney J., 2009a, MNRAS, 396, 203

Schönrich R., Binney J., 2009b, MNRAS, 396, 203

Schönrich R., Binney J., 2009c, MNRAS, 399, 1145

Schröder K. P., Pagel B. E. J., 2003, MNRAS, 343, 1231

Sellwood J. A., Binney J. J., 2002, MNRAS, 336, 785

Sestito P., Bragaglia A., Randich S., Andrievsky S. M., Korotin S. A., 2008, A&A, 488, 943

Shaye J., Dalla Vecchia C., 2008, MNRAS, 383, 1210

Shen J., Rich R. M., Kormendy J., Howard C. D., De Propris R., Kunder A., 2010, ApJ, 720, L72

Shull J. M., 1980, ApJ, 238, 860

Sofue Y., Nagayama T., Matsui M., Nakagawa A., 2011, PASJ, 63, 867

Somerville R. S., Hopkins P. F., Cox T. J., Robertson B. E., Hernquist L., 2008, MNRAS, 481

Somerville R. S., Primack J. R., 1999, MNRAS, 310, 1087

Somerville R. S., Primack J. R., Faber S. M., 2001, MNRAS, 320, 504

Spergel D. N., Verde L., Peiris H. V., Komatsu E., Nolta M. R., Bennett C. L., Halpern M., Hinshaw G., Jarosik N., Kogut A., Limon M., Meyer S. S., Page L., Tucker G. S., Weiland J. L., Wollack E., Wright E. L., 2003, ApJS, 148, 175

Springel V., 2005, MNRAS, 364, 1105

Springel V., Di Matteo T., Hernquist L., 2005a, MNRAS, 361, 776

Springel V., Hernquist L., 2002, MNRAS, 333, 649

Springel V., Hernquist L., 2003, MNRAS, 339, 289

Springel V., Wang J., Vogelsberger M., Ludlow A., Jenkins A., Helmi A., Navarro J. F., Frenk C. S., White S. D. M., 2008, MNRAS, 391, 1685

Springel V., White S. D. M., Jenkins A., Frenk C. S., Yoshida N., Gao L., Navarro J., Thacker R., Croton D., Helly J., Peacock J. A., Cole S., Thomas P., Couchman H., Evrard A., Colberg J., Pearce F., 2005b, Nature, 435, 629

Stanek K. Z., 1995, ApJ, 441, L29

Steinmetz M., Muller E., 1994, A&A, 281, 97

Steinmetz M., Muller E., 1995, MNRAS, 276, 549

Stinson G., Seth A., Katz N., Wadsley J., Governato F., Quinn T., 2006, MNRAS, 373, 1074

Sutherland R. S., Dopita M. A., 1993, ApJS, 88, 253

Tamburro D., Rix H. W., Leroy A. K., Mac Low M. M., Walter F., Kennicutt R. C., Brinks E., de Blok W. J. G., 2009, AJ, 137, 4424

Tasker E. J., Bryan G. L., 2006, ApJ, 641, 878

Tasker E. J., Bryan G. L., 2008, ApJ, 673, 810

Tautvaišienė G., Edvardsson B., Tuominen I., Ilyin I., 2001, A&A, 380, 578

Thacker R. J., Couchman H. M. P., 2000, ApJ, 545, 728

Timmes F. X., Woosley S. E., Weaver T. A., 1995, ApJS, 98, 617

Toomre A., Toomre J., 1972, ApJ, 178, 623

Twarog B. A., Ashman K. M., Anthony-Twarog B. J., 1997, AJ, 114, 2556

Tyson J. A., Wenk R. A., Valdes F., 1990, ApJ, 349, L1

van den Hoek L. B., Groenewegen M. A. T., 1997, A&AS, 123, 305

Vande Putte D., Cropper M., Ferreras I., 2009, MNRAS, 397, 1587

Verley S., Corbelli E., Giovanardi C., Hunt L. K., 2010, A&A, 510, 64

Viironen K., Delgado-Inglada G., Mampaso A., Magrini L., Corradi R. L. M., 2007, MNRAS, 381, 1719

Wada K., Norman C. A., 2007, ApJ, 660, 276

Walter F., Brinks E., de Blok W. J. G., Bigiel F., Kennicutt R. C., Thornley M. D., Leroy A., 2008, AJ, 136, 2563

Weaver R., McCray R., Castor J., Shapiro P., Moore R., 1977, ApJ, 218, 377

White S. D. M., Frenk C. S., 1991, ApJ, 379, 52

White S. D. M., Rees M. J., 1978, MNRAS, 183, 341

Williams B. F., Dalcanton J. J., Dolphin A. E., Holtzman J., Sarajedini A., 2009, ApJ, 695, 15

Woosley S. E., Weaver T. A., 1995, ApJS, 101, 181

Wyse R. F. G., 1999, Baltic Astronomy, 8, 593

Yoachim P., Dalcanton J. J., 2005, ApJ, 624, 701

Yoachim P., Dalcanton J. J., 2006, AJ, 131, 226

Yoachim P., Dalcanton J. J., 2008, ApJ, 683, 707

Yong D., Carney B., Teixera de Almeida M. L., 2005, AJ, 130, 597

Zoccali M., Hill V., Lecureur A., Barbuy B., Renzini A., Minniti D., Gómez A., Ortolani S., 2008, A&A, 486, 177

Zoccali M., Lecureur A., Barbuy B., Hill V., Renzini A., Minniti D., Momany Y., Gómez A., Ortolani S., 2006, A&A, 457, L1

Zolotov A., Willman B., Brooks A. M., Governato F., Brook C. B., Hogg D. W., Quinn T., Stinson G., 2009, ApJ, 702, 1058

Publications

Refereed Journals

---

1. **A. Rahimi**, D. Kawata, C. B. Brook, B. K. Gibson:
   Chemodynamical analysis of bulge stars for simulated disc galaxies
   Mon.Not.R.Astron.Soc. **401**, 1826 (2010)

2. **A. Rahimi**, D. Kawata, C. Allende Prieto, C. B. Brook, B. K. Gibson, A. Kiessling:
   Metallicity gradients of disc stars for a cosmologically simulated galaxy
   Mon.Not.R.Astron.Soc. **415**, 1469 (2011)

3. K. Pilkington, C. G. Few, B. K. Gibson, F. Calura, L. Michel-Dandax, R. J. Thacker, M. Molla, F. Matteucci, **A. Rahimi**, D. Kawata, C. Kobayashi, C. B. Brook, G. S. Stinson, H. M. P. Couchman, J. Bailin, J. Wadsley:
   Metallicity Gradients in Disks: Do Galaxies Form Inside-Out?
   Astron. & Astrophys **540**, A56 (2012)

4. **A. Rahimi**, D. Kawata, 2012,
   Towards a self-consistent numerical model of late-type galaxies: Calibrating the effects of sub-grid physics on galactic models
   Mon.Not.R.Astron.Soc. **422**, 2609 (2012)